MASTER

Stress-Strain Characteristics of Materials at High Strain Rates

Part IV

EXPERIMENTAL AND THEORETICAL ANALYSIS OF PLASTIC IMPACTS ON SHORT CYLINDERS

by

Charles H. Karnes

Prepared for

THE SANDIA CORPORATION
CONTRACT AT(29-2)-621

THE UNIVERSITY OF TEXAS
STRUCTURAL MECHANICS RESEARCH LABORATORY
AUSTIN, TEXAS
JUNE 21, 1960

DISCLAIMER

STRESS-STRAIN CHARACTERISTICS OF MATERIALS AT HIGH STRAIN RATES

Part IV

Experimental and Theoretical Analysis of Plastic Impacts on Short Cylinders

by

Charles H. Karnes

Prepared for

THE SANDIA CORPORATION
Contract AT(29-2)-621

THE UNIVERSITY OF TEXAS
STRUCTURAL MECHANICS RESEARCH LABORATORY
Austin, Texas

June 21, 1960

The Structural Mechanics Research Laboratory

is cooperatively operated by

The Engineering Mechanics and Civil Engineering Departments

at

The Balcones Research Center

University of Texas

Austin, Texas

PREFACE

The research reported here is a continuation of a program which was initiated November 1, 1957 under the sponsorship of Department 5130 of the Sandia Corporation, Contract No. AT(29-2)-621. In the work previously reported under this contract, the stress-strain characteristics of materials were determined by measuring both stress and strain as a function of time and then combining these measurements to obtain stress as a function of strain. To do this, however, certain basic assumptions were required. As the work progressed and the results were studied, it became evident that the assumptions and the experimental techniques should be critically reviewed. A review of the assumptions that had been made regarding the distribution of strain along the length of the specimen during impact, and the variation in strain rate with time during the impact, motivated the investigation described here.

It will be noted that whereas originally information concerning the stress-strain characteristics of materials at high strain rates had been sought as an aid in analyzing plastic wave propagation, in this work, present theories of plastic wave propagation are used in conjunction with experimental results to obtain stress-strain characteristics. This indirect approach promises to be more fruitful than the direct approach followed in previous work.

Experimental and Theoretical Analysis of Plastic Impacts on Short Cylinders, the title of this report, is also the title of a thesis prepared by Charles H. Karnes in partial fulfullment of the requirements for a Master of Science degree. The results presented here are essentially a reproduction of that thesis, with some additional material.

On behalf of the author and myself, I would like to acknowledge the contributions of others, and to express our gratitude to the personnel of Department 5130 for making this research possible.

J. Neils Thompson
Director
Structural Mechanics Research Laboratory
The University of Texas
Austin, Texas

June 21, 1960

TABLE OF CONTENTS

TABLE OF CONTENTS
(Cont'd)

LIST OF FIGURES

Figure Page

LIST OF FIGURES
(Cont'd)

LIST OF FIGURES
(Cont'd)

LIST OF FIGURES
(Cont'd)

LIST OF FIGURES
(Cont'd)

LIST OF TABLES

ABSTRACT

The effects of strain rate on the stress-strain characteristics of copper and lead were studied by measuring both stress and strain as functions of time using short cylindrical specimens supported at one end on a modified Hopkinson pressure bar and impacted at the other end by a steel projectile. Corresponding stresses and strains were computed according to an elementary nonstrain-rate theory (sometimes referred to as the von Karman theory) in which the dynamic stress-strain curve is assumed to be the same as the static stress-strain curve. Stresses and strains were also computed according to an elementary strain-rate theory (sometimes referred to as the Malvern theory) in which the dynamic stress may exceed the static stress for a given strain by an amount which depends upon the strain rate.

It was found that the predictions of the nonstrain-rate theory agreed with measured values only for low impact velocities and for points at least two diameters from the impact end of the specimen. By proper choice of the flow or relaxation constant in the elementary strain-rate theory, measured and computed values of strain, or of stress, but not both simultaneously, could be brought into agreement. In the more general exponential-type, strain-rate law, two independent parameters appear. Presumably with two constants to adjust, this theory could be made to correctly predict both stresses and strains for the conditions under which the tests were performed. If this

procedure forces the theory to account for variations which are actually caused by lateral inertia and shear, erroneous conclusions regarding the properties of the material will be drawn. Further study of the effects of shear and lateral inertia is indicated.

INTRODUCTION

In studies of the effect of strain rate on the stress-strain characteristics of materials, it is essential that the measurements be made at a constant strain rate. To obtain a constant and controllable strain rate in the work which has been done during the past two years in the Structural Mechanics Research Laboratory, short cylindrical specimens 2 in. or less in length were supported with one end against a steel pressure bar, and impacted at the other end by a steel projectile with a large mass relative to the mass of the specimen, moving at velocities ranging from 30 to 500 fps. Under these conditions, the projectile will continue to move at virtually a constant velocity for an appreciable time after impact.

It was expected that during the early part of the impact, the strain at a given point in the specimen would increase in a stepwise fashion as the strain waves generated by the impact reflected back and forth between the projectile and the semifixed end at the pressure bar, but that a smooth curve drawn through the steps in the actual strain record would give a close approximation of the strain variation with time and would provide a measure of strain rate.

It had been assumed in the previous work that in these short specimens, strain would be uniformly distributed along the length. This assumption led to the conclusion that the strain rate should be proportional to the ratio of impact velocity to specimen length, and, likewise, strain at any point in the specimen should be the displacement of the projectile after initial contact with the specimen, divided by the length of the specimen. These assumptions and deductions were used as a basis for the determination of dynamic stress-strain characteristics at high strain rates.[1, 2]

When preliminary strain measurements on the specimens not only failed to reveal any steps in the strain-time records, but also indicated a considerable variation in strain along the length of the specimen, it was obvious that at least some aspects of the previous approach to the measurement of dynamic stress-strain characteristics would have to be abandoned and a new approach developed.

One of the principal reasons for obtaining dynamic stress-strain characteristics in the first place was the need for such information in plastic wave propagation studies. Since any attempt to make direct measurements of stress or strain developed by impact always involves the propagation of waves and is complicated by the presence of the waves, it seems that here is an enemy that can not be defeated, and hence, should be joined. The waves should be used somehow to infer the dynamic stress-strain characteristics of the material.

Further reflection on this problem led to the conclusion that the best approach possible to a solution would be to measure strains with gages mounted directly on the specimen and to measure the stress at one end of the specimen by using the Hopkinson pressure bar, and then compare these measured values with predicted values, the predictions being based on each of the two theories of longitudinal plastic wave propogation that have been proposed. From these comparisons, it is hoped that it may be possible to infer the exact nature of the dynamic properties of the material.

As a consequence of this reasoning, an extensive study was initiated of the strain variations with time at the impact end and the variation of both stress and strain at the other end of short specimens. Previous investigators studying plastic wave propagation have all used bars long enough to be regarded as infinitely long, but this made it impossible to measure the stress at any point in the bar. In the present study, short specimens have been used to make it possible to measure stresses with the pressure-bar technique at a point where the strains are still in the plastic range. The short specimen and the pressure bar complicate the theoretical calculation of the stresses and strains but not to a prohibitive extent.

There are, as previously mentioned, two theories of plastic wave propagation in bars now competing somewhat in the theoretical market place. The first of these, referred to as the nonstrain-rate theory, (sometimes called the von Karman theory) is based upon an idea first suggested by Donnell[3] and later developed by von Karman,[4] and Taylor[5] independently. In this theory, the material is assumed to follow the same stress-strain relationship under dynamic loading as it follows under static loading. From this, it follows that for plane waves in bars, the velocity of propagation must be proportional to the square root of the tangent modulus. The second theory, referred to as the strain-rate theory and sometimes called the Malvern[6] theory, is based upon the assumption that the stress at a given dynamic strain is increased over what it would be for a static strain of the same magnitude by an amount that is proportional to the strain rate.

In the following sections essential details of the two theories are presented and the methods used for computing stress and strain are described. The technique and equipment used for measuring stress and strain are described. Measured values are compared with computed values and some conclusions are drawn regarding the significance of the results.

THEORETICAL DETERMINATION OF STRAIN DISTRIBUTION

The problem to be considered is that of a rigid projectile impacting a short cylinder which is mounted on a steel pressure bar as shown in Fig. 1.

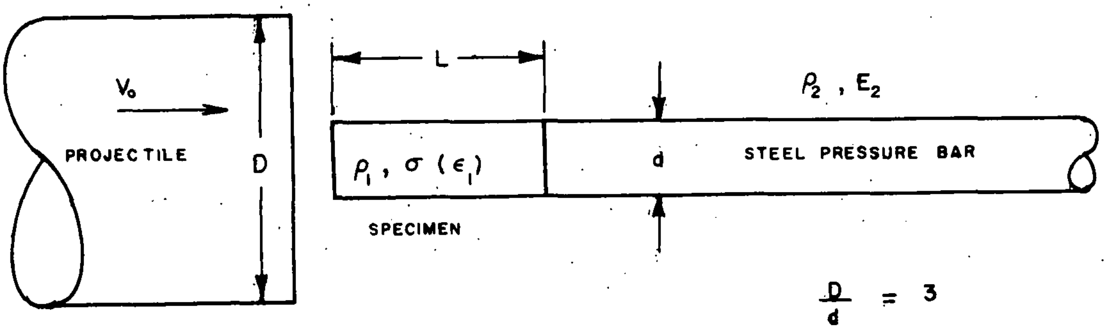

FIG. 1, SCHEMATIC OF PROBLEM

The projectile is considered rigid in the problem because it is made of steel which is stiffer than the specimen and its cross-sectional area is large compared to that of the specimen and pressure bar.

Nonstrain-Rate Theory

In the nonstrain-rate theory, the assumption is made that the static stress-strain curve is unique for the material in question and does not depend on strain rate. With this assumption as a basis, the relationships between propagational velocity and particle velocity with strain are developed as follows.

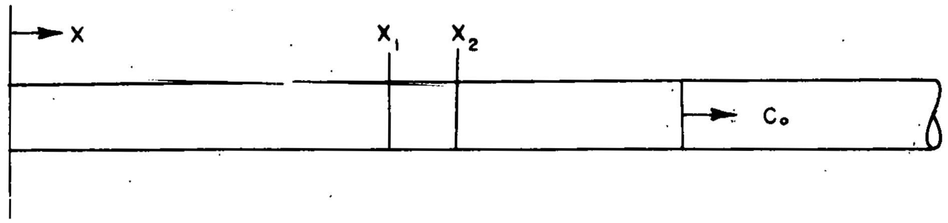

FIG. 2, STRESS WAVE TRAVELING IN SPECIMEN

Consider a specimen as shown in Fig. 2, in which a stress wave is traveling in the x-direction. If the front of the wave has passed the element bounded by the planes of x_1 and x_2, then a free body diagram of the element may be drawn as shown in Fig. 3.

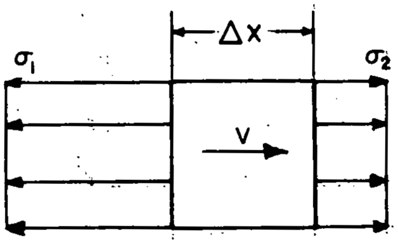

FIG. 3, FREE BODY DIAGRAM OF ELEMENT

The equation of motion for the element is

$$\Sigma F_x = (\sigma_2 - \sigma_1)A = \rho A \Delta x \frac{\partial^2 u}{\partial t^2} \qquad \text{- - - - -} \quad (1a)$$

and in the limit

$$\frac{\partial \sigma}{\partial x} = \rho \frac{\partial^2 u}{\partial t^2} \qquad \text{- - - - -} \quad (1b)$$

where the displacement of the element from its original position in the bar is u. The strain is

$$\varepsilon = \frac{\partial u}{\partial x} \qquad \text{- - - - -} \quad (2)$$

In accordance with the basic assumption, the stress is a function of strain only, that is

$$\sigma = \sigma(\varepsilon)$$

Therefore $$\frac{\partial \sigma}{\partial x} = \frac{d\sigma}{d\varepsilon} \frac{\partial \varepsilon}{\partial x} = \frac{d\sigma}{d\varepsilon} \frac{\partial^2 u}{\partial x^2} \qquad \text{- - - - -} \quad (3)$$

Substituting Eq. (3) into Eq. (1b) yields

$$\frac{\partial^2 u}{\partial t^2} = C^2 \frac{\partial^2 u}{\partial x^2} \qquad \text{- - - - -} \quad (4)$$

where
$$C = \left[\frac{1}{\rho}\,\frac{d\sigma}{d\varepsilon}\right]^{1/2} \qquad \text{- - - - -} \qquad (5)$$

is the propagational velocity of a stress wave whose amplitude is σ and $\frac{d\sigma}{d\varepsilon}$ is the slope of $\sigma(\varepsilon)$ at the stress σ.

The particle velocity, V, may be computed by applying the principle of impulse and momentum to the element. The impulse is produced by the differential force, $Ad\sigma$, acting on the element for a time corresponding to the time required for the stress wave to travel the length dx. The velocity of the element changes by an increment dV in that time and the change in momentum is

$$\rho A dx dV = -A d\sigma \frac{dx}{C} \qquad \text{- - - - -} \qquad (6)$$

or
$$dV = -\frac{1}{\rho}\,\frac{d\sigma}{C} \qquad \text{- - - - -} \qquad (7)$$

where C is determined by the stress, σ. The total change in particle velocity during the passage of any part of a stress wave is

$$V_2 - V_1 = -\frac{1}{\rho}\int_{\sigma_1}^{\sigma_2} \frac{d\sigma}{C} \qquad \text{- - - - -} \qquad (8)$$

If a specimen is impacted with a velocity, V_o, which must be the particle velocity at the impact end, since the projectile is regarded as rigid, then the maximum stress generated at the impact end is determined by Eq. (8) where V_1 and σ_1 are zero. If σ_2 is greater than the yield stress, the shape of the stress wave will change as it travels down the bar. This is illustrated in Fig. 4.

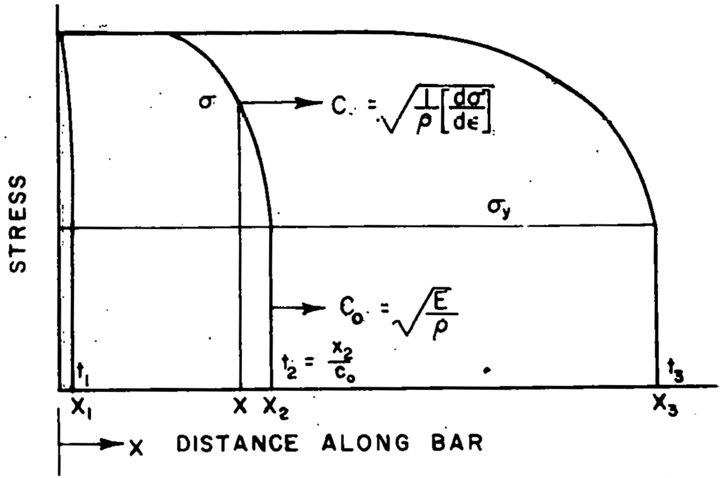

FIG. 4 , DISTORTION OF PLASTIC WAVE

At time t_1, immediately after impact, the wave has traveled a short distance x_1. At time, t_2, the elastic front of the wave has traveled a distance $x_2 = C_o t_2$, but the stress σ has traveled a distance of $x = Ct_2$. Thus, the wave is becoming more and more distorted as it travels down the specimen.

If the stress wave generated on impact is considered to be made up of a series of finite steps, each traveling at a velocity determined by the stress level, the passage of the wave along the specimen and the reflections at the interface between the specimen and pressure bar can be analyzed by considering each step separately as it is reflected off the pressure bar and is superposed on the subsequent steps following behind it. Fig. 5 illustrates how a wave consisting of finite steps is distorted as it travels down a specimen.

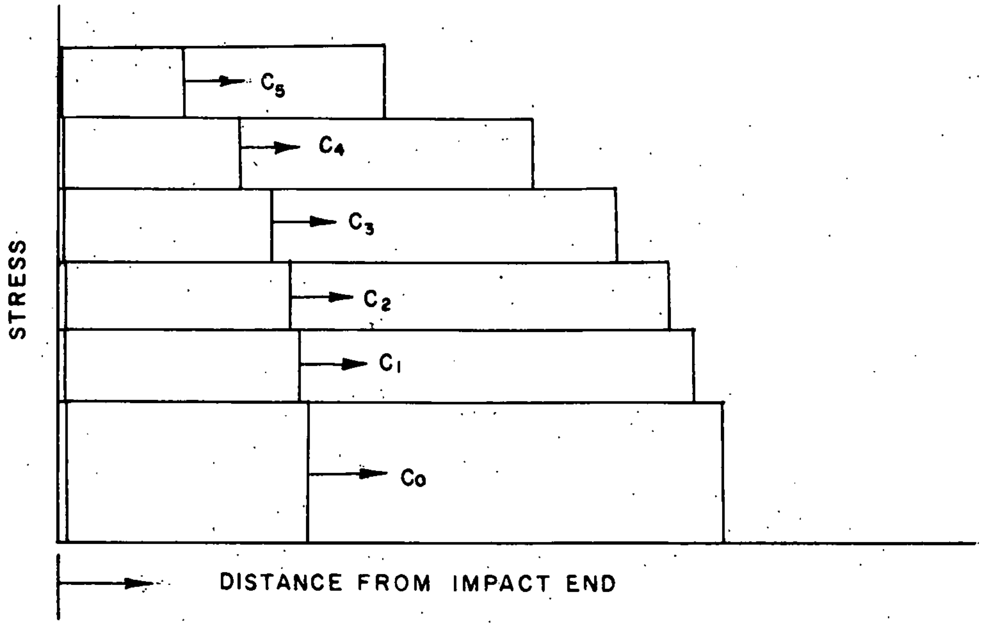

FIG. 5, DISTORTION OF WAVE APPROXIMATED BY SERIES OF FINITE STEPS

Reflections at a fixed end.[7] Consider a point, p, near a fixed end of a specimen in which a stress wave of magnitude σ_i is propagating. The passing stress wave will impart to p a velocity V_i determined by Eq. (8) or

$$V_i = -\frac{1}{\rho}\int_0^{\sigma_i}\frac{d\sigma}{C} \qquad ----- \quad (9)$$

This particle velocity remains constant until after the wave reflected from the fixed end passes point p traveling in the opposite direction. Since the velocity at the fixed end must be zero, the reflected wave must provide a particle velocity which exactly cancels V_i.

Therefore, for a fixed end

$$\frac{1}{\rho}\int_0^{\sigma_i}\frac{d\sigma}{C} = \frac{1}{\rho}\int_{\sigma_i}^{\sigma_t}\frac{d\sigma}{C} = \frac{1}{\rho}\int_0^{\sigma_t}\frac{d\sigma}{C} - \frac{1}{\rho}\int_0^{\sigma_i}\frac{d\sigma}{C} \quad ---- \quad (10)$$

$$\text{or} \quad 2V_i = V_t \quad ----- \quad (11)$$

$$\text{where} \quad V_t = \frac{1}{\rho}\int_0^{\sigma_t}\frac{d\sigma}{C} \quad ----- \quad (12)$$

V_t is not to be interpreted as the resultant particle velocity after passage of the reflected wave, but only as the integral given in Eq. (12). The stress σ_t is the total stress at the end of the bar after the reflection takes place.

The value of V as a function of stress may be computed by obtaining the propagational velocity as a function of stress and performing the necessary numerical integration. C and V for commercially pure copper and Tellurium lead are shown as functions of strain in Figs. 6 and 7. These curves were computed from the static stress-strain curves shown in Figs. 8 and 9.

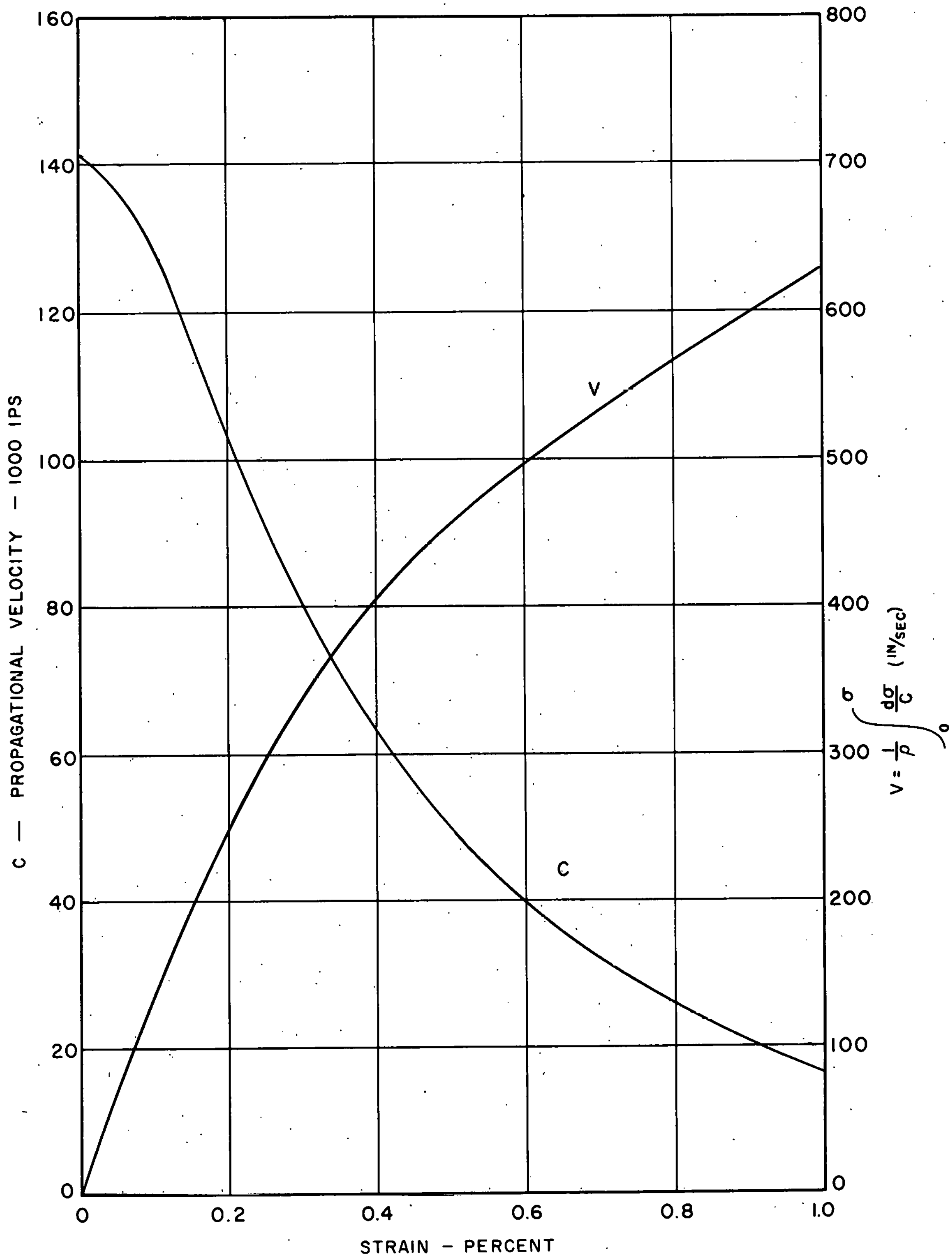

FIG. 6, C & V CURVES FOR COPPER

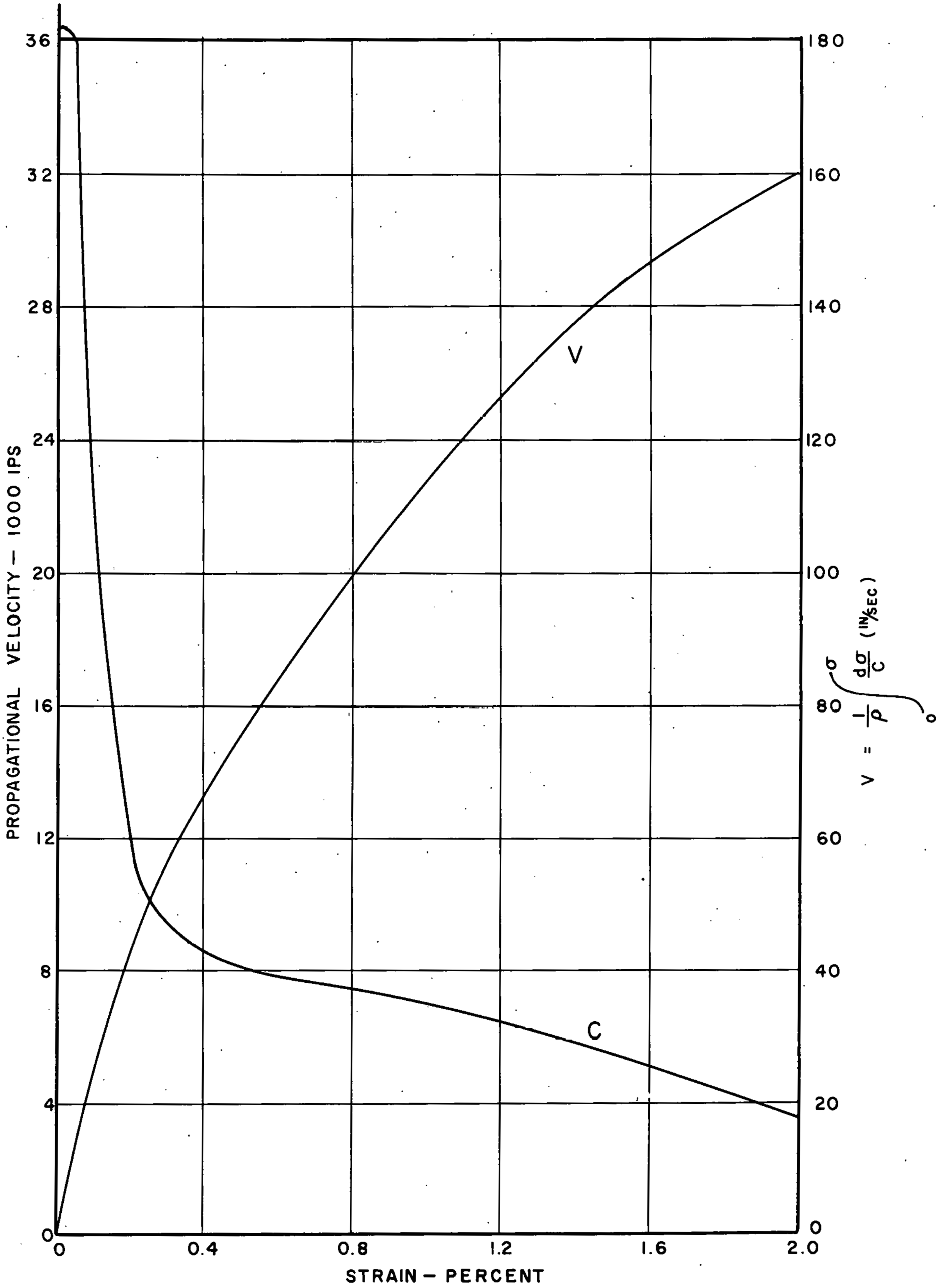

FIG. 7 C & V CURVES FOR LEAD

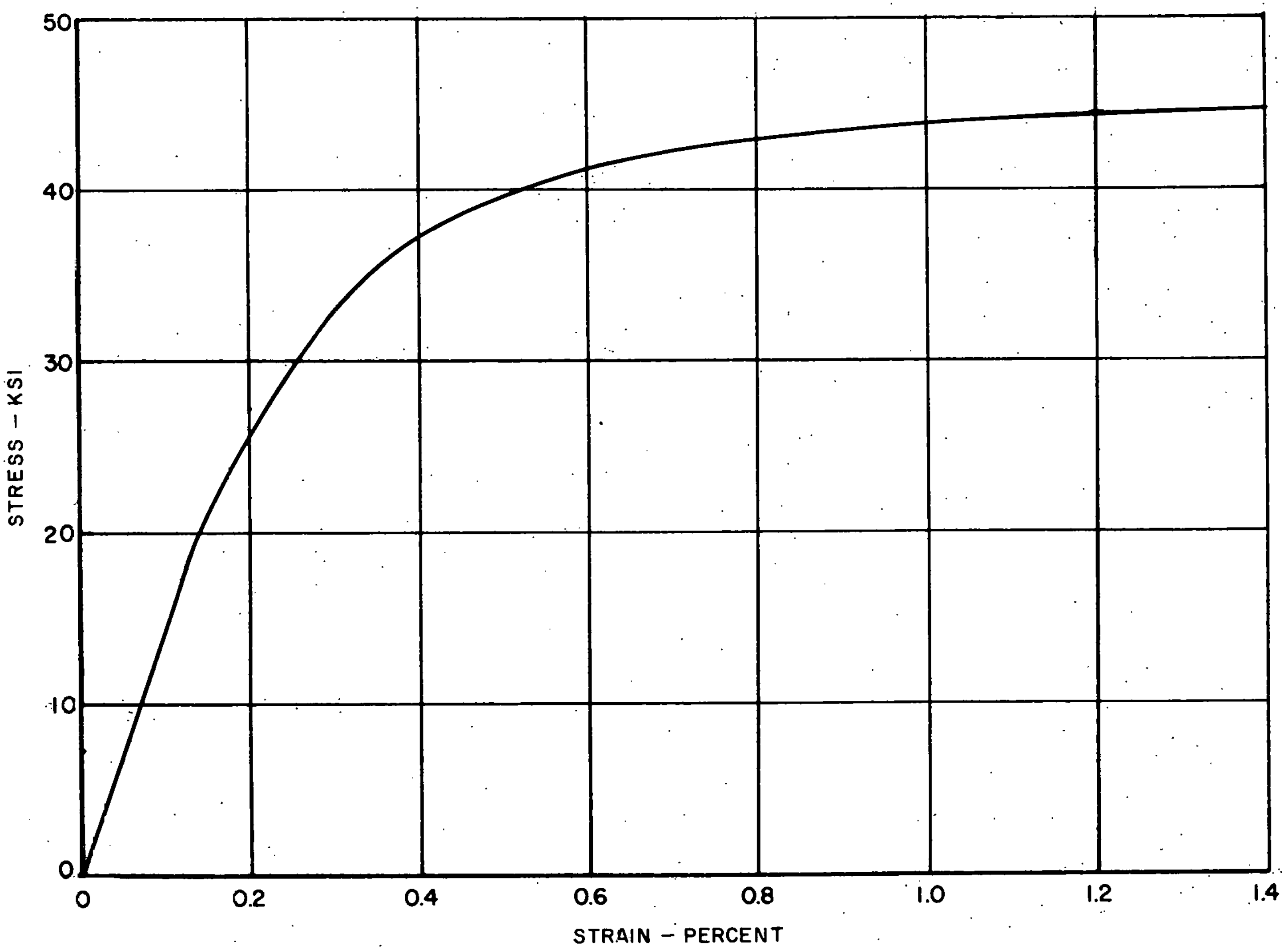

FIG. 8, STATIC STRESS-STRAIN CURVE FOR COPPER

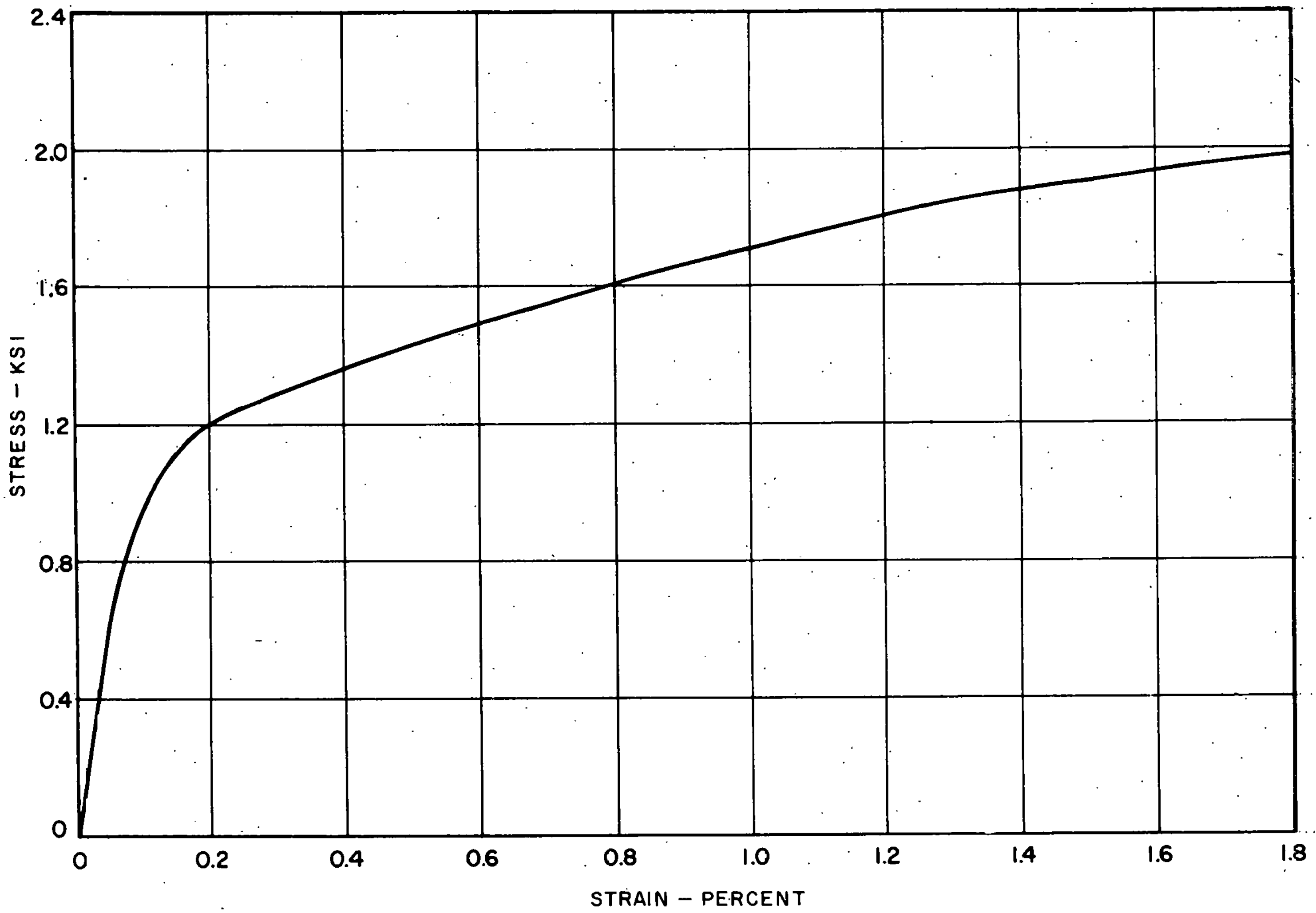

FIG. 9, STATIC STRESS – STRAIN CURVE FOR LEAD

Because of the nature of the equations, it is sometimes more convenient to manipulate the value of V which is determined by the stress, rather than to manipulate the stress itself. For instance, Fig. 10 shows the value of V before and after a stress wave of magnitude σ_i has reflected off a fixed end. Although V_t is equal to $2V_i$, σ_t is less than $2\sigma_i$ if the proportional limit has been exceeded.

Reflection at a semifixed end. Since the pressure bar on which the specimens were mounted is made of steel and has the same diameter as the specimens, it cannot be considered absolutely rigid as compared to copper specimens. Consequently, an analysis that considers the elastic properties of the steel bar must be made.

Consider a stress wave of magnitude σ_i approaching a discontinuity in material as in Fig. 11. The total change in velocity of particles M and N on either side of the discontinuity must be the same since, after the wave reflectes from and passes through the discontinuity, both particles must have the same velocity. The total change in velocity of point M is

$$\Delta V_M = \frac{-1}{\rho_1} \int_0^{\sigma_i} \frac{d\sigma}{C_1} + \frac{1}{\rho_1} \int_{\sigma_i}^{\sigma_t} \frac{d\sigma}{C_1} \qquad \text{- - - - -} \qquad (13)$$

which must be equal to

$$\Delta V_N = \frac{1}{\rho_2} \int_0^{\sigma_t} \frac{d\sigma}{C_2} \qquad \text{- - - - -} \qquad (14)$$

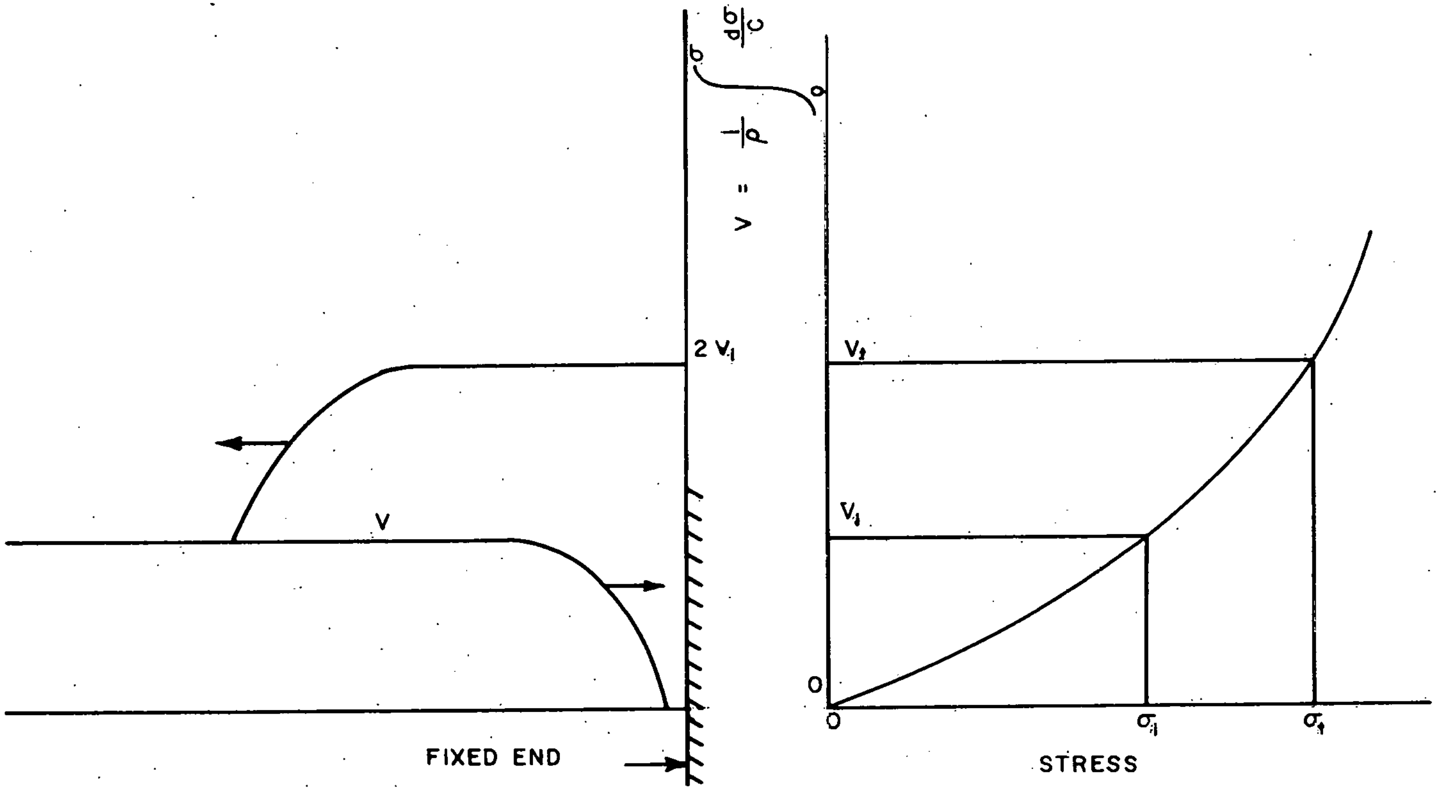

FIG. 10, REFLECTION OF A V-WAVE AT A FIXED END

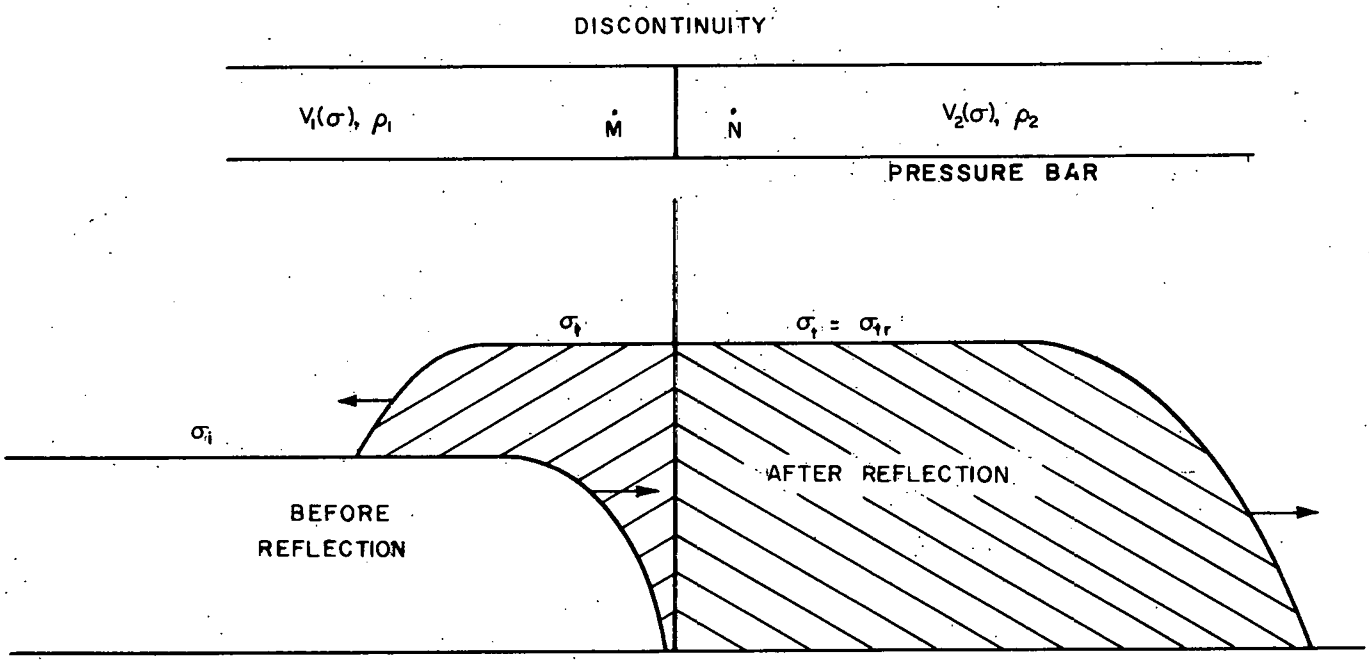

FIG. 11, REFLECTION OF A STRESS WAVE OFF A SEMI-FIXED END

Therefore

$$\frac{1}{\rho_1}\int_0^{\sigma_i}\frac{d\sigma}{C_1} - \left[\frac{1}{\rho_1}\int_0^{\sigma_t}\frac{d\sigma}{C_1} - \frac{1}{\rho_1}\int_0^{\sigma_i}\frac{d\sigma}{C_1}\right] = \frac{1}{\rho_2}\int_0^{\sigma_t}\frac{d\sigma}{C_2} \quad \text{- - - - (15)}$$

or

$$\frac{2}{\rho_1}\int_0^{\sigma_i}\frac{d\sigma}{C_1} = \frac{1}{\rho_1}\int_0^{\sigma_t}\frac{d\sigma}{C_1} + \frac{1}{\rho_2}\int_0^{\sigma_t}\frac{d\sigma}{C_2} \quad \text{- - - - - (16)}$$

In this particular problem C_2 is constant since the yield stress of the steel pressure bar is not exceeded. Therefore, Eq. (16) becomes

$$\frac{2}{\rho_1}\int_0^{\sigma_i}\frac{d\sigma}{C_1} = \frac{1}{\rho_1}\int_0^{\sigma_t}\frac{d\sigma}{C_1} + \frac{\sigma_t}{\rho_2 C_2} \quad \text{- - - - - (17)}$$

which is the equation relating the incident to the resultant stress. It can be solved graphically in the following manner. In Fig. 12, each term of Eq. (17) is plotted as well as the sum of the two terms on the right-hand side. Point (a) on curve B is determined by the magnitude of the incident stress, σ_{i_1}, or the incident particle velocity Vi_1. A line is extended upward until it intersects curve D (point b) which determines $2Vi_1$. The ordinate of point (b) must be equal to the right-hand side of Eq. (17). Therefore, a line drawn

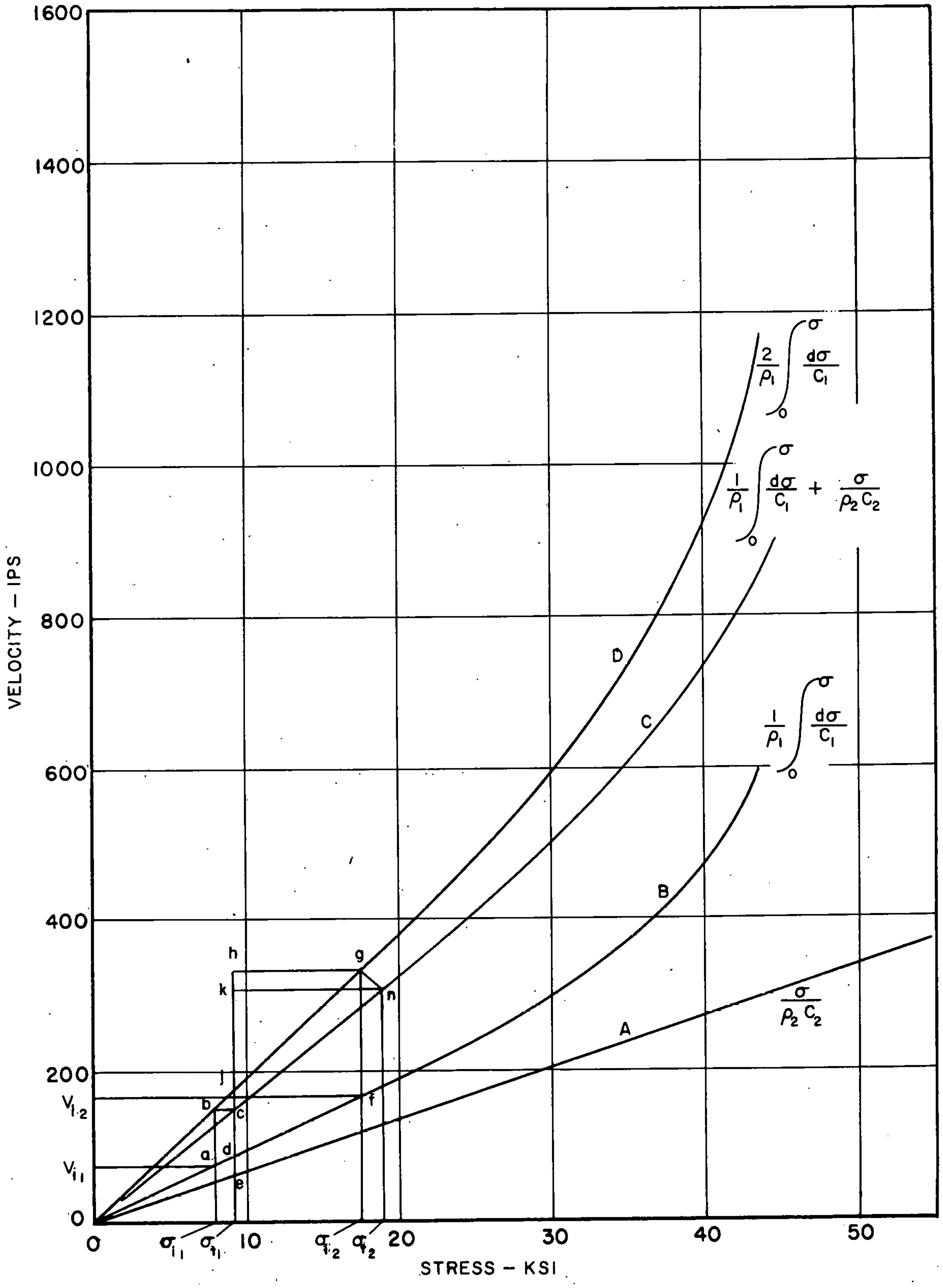

FIG. 12, GRAPHICAL CONSTRUCTION OF WAVE REFLECTED OFF A SEMI-FIXED END.

horizontally from point (b) to curve C determines the value of σ_{t_1} (point c). The magnitude of V_{t_1} and V_{tr_1}, the transmitted particle velocity, is determined by extending a line vertically downward to curves B and A, respectively.

The previously described method must not be used if the material at the discontinuity is already under a state of stress and is in motion as if an earlier stress wave had passed the section. For instance, in Fig. 13, a stress wave σ_{i_1} has passed the discontinuity and has resulted in total and transmitted stresses of σ_{t_1} and σ_{tr_1}, respectively. Another stress wave of magnitude $\sigma_{i_2} - \sigma_{t_1}$ approaches the discontinuity superimposed on σ_{t_1}. The problem is to find σ_{t_2} and σ_{tr_2}. Again, the impulse-momentum principle is used to find the final particle velocity. Before σ_{i_2} arrives, points p and q have equal velocities given by Eq. (13) and (14) or

$$V_{p_1} = -\frac{1}{\rho_1}\int_0^{\sigma_{i_1}} \frac{d\sigma}{C_1} + \frac{1}{\rho_1}\int_{\sigma_{i_1}}^{\sigma_{t_1}} \frac{d\sigma}{C_1} \qquad \text{- - - - -} \quad (18)$$

and

$$V_{q_1} = -\frac{1}{\rho_2}\int_0^{\sigma_{t_1}} \frac{d\sigma}{C_2} = -\frac{\sigma_{t_1}}{\rho_2 C_2} \qquad \text{- - - - -} \quad (19)$$

After the second reflected wave has passed points p and q, the velocities must be

$$V_{p_2} = V_{p_1} - \frac{1}{\rho_1}\int_{\sigma_{t_1}}^{\sigma_{i_2}} \frac{d\sigma}{C_1} + \frac{1}{\rho_1}\int_{\sigma_{i_2}}^{\sigma_{t_2}} \frac{d\sigma}{C_1} \qquad \text{- - - - -} \quad (20)$$

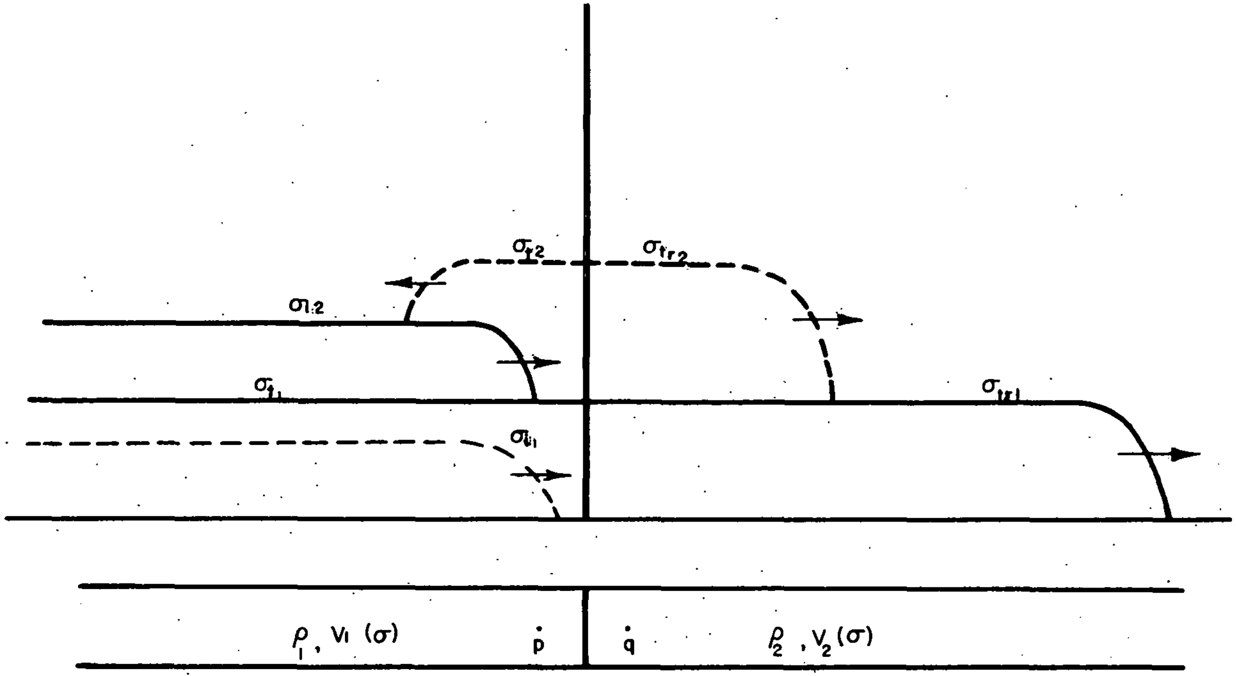

FIG. 13, REFLECTION OF STRESS WAVE OFF A SEMI-FIXED END ALREADY UNDER STRESS and

$$V_{q_2} = V_{q_1} - \frac{1}{\rho_2} \int_{\sigma_{i_1}}^{\sigma_{t_2}} \frac{d\sigma}{C_2} = V_{q_1} - \frac{\sigma_{t_2} - \sigma_{t_1}}{\rho_2 C_2} \qquad --- \qquad (21)$$

Combining Eqs. (18), (19), (20), and (21), and equating the final velocities of points p and q yields

$$\frac{2}{\rho_1} \int_o^{\sigma_{i_1}} \frac{d\sigma}{C_1} + \frac{2}{\rho_1} \int_o^{\sigma_{i_2}} \frac{d\sigma}{C_1} - \frac{2}{\rho_1} \int_o^{\sigma_{t_1}} \frac{d\sigma}{C_1}$$

$$= \frac{1}{\rho_1} \int_o^{\sigma_{t_2}} \frac{d\sigma}{C_1} + \frac{\sigma_{t_2}}{\rho_2 C_2} \qquad ----- \qquad (22)$$

or

$$2V_{a_1} + 2V_{a_2} - 2V_{r_1} = V_{r_2} + V_{t_2} \qquad ----- \qquad (23)$$

where the V's in Eq. (23) are understood to be defined by Eqs. (9) or (22) and are not particle velocities themselves.

The state of the material before the wave σ_{i_2} arrives is determined by σ_{i_1}, which locates points a, b, c, and d in Fig. 12. The ordinate of point b is the first term in Eq. (22). The second term is equal to the ordinate of point g which is determined by σ_{i_2}. Point h is obtained by extending a vertical line through c until it intersects a horizontal line through g. The third term in Eq. (22) is the ordinate of point j and is determined by σ_{t_1}. Therefore, the left side of Eq. (22) must be

$$\overline{oc} + (\overline{oh} - \overline{oj}) = \overline{oc} + \overline{jh} \qquad ----- \qquad (24)$$

If $\overline{ck}$ is laid off to equal $\overline{jh}$ and a line is drawn horizontally from k to curve C, then the ordinate of point n is equal to the right-hand side of Eq. (22) and determines σ_{t_2}, the magnitude of the reflected stress after the passage of the second wave.

This process may be used to construct graphically not only the final value of stress after a wave front has passed, but also the intermediate values if the wave is constructed of finite steps as in Fig. 5.

Meeting of wave fronts. When a stress wave travels down a bar and is partially reflected off a discontinuity, there is a possibility that the reflected portion will meet another front emanating from the original source.* This would produce a situation illustrated in Fig. 14. It is desired to determine the magnitude of the resultant stress, σ_t, propagating away from the meeting point in both directions.

Consider points p and q on either side of the meeting plane m. Before σ_2 and σ_3 approach section m, the velocities of points p and q must be equal and are given by

$$V_{p_1} = V_{q_1} = -\frac{1}{\rho} \int_0^{\sigma_1} \frac{d\sigma}{C} \qquad ----- \qquad (25)$$

---

*The meeting of two stress waves can be thought of as producing a reflection since both the stresses and the particle velocities must be equal across the meeting surface. This requirement produces waves of equal magnitude traveling in opposite directions.

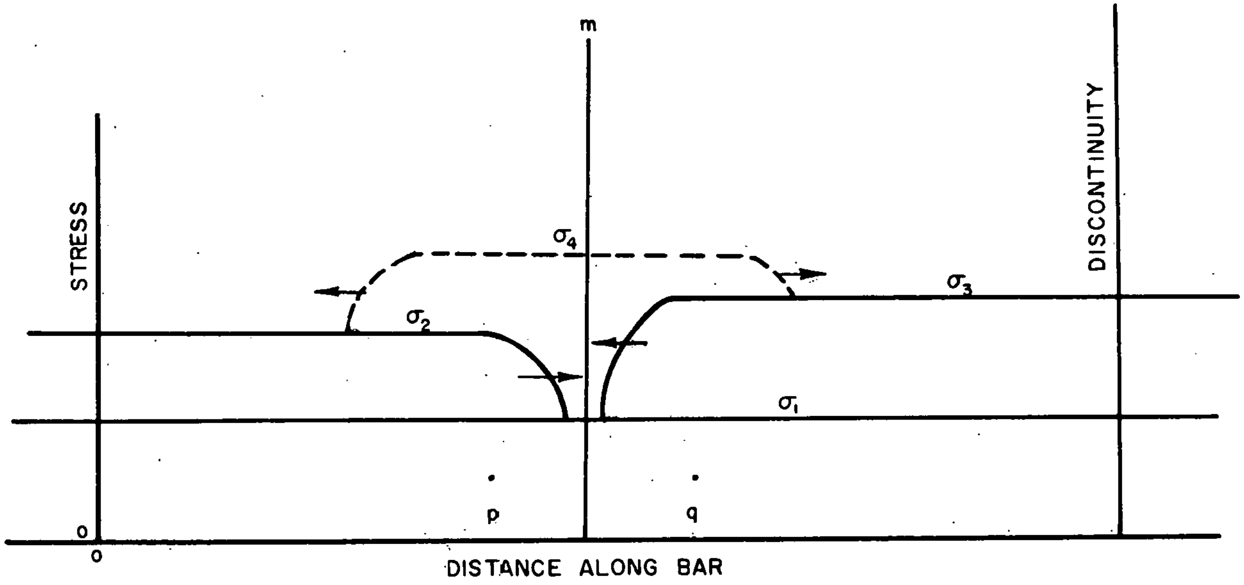

FIG. 14, MUTUAL REFLECTION OF STRESS WAVES

After the wave front generating σ_2 passes point p, V_p becomes

$$V_{p_2} = V_{p_1} - \frac{1}{\rho}\int_{\sigma_1}^{\sigma_2}\frac{d\sigma}{C} = -\frac{1}{\rho}\int_{o}^{\sigma_2}\frac{d\sigma}{C} \qquad \text{- - - - -} \quad (26)$$

The reflected stress wave σ_4 reduces that velocity to

$$\left.\begin{aligned} V_{p_4} &= V_{p_2} + \frac{1}{\rho}\int_{\sigma_2}^{\sigma_4}\frac{d\sigma}{C} \\ V_{p_4} &= -\frac{2}{\rho}\int_{o}^{\sigma_2}\frac{d\sigma}{C} + \frac{1}{\rho}\int_{o}^{\sigma_4}\frac{d\sigma}{C} \end{aligned}\right) \qquad \text{- - - - -} \quad (27)$$

In the meantime, point q has attained a velocity given by

$$\left.\begin{aligned} V_{q_4} &= -\frac{1}{\rho}\int_{o}^{\sigma_1}\frac{d\sigma}{C} + \frac{1}{\rho}\int_{\sigma_1}^{\sigma_3}\frac{d\sigma}{C} - \frac{1}{\rho}\int_{\sigma_3}^{\sigma_4}\frac{d\sigma}{C} \\ V_{q_4} &= -\frac{2}{\rho}\int_{o}^{\sigma_1}\frac{d\sigma}{C} + \frac{2}{\rho}\int_{o}^{\sigma_3}\frac{d\sigma}{C} - \frac{1}{\rho}\int_{o}^{\sigma_4}\frac{d\sigma}{C} \end{aligned}\right) \quad (28)$$

Obviously, the final velocities of points p and q must be equal, therefore equating them yields

$$\frac{1}{\rho}\int_{o}^{\sigma_4}\frac{d\sigma}{C} = \frac{1}{\rho}\int_{o}^{\sigma_2}\frac{d\sigma}{C} + \frac{1}{\rho}\int_{o}^{\sigma_3}\frac{d\sigma}{C} - \frac{1}{\rho}\int_{o}^{\sigma_1}\frac{d\sigma}{C} \qquad (29)$$

Since σ_1, σ_2, and σ_3 are all known, σ_4 may then be computed with the aid of a V versus σ curve such as curve B of Fig. 12.

Diagrams of state. A diagram of state is a graph on which the state of stress of a bar is given as a function of position along the bar and time after impact. Since there are three quantities involved, i. e., stress (or strain), distance, and time; the graph should be three-dimensional in order to visualize its construction.

1. Copper. Fig. 15 is the diagram of state of a commercially pure copper cylinder with one end fixed which has been struck with a rigid projectile moving at a velocity of 780 inches per second (ips). The coordinates of distance and time are nondimensional; distance is given in terms of specimen length, L, and time is in terms of the propagational velocity of the elastic wave, C_o, and the specimen length. The time when the elastic wave reaches the end of the specimen is always unity, regardless of specimen length.

   The stress wave resulting from the impact is approximated by ten finite steps represented by the ten straight lines radiating from the origin in Fig. 15. Each step is traveling at a velocity determined by its position on the stress-strain curve. The velocity in turn determines the slope of the characteristic lines

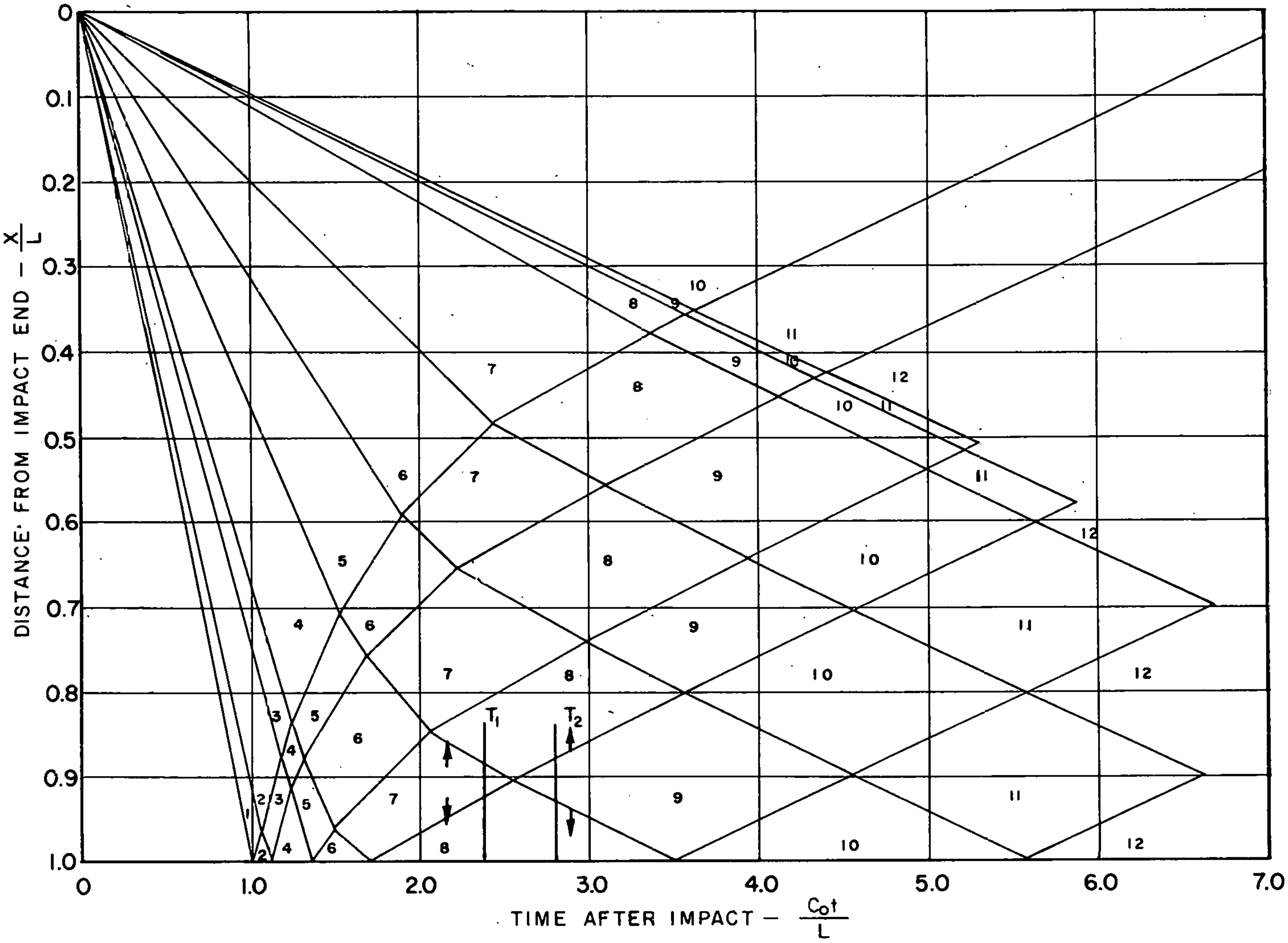

FIG. 15, DIAGRAM OF STATE FOR 65 fps IMPACT ON COPPER SPECIMEN WITH FIXED END.

representing the individual steps. In order to facilitate the construction of the diagram of state, the stress wave is divided into ten equal particle velocity increments of 78 ips each. This enables the stress resulting when a step is reflected off the fixed end or off other steps to be computed with the least effort. It can be seen that the first steps to be reflected off the fixed end interfere with the slower moving steps of the incident wave. The interferences produce higher stresses for both the incident and reflected steps which result in still lower propagational velocities. The lower propagational velocities cause the characteristic lines to be steeper with respect to the distance axis. The resulting figure is a series of polygons whose time durations gradually increase. Each polygon shown in the figure and marked with a number represents a particular state.

For instance, in all polygons marked (7), the stresses and strains are equal and are constant throughout. If the diagram were plotted in three dimensions with stress or strain as the third dimension, each polygon would form a plateau of constant stress or strain. The values of stress, strain, wave velocity, and V (as given by Eq. (9)) are given in Table I for

TABLE I. Data for Figure 15

Plateau	V in./sec	ε in./in.	C_{avg} in./sec	σ psi	$\frac{1}{C}$ µsec/in.	$\frac{C_o}{C}$
1	78	.00055	138,000	8,200	7.25	1.02
2	156	.0011	127,000	16,000	7.88	1.11
3	234	.0019	105,000	24,800	9.53	1.34
4	312	.0028	87,000	31,700	11.50	1.62
5	390	.0039	65,000	36,900	15.40	2.17
6	468	.0055	44,000	40,500	22.80	3.21
7	546	.0076	28,000	42,900	35.70	5.02
8	624	.0120	16,000	44,400	62.50	8.80
9	702	.0156	14,200	45,400	70.40	9.90
10	780	.0200	13,800	46,400	72.50	10.21
11	858	.0244	13,500	47,400	74.10	10.44

each numbered polygon. The reflections of each step off the fixed end and off later arriving steps were computed by the general method described previously.

An example of the use of the method of computing the resultant stress when two waves traveling in opposite directions meet is as follows. The stress distribution at the time represented by the line T_1 in Fig. 15 is similar to that described in Fig. 14 by the solid lines with the exception that here the two waves meeting are equal. The situation in Figs. 14 and 15 would be identical if σ_1, σ_2, σ_3, and σ_4 were replaced by σ_7, σ_8, σ_8, and σ_9 respectively. It follows from previous analysis that

$$\frac{1}{\rho}\int_0^{\sigma_9}\frac{d\sigma}{C} = \frac{2}{\rho}\int_0^{\sigma_8}\frac{d\sigma}{C} - \frac{1}{\rho}\int_0^{\sigma_7}\frac{d\sigma}{C} \quad \text{- - - - -} \quad (30)$$

which may be solved using the V versus σ curve for copper in Fig. 12. The distribution after the waves meet is as given by the line T_2 which corresponds to the dotted line in Fig. 14.

The diagram of state is useful in that it portrays the strain-time history of each point in the rod, and also the strain distribution throughout the bar at any time after impact. For example, if the stress and strain histories at the fixed end were wanted, the values given in Table I for the polygons intersected by the line $x/L = 1$ would be plotted versus time. Such a plot would result in the stress and strain-time curves approximated by the steps shown in Fig. 16. The histories at any other point in the bar could have been found by drawing a line parallel to the time axis through the point in question. The intersection of that

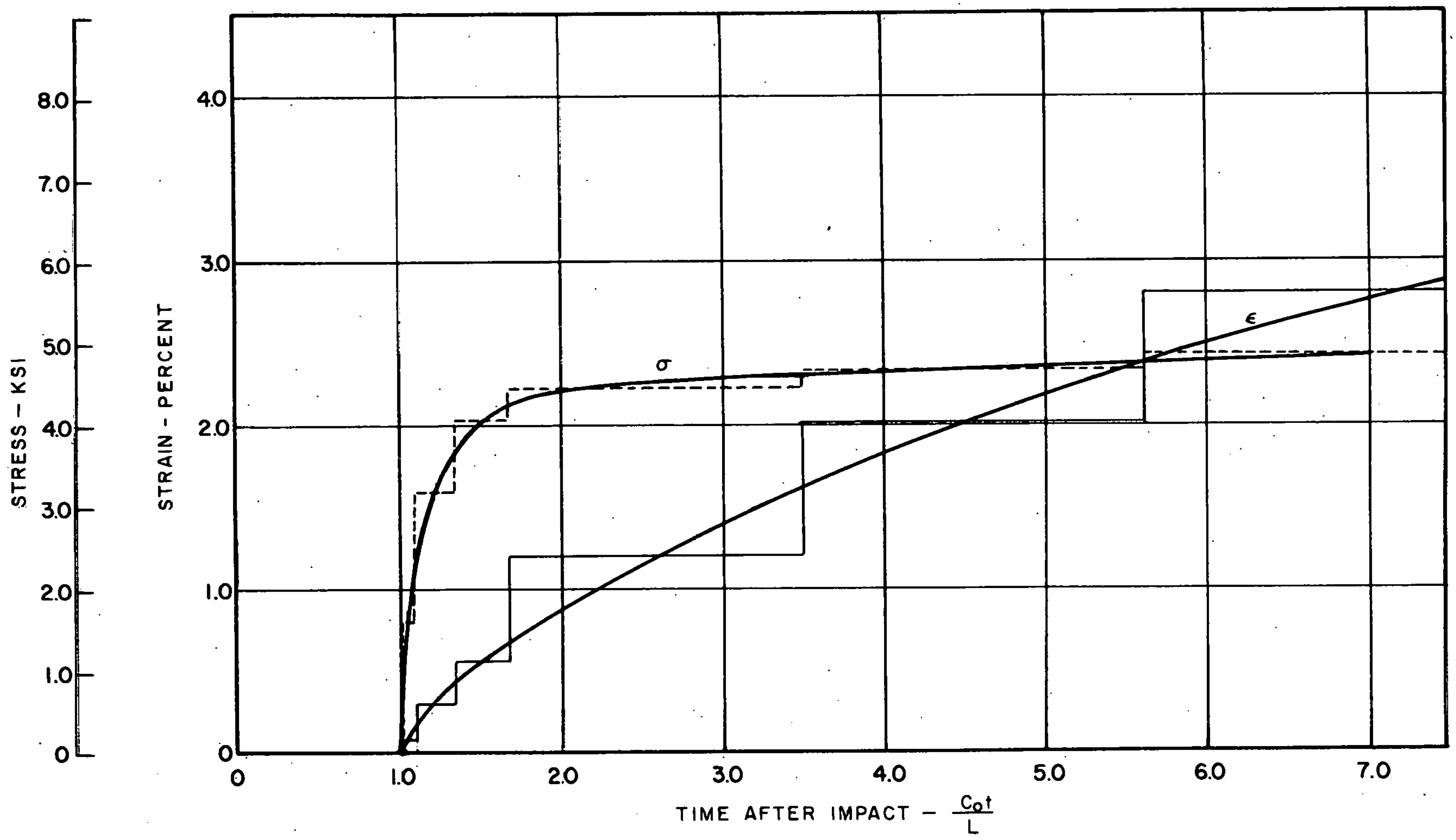

FIG. 16, STRESS AND STRAIN TIME HISTORY FOR COPPER SPECIMEN WITH FIXED END line with the polygons and the values of the polygons would determine the required history. A plot consisting of finite steps would be produced. Smooth curves could be drawn through the steps to represent the actual history.

The diagram of state for a copper specimen which will more nearly coincide with the physical problem is one in which the elastic properties of the steel pressure bar are considered. Such a diagram is shown in Fig. 17. There appears to be little difference between Fig. 17 and Fig. 15 where the end was considered fixed; however, the characteristic lines near the position $x/L = 1$ in Fig. 17 are steeper with respect to the time axis which indicates higher propagational velocities and, hence, lower strains as can be seen in Fig. 18. Fig. 18 shows the stress and strain history for the copper at the elastic bar end of the specimen.

Table II lists the information concerning each plateau in the diagram of state in Fig. 17.

The diagrams in Figs. 15 and 17 are for impact velocities of 780 ips. If the diagram is desired for any other impact velocity, say 390 ips, then of the steps emanating from the impact end, only those corresponding to V = 390 ips and below should be considered. If Fig. 17 were to be used for an impact velocity of 390 ips, the

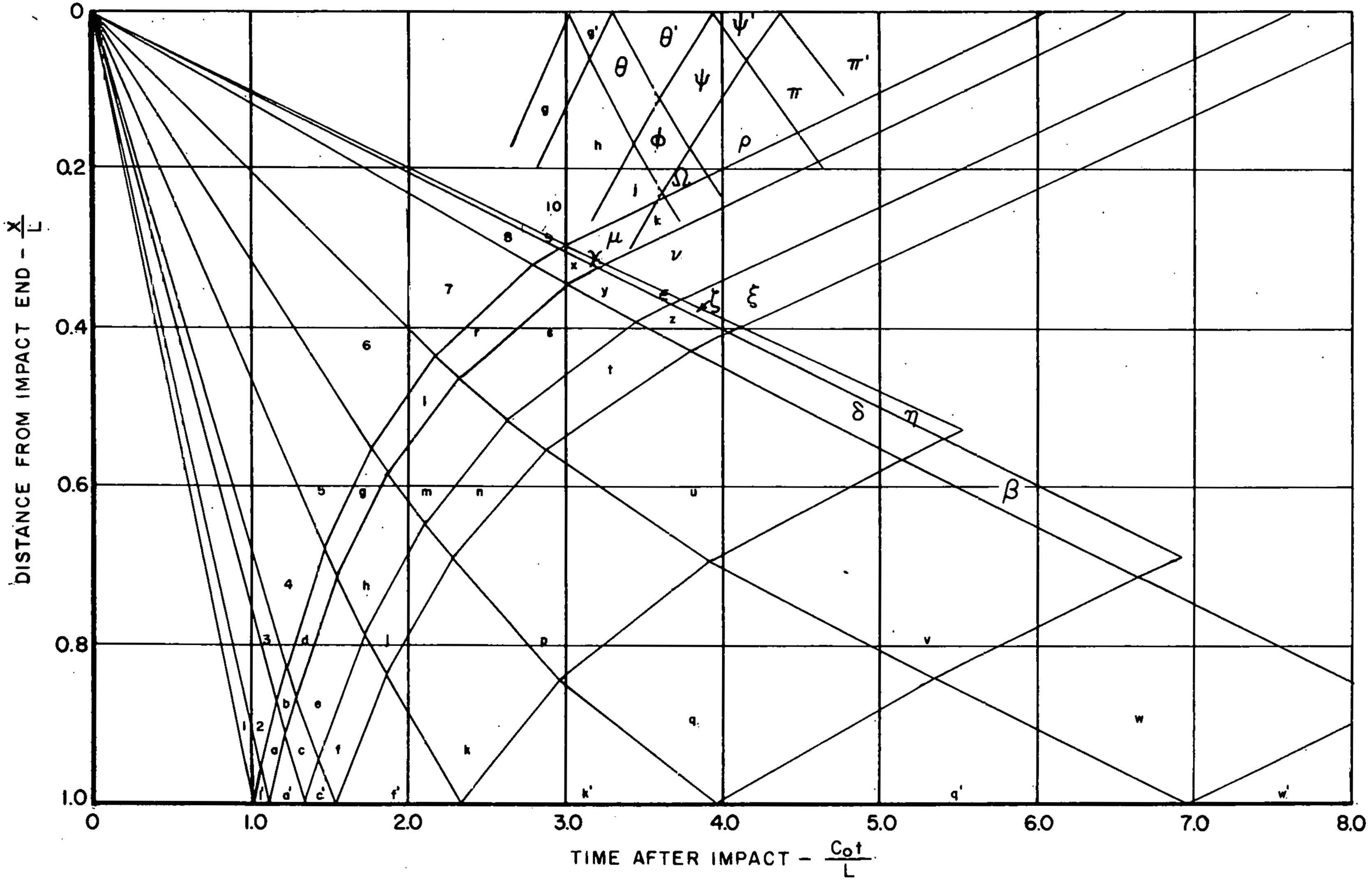

FIG. 17, DIAGRAM OF STATE FOR 65 fps IMPACT ON COPPER SPECIMEN WITH SEMI-FIXED END

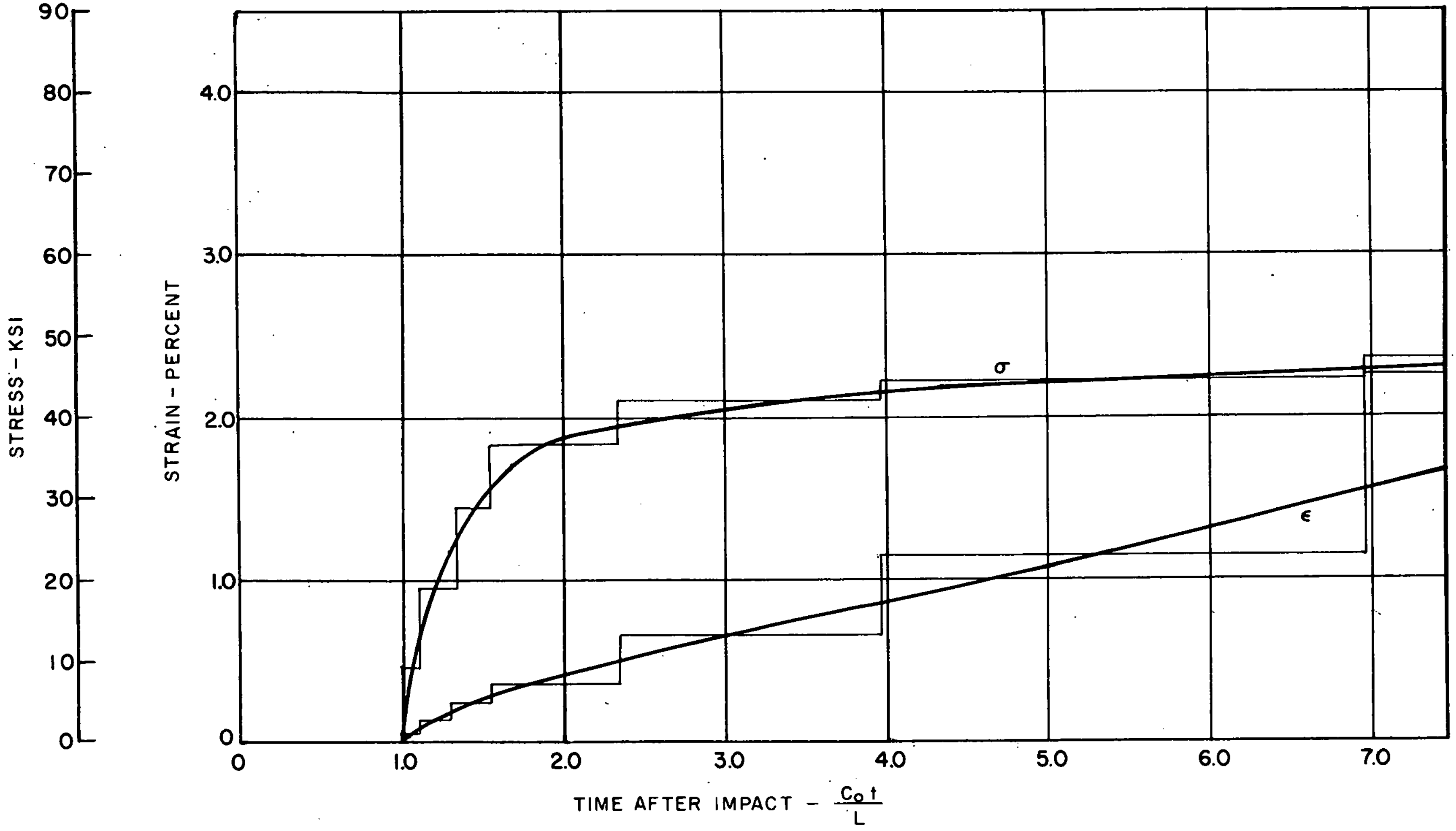

FIG. 18, STRESS AND STRAIN HISTORY FOR COPPER SPECIMEN AT SEMI-FIXED END

TABLE II. Data for Figure 17

Plateau	V ips	ε%	σ psi	C ips	$\frac{C_o}{C}$
l	78	.055	8,200	138,000	1.02
l'	89	.063	9,200	136,500	1.04
a	167	.120	17,600	125,000	1.14
a'	180	.133	19,000	122,000	1.15
b	245	.200	25,700	103,000	1.37
c	258	.220	27,400	99,000	1.42
c'	278	.240	28,900	95,000	1.48
d	323	.295	32,600	84,500	1.67
e	336	.312	33,500	81,500	1.73
f	356	.341	35,000	75,500	1.87
f'	368	.357	36,700	70,200	2.00
g	401	.410	37,500	62,000	2.28
h	414	.435	38,200	58,000	2.43
j	434	.480	39,200	51,500	2.74
k	446	.500	39,600	49,000	2.88
k'	510	.651	42,000	35,000	4.02
L	479	.580	41,000	41,000	3.44
m	492	.610	41,300	38,500	3.66
n	512	.657	42,000	35,000	4.02
p	524	.695	42,300	32,000	4.40
q	588	.900	43,600	22,000	6.40
q'	630	1.15	44,200	16,000	8.80
r	557	.800	43,200	26,000	5.40
s	570	.850	43,500	24,000	5.86
t	590	.930	43,700	21,000	6.70
u	602	.990	43,800	19,000	7.40

TABLE II. Data for Figure 17
(Cont'd)

Plateau	V ips	ε%	σ psi	C ips	$\frac{C_o}{C}$
v	666	1.35	44,800	14,500	9.7
w	708	1.59	45,500	14,000	10.1
x	635	1.18	44,400	15,800	8.9
y	648	1.26	44,600	15,000	9.4
z	668	1.35	44,800	14,500	9.7
w'	825	2.25	47,000	13,500	10.4
α	680	1.43	45,000	14,500	9.7
β	744	1.80	46,000	14,000	10.1
γ	786	2.03	46,400	13,800	10.2
Δ	713	1.53	45,300	14,200	9.9
ε	726	1.69	45,700	14,000	10.1
ζ	756	1.86	46,100	14,000	10
η	768	1.93	46,400	14,000	10
λ	832	2.30	47,000	13,500	10.4
μ	791	2.06	47,000	13,500	10.4
ν	804	2.10	47,000	13,500	10.4
ξ	834	2.4	48,000	13,000	10.8
g'	412	.434	38,200	58,000	2.43
θ	425	.460	38,800	54,000	2.61
θ'	438	.485	39,300	51,000	2.76
ϕ	445	.500	39,600	49,000	2.88
ψ	458	.530	40,200	46,000	3.06
ψ'	478	.580	41,000	41,000	3.44
Ω	457	.530	40,200	46,000	3.06
ρ	470	.550	40,500	44,000	3.21
π	490	.600	41,200	39,000	3.62
π'	502	.635	41,700	36,500	3.86

characteristic lines separating polygons 5, g, h, j, k, and k' must be extended without regard for any line resulting from steps 6 through 10. The continuations of those lines and their subsequent reflections off the impact end are shown in Fig. 17. It is seen that for an impact velocity of 390 ips the first reflection gets back to the impact end in three times the time it takes the elastic wave to travel the length of the bar, whereas for an impact velocity of 780 ips, a much longer time is required.

2. Lead. The diagram of state for an impact velocity of 120 ips on a specimen of tellurium lead is shown in Fig. 19. In the computations the bar end of the specimen was considered fixed since the relative stiffness of the steel bar is very large as compared to that of the lead.

Table III contains the pertinent information for each polygon in the figure.

The stress and strain occurring at the bar end of the specimen are shown in Fig. 20. The quantities are plotted in the nondimensional time units previously described. An interesting result of the diagram of state for lead is that the strain-time curve increases linearly up to 0.5 per cent strain, but then increases much more rapidly. This sudden increase in strain rate is caused by the arrival of several wave steps in quick succession which is the result of their propagational velocities

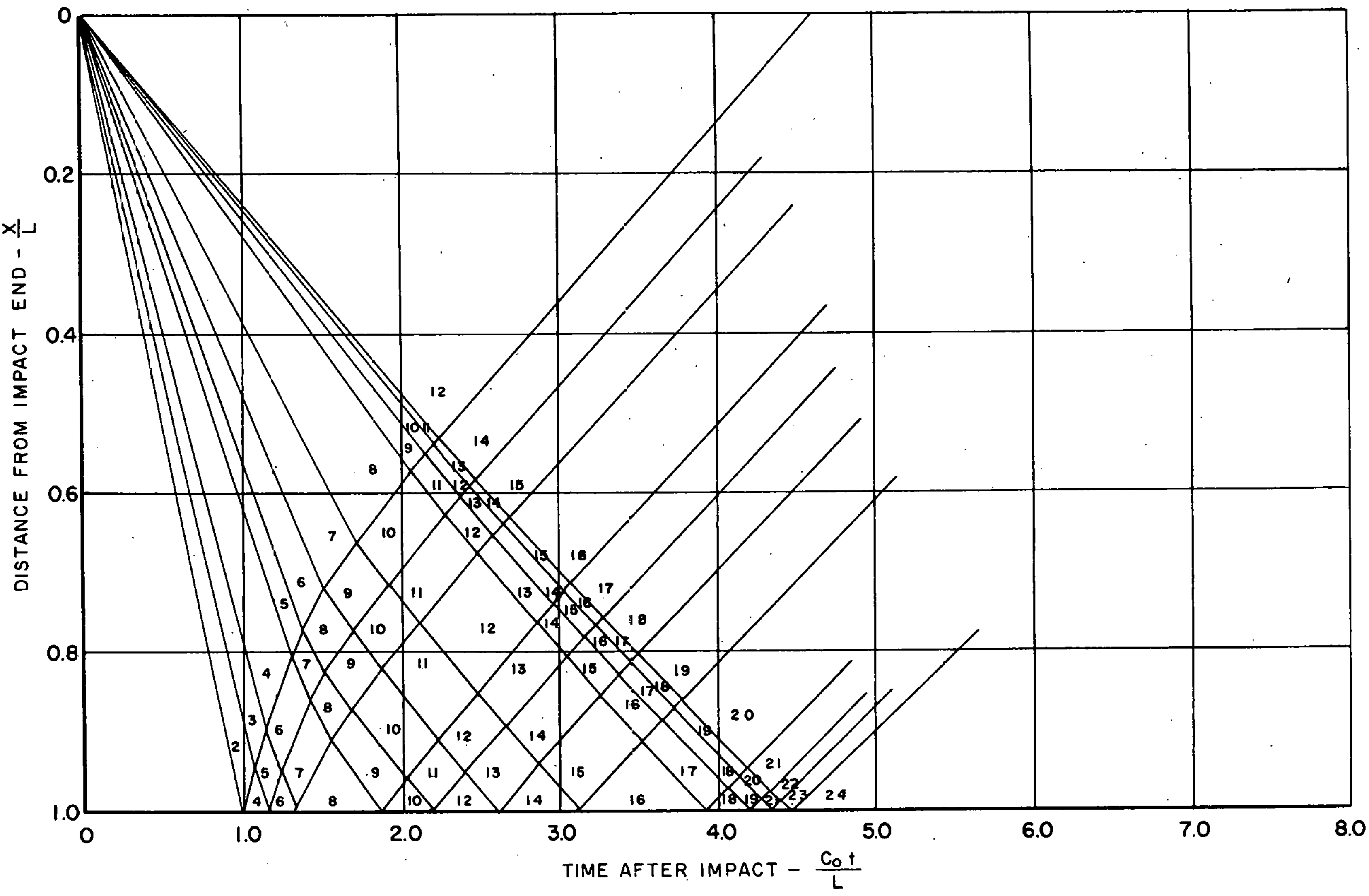

FIG. 19, DIAGRAM OF STATE FOR 10 fps IMPACT ON LEAD WITH FIXED END

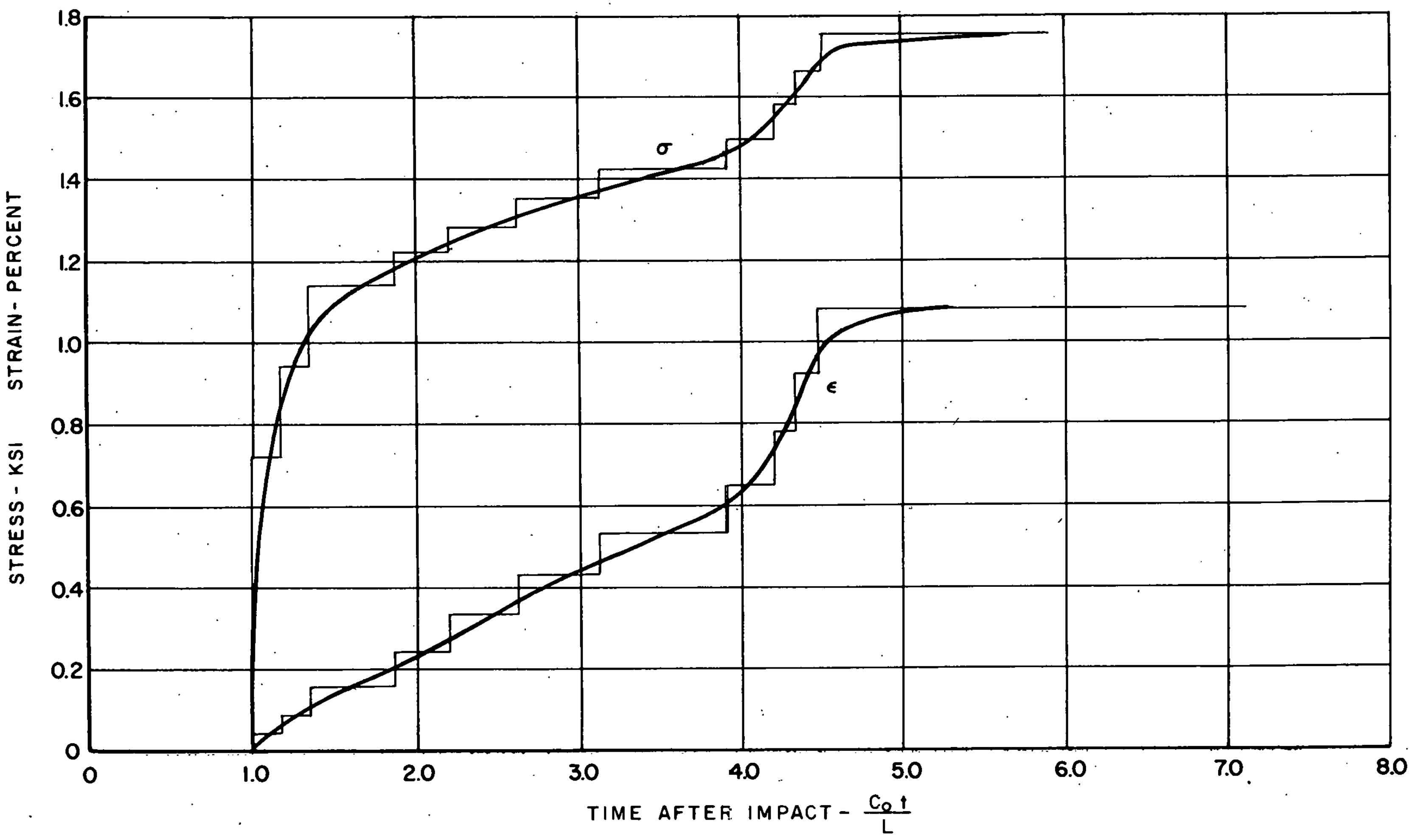

FIG. 20, STRESS AND STRAIN HISTORY FOR LEAD AT FIXED END being very nearly equal. The nearness of the propagational velocities is caused by the fact that the static stress-strain curve has a portion which is very nearly a straight line as can be seen in Fig. 9.

TABLE III. Data for Figure 19

Step	V ips	ε %	σ psi	C ips	$\frac{C_o}{C}$
1	5	.020	240	36,200	1.000
2	10	.030	390	35,800	1.011
3	15	.045	595	31,750	1.141
4	20	.060	720	28,200	1.283
5	25	.080	850	22,100	1.637
6	30	.100	940	20,200	1.791
7	35	.125	1040	17,150	2.11
8	40	.160	1140	13,500	2.68
9	45	.195	1190	10,000	3.62
10	50	.240	1220	9,300	3.89
11	55	.284	1250	8,900	4.07
12	60	.330	1280	8,600	4.21
13	65	.377	1320	8,350	4.33
14	70	.428	1350	8,100	4.47
15	75	.478	1380	7,950	4.55
16	80	.530	1420	7,800	4.64
17	85	.584	1455	7,680	4.71
18	90	.644	1495	7,600	4.76
19	95	.708	1540	7,520	4.82
20	100	.775	1580	7,420	4.88

TABLE III
(cont'd)

Step	V ips	ε%	σ psi	C ips	$\frac{C_o}{C}$
21	105	.843	1620	7310	4.95
22	110	.920	1660	7150	5.07
23	115	.995	1700	6980	5.18
24	120	1.08	1750	6750	5.37
25	125	1.17	1790	6500	5.57
26	130	1.26	1840	6200	5.84
27	135	1.35	1860	5900	6.14
28	140	1.45	1885	5600	6.47
29	145	1.56	1910	5200	6.96
30	150	1.68	1940	4800	7.55
31	155	1.81	1970	4300	8.43
32	160	1.94	2000	3900	9.29
33	165	2.08	2030	3700	9.78

Effects of changes in σ-ε curve. If a material under study is thought to be strain-rate dependent, that is, the stress is a function of strain rate as well as strain, then the static stress-strain curve will not determine the state of the material subjected to impact. In an effort to determine what effect a change in the stress-strain curve has on the results as predicted by the elementary theory, another diagram of state and hence, strain-time curve, was constructed using a stress-strain curve which was only slightly different from the one used previously for lead. The second stress-strain curve used had the same shape as the first except that the yield stress and all stresses beyond yield were increased approximately 450 psi. The two curves are shown in Fig. 21. Curve B in the figure can be thought of as that curve resulting when a specimen which is strain-rate sensitive is strained at a high rate. It is, therefore, a dynamic stress-strain curve.

The sensitivity of strain and stress-time curves to changes in the stress-strain curve are shown in Fig. 22. This figure shows the stress and strain in the material at the bar end of the specimen as a function of time. The curves are labeled according to the stress-strain curve used to compute them.

It is obvious that changing the stress-strain curve affects both the stress and strain at the bar end, but it is especially significant that the change affects the stress much more than the strain. This indicates that strain alone is not a good criterion by which to judge the validity of the nonstrain-rate theory.

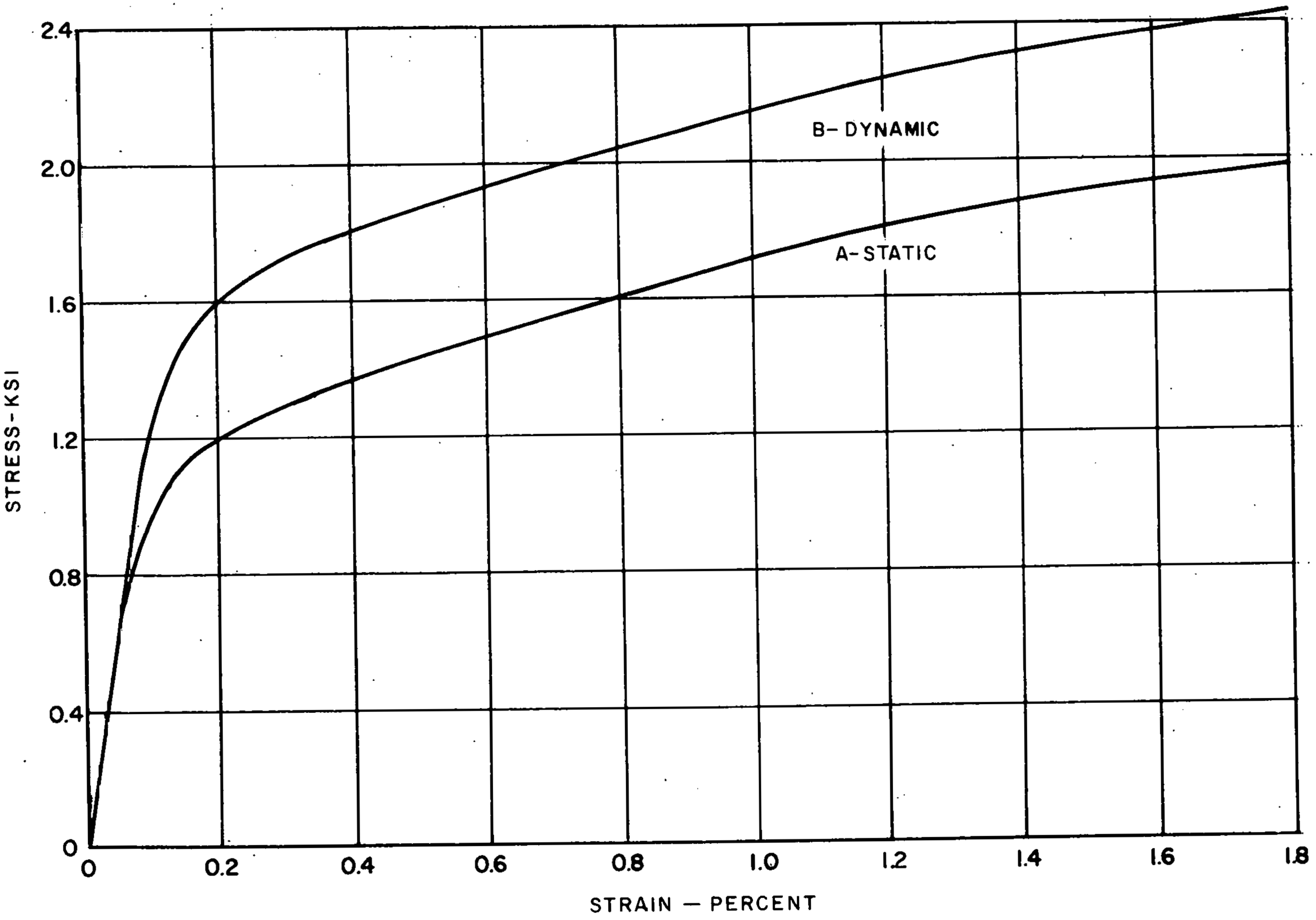

FIG. 21, STATIC AND "DYNAMIC" STRESS - STRAIN CURVES FOR LEAD

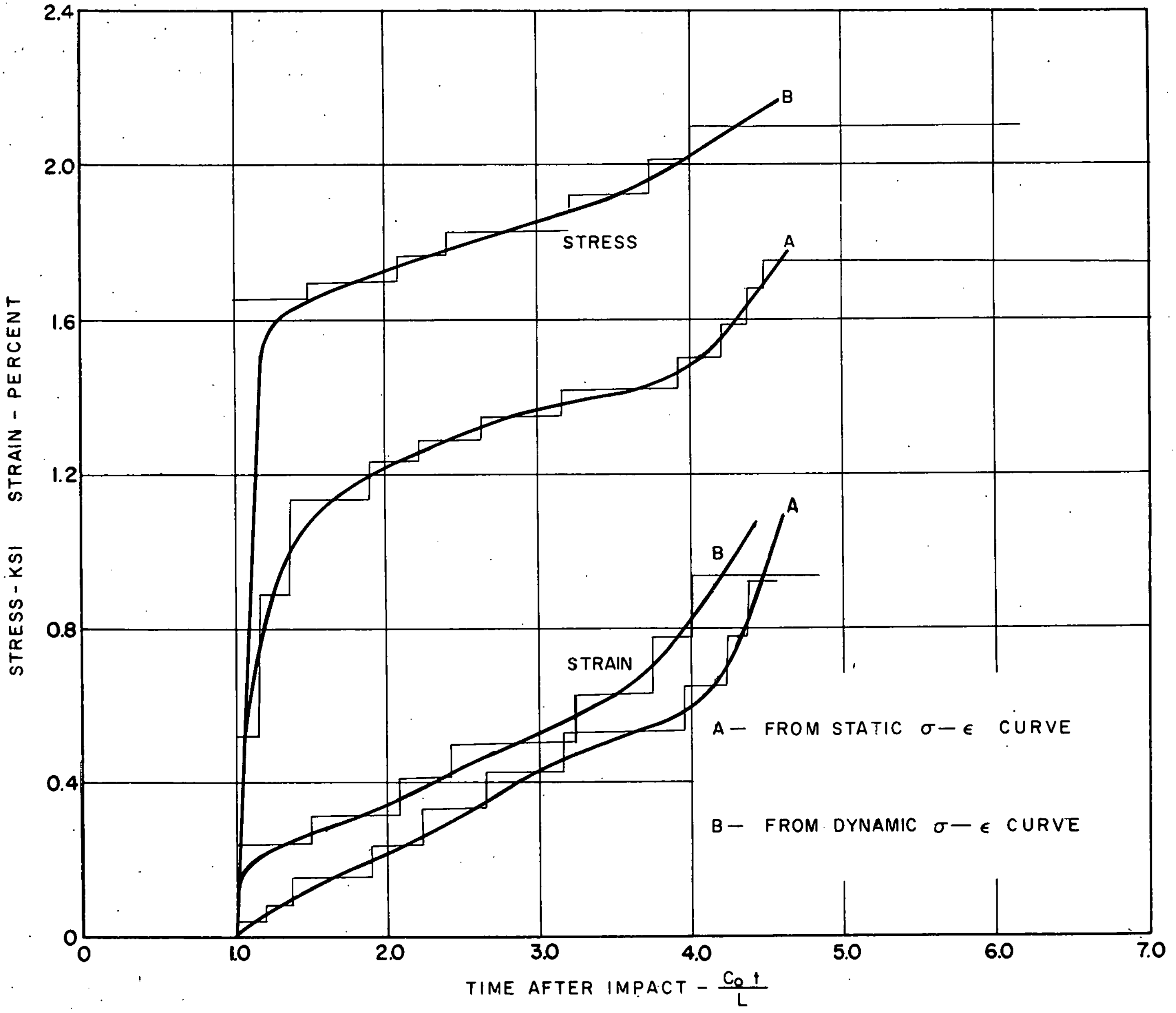

FIG. 22, EFFECTS OF CHANGING THE STRESS-STRAIN CURVE

Strain-Rate Theory

A material in which the stress depends not only on the strain but also on the strain rate is said to be strain-rate sensitive. In such material, the stress is assumed to be

$$\sigma = F(\varepsilon'', \dot{\varepsilon}'') \tag{31}$$

where ε'' is the plastic strain and $\dot{\varepsilon}''$ is the plastic strain rate. The elastic stress is assumed to be independent of strain rate, therefore

$$\dot{\sigma} = E\dot{\varepsilon}' \tag{32}$$

where $\dot{\varepsilon}'$ is the elastic strain rate. If, in Eq. (31) σ is an increasing function of ε'' and $\dot{\varepsilon}''$, then

$$\dot{\varepsilon}'' = G(\sigma, \varepsilon) \tag{33}$$

will be single-valued and can be obtained, where ε is the total strain. Combining Eqs. (32) and (33), the total strain rate becomes

$$\dot{\varepsilon} = \frac{\dot{\sigma}}{E} + G(\sigma, \varepsilon) \tag{34}$$

The above equation may also be written as

$$E\dot{\varepsilon} = \dot{\sigma} + g(\sigma, \varepsilon) \tag{35}$$

where

$$g(\sigma, \varepsilon) = EG(\sigma, \varepsilon) \tag{36}$$

Since the strain ε is defined as

$$\varepsilon = \frac{\partial u}{\partial x} \qquad \text{-----} \quad (37)$$

where u is the displacement, the strain rate is

$$\frac{\partial \varepsilon}{\partial t} = \frac{\partial}{\partial t} \frac{\partial u}{\partial x} = \frac{\partial v}{\partial x} \qquad \text{-----} \quad (38)$$

where v is the particle velocity. Thus the propagation, according to the strain-rate theory, is described by the following three equations.

$$\frac{\partial \sigma}{\partial x} - \rho \frac{\partial v}{\partial t} = 0 \quad \text{Equation of Motion} \qquad \text{-----} \quad (39)$$

$$\frac{\partial \varepsilon}{\partial t} - \frac{\partial v}{\partial x} = 0 \quad \text{Equation of Continuity} \qquad \text{-----} \quad (40)$$

$$E \frac{\partial \varepsilon}{\partial t} - \frac{\partial \sigma}{\partial t} = g(\sigma, \varepsilon) \quad \text{Equation of Material Behavior} \qquad \text{-----} \quad (41)$$

The function $g(\sigma, \varepsilon)$ describes the flow or strain rate which would occur if a constant magnitude stress were applied to the material. This function is assumed to be of the form

$$g(\sigma, \varepsilon) = K(\sigma - \sigma_s) \qquad \text{-----} \quad (42)$$

where $\sigma_s = f(\varepsilon)$ is the "static" stress-strain relationship or the stress-strain curve obtained at a very low strain rate. The function described in Eq. (42) is a linear approximation of the more general strain-rate theory formulated by Prandtl[6] which was

$$g(\sigma, \varepsilon) = K_1 \left[\exp \left(\frac{\sigma - \sigma_s}{K_2} \right) - 1 \right] \quad \text{- - - - -} \quad (43)$$

The linear approximation is made to greatly simplify the numerical computations.

The equations can be solved by the method of characteristics and in order to facilitate finite difference computation with a digital computer the equations are nondimensionalized by introducing the following definitions and notations.

$$\bar{\sigma} = \frac{\sigma}{E}$$

$$\bar{\varepsilon} = \varepsilon$$

$$\bar{v} = \frac{v}{C_o}$$

$$\bar{t} = \frac{C_o t}{L}$$

$$\bar{x} = \frac{x}{L}$$

$$\bar{K} = \frac{KL}{C_o}$$

where: σ = actual stress - lb/in.^{2}

E = elastic modulus - lb/in.^{2}

ε = strain - nondimensional

v = partial velocity - in./sec

$C_o = \sqrt{E/\rho}$ = bar velocity - in./sec

t = time - sec

L = specimen length - in.

x = distance from impact end - in.

K = flow constant - 1/sec

After Eq. (42) and the nondimensional parameters are substituted into Eqs. (39), (40), and (41), the following equations are obtained:

$$\frac{\partial \bar{\sigma}}{\partial \bar{x}} - \frac{\partial \bar{v}}{\partial \bar{t}} = 0 \qquad \text{-----} \qquad (44)$$

$$\frac{\partial \bar{v}}{\partial \bar{x}} - \frac{\partial \bar{\varepsilon}}{\partial \bar{t}} = 0 \qquad \text{-----} \qquad (45)$$

$$\frac{\partial \bar{\varepsilon}}{\partial \bar{t}} - \frac{\partial \bar{\sigma}}{\partial \bar{t}} = \bar{K}\ (\bar{\sigma} - \bar{\sigma}_s) \qquad \text{-----} \qquad (46)$$

The solution of the differential equations by the method of characteristics involves obtaining the total derivatives of the dependent variables $\bar{\sigma}$, $\bar{\varepsilon}$, and $\bar{v}$ along some arbitrary curve in the x - t plane expressed in parametric form as

$$\left.\begin{aligned} \bar{x} &= \bar{x}(w) \\ \bar{t} &= \bar{t}(w) \end{aligned}\right) \qquad \text{-----} \qquad (47)$$

The total derivatives are obtained with respect to the parameter w and are

$$\frac{d\bar{\sigma}}{dw} = \frac{\partial\bar{\sigma}}{\partial\bar{x}} \frac{d\bar{x}}{dw} + \frac{\partial\bar{\sigma}}{\partial\bar{t}} \frac{d\bar{t}}{dw} \qquad \text{- - - - - (48)}$$

$$\frac{d\bar{\varepsilon}}{dw} = \frac{\partial\bar{\varepsilon}}{\partial\bar{x}} \frac{d\bar{x}}{dw} + \frac{\partial\bar{\varepsilon}}{\partial\bar{t}} \frac{d\bar{t}}{dw} \qquad \text{- - - - - (49)}$$

$$\frac{d\bar{v}}{dw} = \frac{\partial\bar{v}}{\partial\bar{x}} \frac{d\bar{x}}{dw} + \frac{\partial\bar{v}}{\partial\bar{t}} \frac{d\bar{t}}{dw} \qquad \text{- - - - - (50)}$$

The above equations along with Eqs. (44), (45), and (46) are six equations which include six first derivatives, one of each dependent variable with respect to x and t. The equations are written in matrix form as follows:

$$\begin{bmatrix} \frac{d\bar{x}}{dw} & \frac{d\bar{t}}{dw} & 0 & 0 & 0 & 0 \\ 0 & 0 & \frac{d\bar{x}}{dw} & \frac{d\bar{t}}{dw} & 0 & 0 \\ 0 & 0 & 0 & 0 & \frac{d\bar{x}}{dw} & \frac{d\bar{t}}{dw} \\ 1 & 0 & 0 & 0 & 0 & -1 \\ 0 & 0 & 0 & -1 & 1 & 0 \\ 0 & -1 & 0 & 1 & 0 & 0 \end{bmatrix} \begin{bmatrix} \frac{\partial\bar{\sigma}}{\partial\bar{x}} \\ \frac{\partial\bar{\sigma}}{\partial\bar{t}} \\ \frac{\partial\bar{\varepsilon}}{\partial\bar{x}} \\ \frac{\partial\bar{\varepsilon}}{\partial\bar{t}} \\ \frac{\partial\bar{v}}{\partial\bar{x}} \\ \frac{\partial\bar{v}}{\partial\bar{t}} \end{bmatrix} = \begin{bmatrix} \frac{d\bar{\sigma}}{dw} \\ \frac{d\bar{\varepsilon}}{dw} \\ \frac{d\bar{v}}{dw} \\ 0 \\ 0 \\ \bar{K}(\bar{\sigma} - \bar{\sigma}_s) \end{bmatrix} \qquad \text{- - (51)}$$

The resulting set of linear differential equations can be solved for each of the unknowns unless the determinant of their coefficients vanishes. The zeros of the determinant yield the characteristics across which discontinuities must exist if they are present at all. The characteristics of Eqs. 51 are

$$\left.\begin{aligned} d\bar{x} &= 0 \\ d\bar{x} &= d\bar{t} \\ d\bar{x} &= -\,d\bar{t} \end{aligned}\right) \qquad \text{-----} \qquad (52)$$

These characteristics are shown in the x-t plane in Fig. 23.

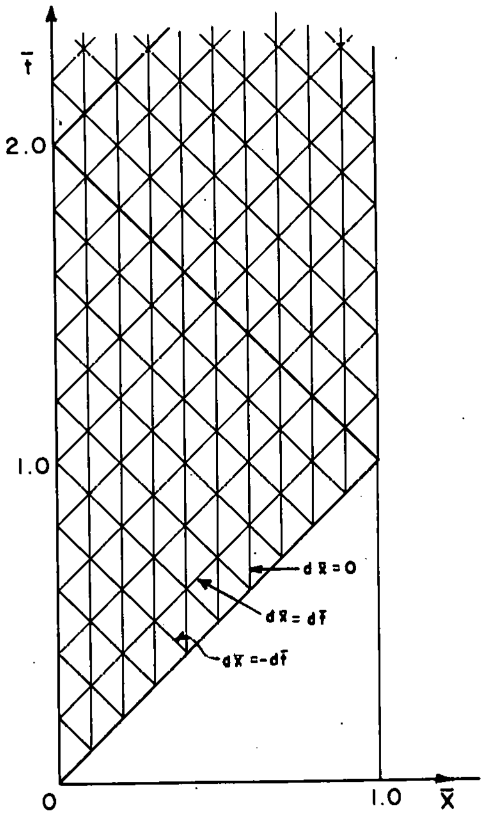

FIG. 23 CHARACTERISTICS IN THE $\bar{X}-\bar{t}$ PLANE

Along these characteristics, Eqs. (44), (45), and (46) reduce to total differential equations given by the following.

$$d\bar{\epsilon} - d\bar{\sigma} = \bar{K}(\bar{\sigma} - \bar{\sigma}_s)\, d\bar{t} \text{ along } d\bar{x} = 0 \qquad \text{-----} \qquad (53)$$

$$d\bar{\sigma} - d\bar{v} = -\bar{K}(\bar{\sigma} - \bar{\sigma}_s)\, d\bar{t} \text{ along } d\bar{x} = d\bar{t} \qquad \text{-----} \qquad (54)$$

$$d\bar{\sigma} + d\bar{v} = -\bar{K}(\bar{\sigma} - \bar{\sigma}_s)\, d\bar{t} \text{ along } d\bar{x} = -d\bar{t} \qquad \text{-----} \qquad (55)$$

These equations can be solved by writing them as finite-difference equations expressing the changes in the variables along the prescribed characteristics. Fig. 24 shows a portion of the network of Fig. 23. If

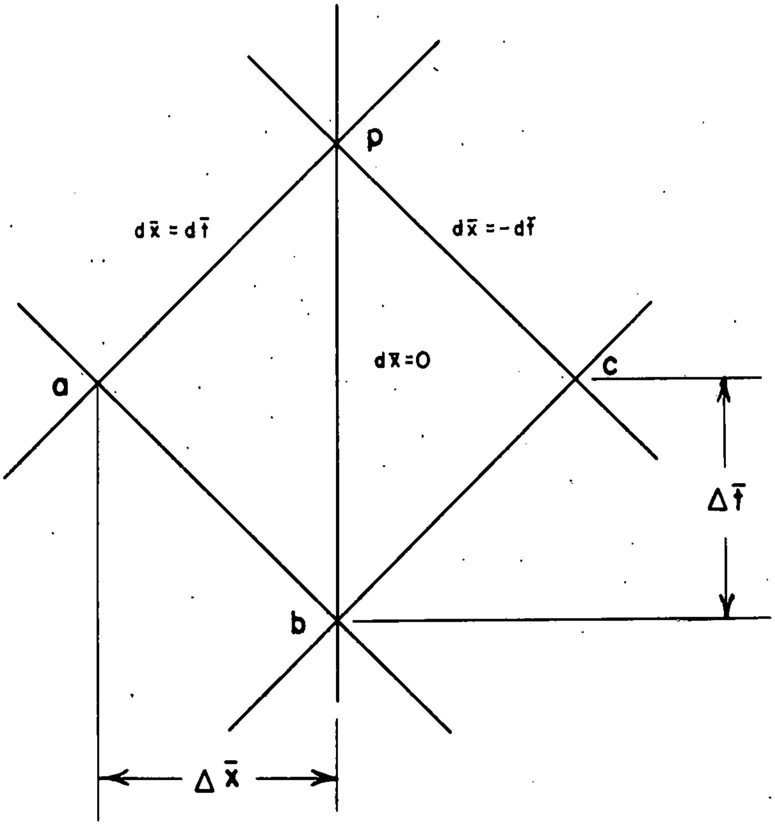

FIG. 24 ELEMENT OF CHARACTERISTIC PLANE

the values of $\bar{\sigma}$, $\bar{\epsilon}$, and $\bar{v}$ are known at points a, b, and c; then the finite difference equations will include only the three unknown quantities at point p. The values of $\bar{\sigma}$ and $\bar{\sigma}_s$ in the right-hand side of Eqs. (53), (54), and (55) are taken as the average values of the quantities between the two points being considered. Eqs. (53), (54), and (55) in finite difference notation become

$$(\bar{\epsilon}_p - \bar{\epsilon}_b) - (\bar{\sigma}_p - \bar{\sigma}_b) = \bar{K} \left[\left(\frac{\bar{\sigma}_p + \bar{\sigma}_b}{2} \right) - \left(\frac{\bar{\sigma}_{sp} + \bar{\sigma}_{sb}}{2} \right) \right] 2 \Delta t = - - - \qquad (56)$$

$$(\bar{\sigma}_p - \bar{\sigma}_a) - (\bar{v}_p - \bar{v}_a) = -\bar{K} \left[\left(\frac{\bar{\sigma}_p + \bar{\sigma}_a}{2} \right) - \left(\frac{\bar{\sigma}_{sp} + \bar{\sigma}_{sa}}{2} \right) \right] \Delta t \quad - - - \qquad (57)$$

$$(\bar{\sigma}_p - \bar{\sigma}_c) + (\bar{v}_p - \bar{v}_c) = -\bar{K} \left[\left(\frac{\bar{\sigma}_p + \bar{\sigma}_c}{2} \right) - \left(\frac{\bar{\sigma}_{sp} + \bar{\sigma}_{sc}}{2} \right) \right] \Delta t \quad - - - \qquad (58)$$

These three equations contain three independent unknowns, $\bar{\epsilon}_p$, $\bar{\sigma}_p$, and $\bar{v}_p$, and one dependent unknown, $\bar{\sigma}_{sp}$, which is a function of $\bar{\epsilon}_p$. The function $\bar{\sigma}_s$ is stored in the computer as a polynomial in $\bar{\epsilon}$. The equations are solved by a successive approximation or iteration process for which a digital computer is best suited. After they are simplified, they become:

$$(\bar{\epsilon}_p^i - \bar{\epsilon}_b) - (\bar{\sigma}_p^i - \bar{\sigma}_b) = \bar{K} \left[(\bar{\sigma}_p^{i-1} - \bar{\sigma}_{sp}^{i-1}) + (\bar{\sigma}_b - \bar{\sigma}_{sb}) \right] \Delta t - - - \qquad (59)$$

along $d\bar{x} = 0$

$$(\bar{\sigma}_p^i - \bar{\sigma}_a) - (\bar{v}_p^i - \bar{v}_a) = -\bar{K} \left[(\bar{\sigma}_p^{i-1} - \bar{\sigma}_{sp}^{i-1}) + (\bar{\sigma}_a - \bar{\sigma}_{sa}) \right] \frac{\Delta t}{2} \qquad (60)$$

along $d\bar{x} = d\bar{t}$

$$(\bar{\sigma}_p^i - \bar{\sigma}_c) - (\bar{v}_p^i - \bar{v}_c) = -\bar{K}\left[(\bar{\sigma}_p^{i-1} - \bar{\sigma}_p^{i-1}) + (\bar{\sigma}_c - \bar{\sigma}_{sc})\right]\frac{\Delta t}{2} \quad - - \quad (61)$$

$$\text{along } d\bar{x} = -d\bar{t}$$

The superscript i represents the i^{th} approximation.

When the three quantities are obtained for **point p**, the computer may transfer to an adjacent point and repeat the process.

In order that the unknowns at all of the points within the $\bar{x}$ - $\bar{t}$ space bounded by the lines $\bar{x} = 0$, $t > \bar{x}$, and $t < 2 - \bar{x}$ in Fig. 23 may be computed; four of the six quantities along the lines $\bar{x} = \bar{t}$ and $\bar{x} = 0$ must be known.

If an impact takes place such that the particle velocity at $\bar{x} = 0$ experiences an instantaneous jump, then a discontinuity will propagate along the line $\bar{x} = \bar{t}$, and the material is assumed to behave elastically at the wave front. That is

$$\sigma_j = -\rho C_o v_j \qquad - - - - - \qquad (62)$$

or

$$\bar{\sigma}_j = -\bar{v}_j \qquad - - - - - \qquad (63)$$

and

$$\bar{\varepsilon}_j = \bar{\sigma}_j \qquad - - - - - \qquad (64)$$

where $\bar{\sigma}_j$, $\bar{\varepsilon}_j$, and $\bar{v}_j$ are the values associated with the discontinuity at the wave front. The negative sign must be used for a front moving from left to right because particle velocities to the right are considered positive and compressive stresses are negative. It must be emphasized that Eqs. (62), (63), and (64) apply only at the wave front and that as the front moves along the bar, Eq. (60) applies. If the magnitude of the velocity step at $\bar{x} = 0$ is known, then Eqs. (60), (63), and (64) are sufficient to determine the stress, strain, and particle velocity all along the characteristic $\bar{x} = \bar{t}$.

If the particle velocity variation at $\bar{x} = 0$ is not a step function, but has a finite rise time, then a fine grid must be chosen so that the time variation of particle velocity can be approximated to a sufficient degree of accuracy by a series of finite steps.

Reflections at the Ends of the Specimen

If a step in stress of magnitude σ_i approaches the end of a copper specimen supported by the steel bar, then any reflection that occurs will be purely an elastic reflection so that

$$\bar{\sigma}_r = \frac{\rho_s C_s - \rho_c C_c}{\rho_s C_s + \rho_c C_c} \bar{\sigma}_i \qquad \text{-----} \qquad (65)$$

where $\bar{\sigma}_r$ is the magnitude of the step propagating back toward the impact end and the subscripts s and c denote steel and copper, respectively. The resultant stress after the reflection is then

$$\bar{\sigma} = \bar{\sigma}_o + \bar{\sigma}_i + \bar{\sigma}_r \qquad \text{-----} \qquad (66)$$

where $\bar{\sigma}_o$ was the stress present at the end of the specimen when the step $\bar{\sigma}_i$ arrived.

A reflected step at the impact end will have the same magnitude as the incident step since the projectile is assumed to be rigid; hence, the resultant stress at the impact end after the reflection is

$$\bar{\sigma} = \bar{\sigma}_o + 2\bar{\sigma}_i \qquad \text{- - - - -} \qquad (67)$$

where $\bar{\sigma}_o$ was the stress present at the impact end just before the step $\bar{\sigma}_i$ arrived.

The governing finite difference equations were solved on the I. B. M. 650 Digital Computer in The University of Texas Computing Center. Some of the results of the computations are shown in Figs. 25 and 26. Fig. 25 is a comparison of the stress-time history at the bar end of the specimen as predicted by the strain-rate theory with that predicted by the nonstrain-rate theory. The strain-rate curve was computed using a value of K equal to 60 x 10^4 per second. It is obvious that the two curves do not agree in either shape or magnitude. One reason for the disagreement is the fact that a step velocity is assumed at the impact end and for the strain-rate theory, a large percentage of the step arrives at the bar end.

The strain-time histories are shown in Fig. 26. These curves would be in very good agreement if it were not for the sudden jump at the beginning of the strain-rate curve.

Obviously, the strain-rate curves can be changed by varying the flow constant K and by varying the particle velocity-time variation at the impact end. The effects of these variables will be shown in a later section of this report.

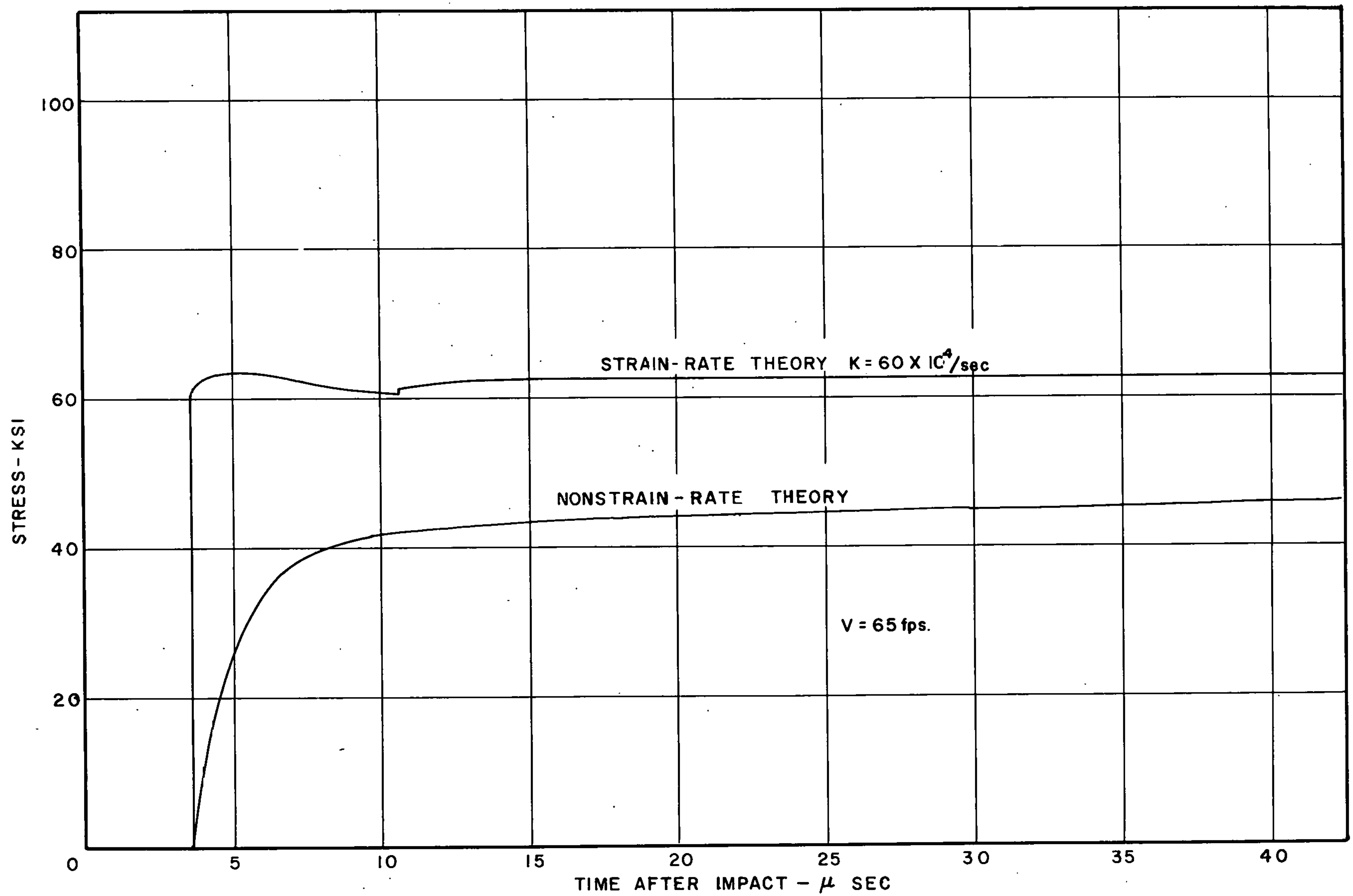

FIG. 25 COMPARISON OF STRESSES FROM STRAIN-RATE AND NONSTRAIN-RATE THEORIES FOR 1/2 in. COPPER SPECIMEN

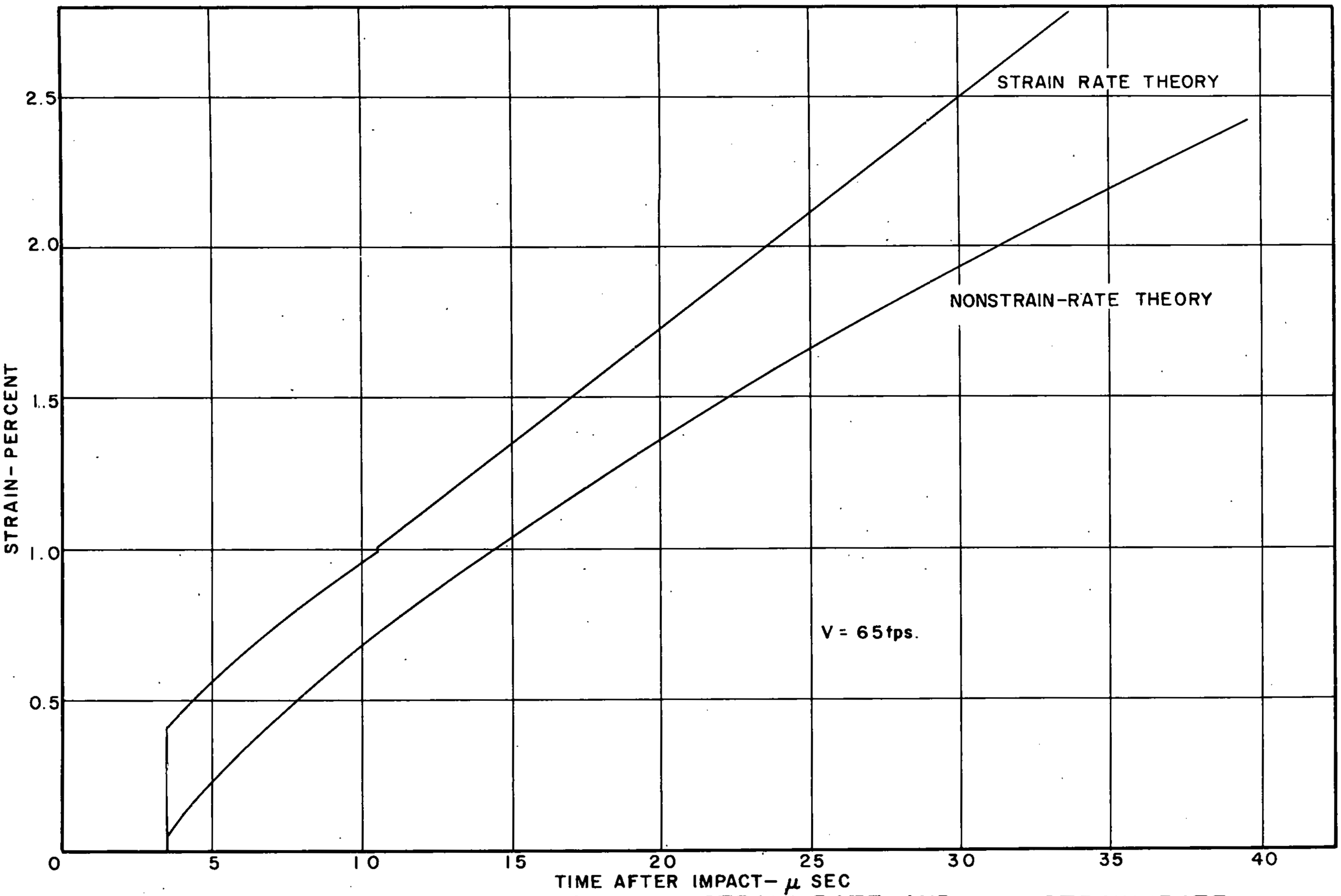

FIG. 26 COMPARISON OF STRAINS FROM STRAIN-RATE AND NONSTRAIN-RATE THEORIES FOR ½ in. COPPER SPECIMEN

EXPERIMENTAL TECHNIQUE FOR STRAIN MEASUREMENT

In general, the experimental problem is that of mounting a copper or lead specimen on a steel pressure bar and subjecting it to an impact of some known velocity. A schematic diagram of the setup is shown in Fig. 27.

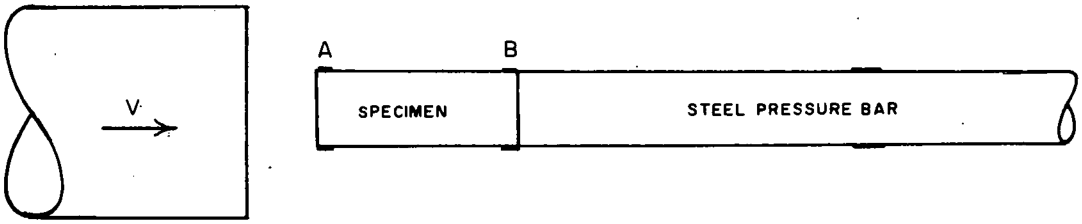

FIG. 27, SCHEMATIC OF EXPERIMENTAL SETUP

The measurements to be made include the impact velocity, the strain-time variation at sections A and B, and the stress-time variation at section B which is the interface between the specimen and pressure bar.

Description of Equipment

The equipment used in the experimental work includes a 1.5-in.-bore air gun to fire the projectile against the specimens, a 0.5-in steel pressure bar, a mounting system to hold the specimen in true alignment with respect to the projectile, a photoelectric system to measure the impact velocity, and a battery of oscilloscopes and cameras to record the measured quantities.

Air gun. The 1.5-in. air gun is shown in Fig. 28. Dry nitrogen is actually used instead of air to operate the gun since it can be obtained more conveniently than the compressed air. The projectiles are 6, 12, and 18-in. long and weigh 3, 6, and 9 lb. respectively, and are made of SAE 1060 steel. The cylindrical surfaces were case hardened to Rockwell C-60 to a depth of about 1/8-in. and the end surfaces were flame hardened. All the surfaces were ground and polished. The 48-in. gun barrel has a wall thickness of 0.625-in. and is made of AISI 4140 steel heat treated to a hardness of Rockwell C-58. The bore is ground and honed to a diameter of 1.499-in. with tolerances of plus 0.001, minus 0.000-in. in the last 12 in. and plus 0.004-in. minus 0.000-in. throughout the rest of the barrel. The projectile diameter is 1.4989-in. plus 0.0000-in. minus 0.0004-inches. The projectile and barrel are lubricated with a very light household oil.

The extreme precision is necessary so that absolutely no lateral motion of the projectile is allowed that will produce an oblique impact.

The principle of operation of this gun is essentially the same as that for the MK2, MOD O gun described by Benedick.[8]

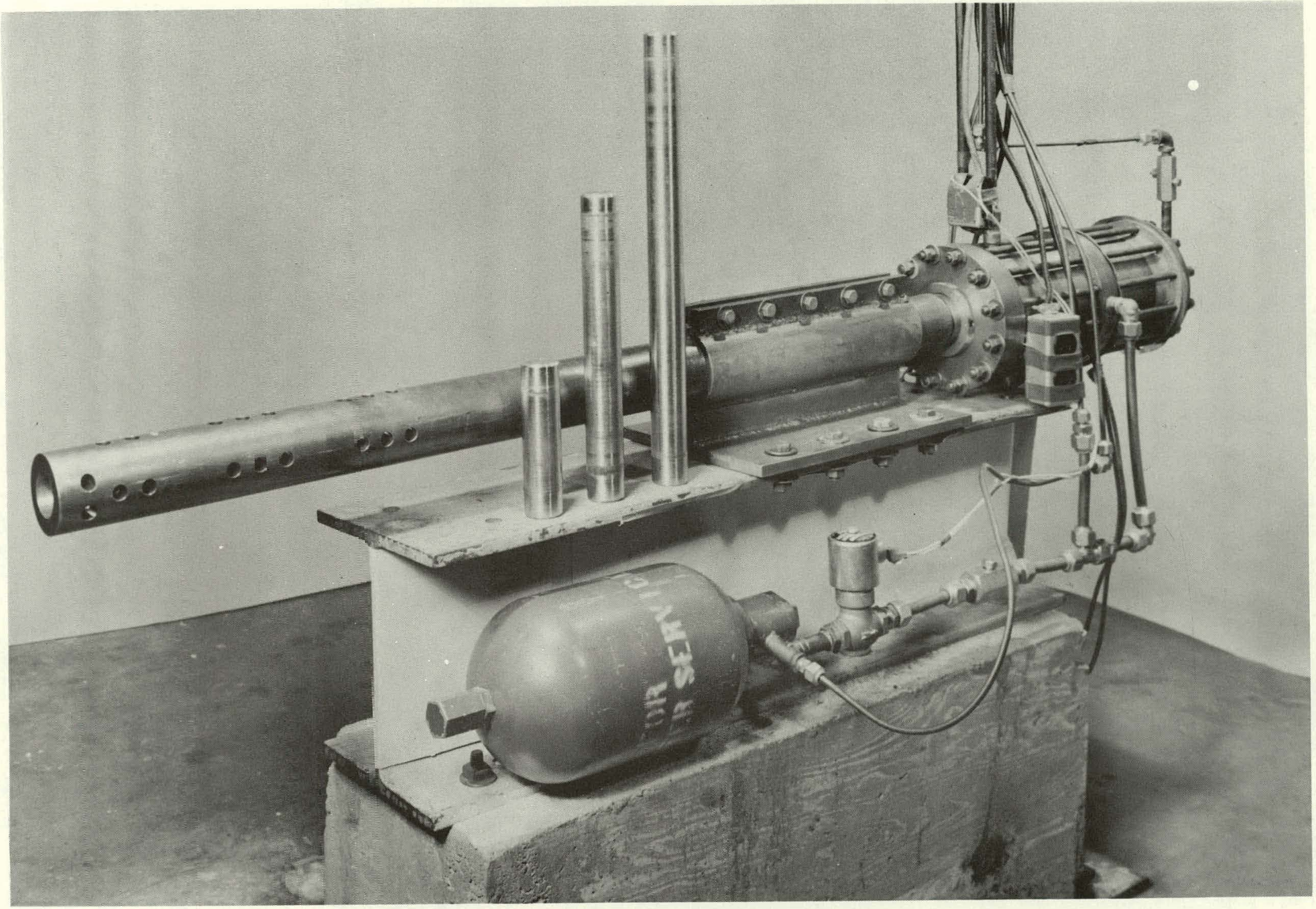

FIG. 28 1.5" AIRGUN WITH PROJECTILES

Pressure bar and alignment system. The pressure bar is a 10-ft piece of 0.5-in. case hardened, SAE 1060 steel with one end ground and polished to obtain as flat a seat as possible for the specimens. The bar is held inside a tube of 1.0-in. inside diameter and 1.5-in. outside diameter by four teflon rings spaced throughout its length. The tube is mounted in two teflon bushings held in a pair of two-way Universal vises. The vises are used to vary the alignment of the pressure bar and specimen with respect to the projectile so that as near a plane impact as possible is obtained. The pressure bar and mounting system is shown in Fig. 29. The tube, which is allowed to slide in the teflon bushings, dissipates the excess kinetic energy by crushing a pad of paper honeycomb placed between the back end of the tube and a steel and concrete battering block. Thus, after the required measurements are recorded, the projectile strikes the tube which protects the pressure bar from damage.

Two Type A-7, 1/4-in. strain gages are mounted 2.5-in. from the impact end of the pressure bar. The gages are wired into a Wheatstone bridge so that the symmetric strains are recorded and the bending strains are cancelled. The system is used to measure the stress exerted by the specimen on the bar.

Photoelectric system. The impact velocity is calculated by measuring the time it takes the projectile to cut two narrow beams of collimated light positioned a known distance apart. A photograph of the collimating light source and the receiving photomultiplier

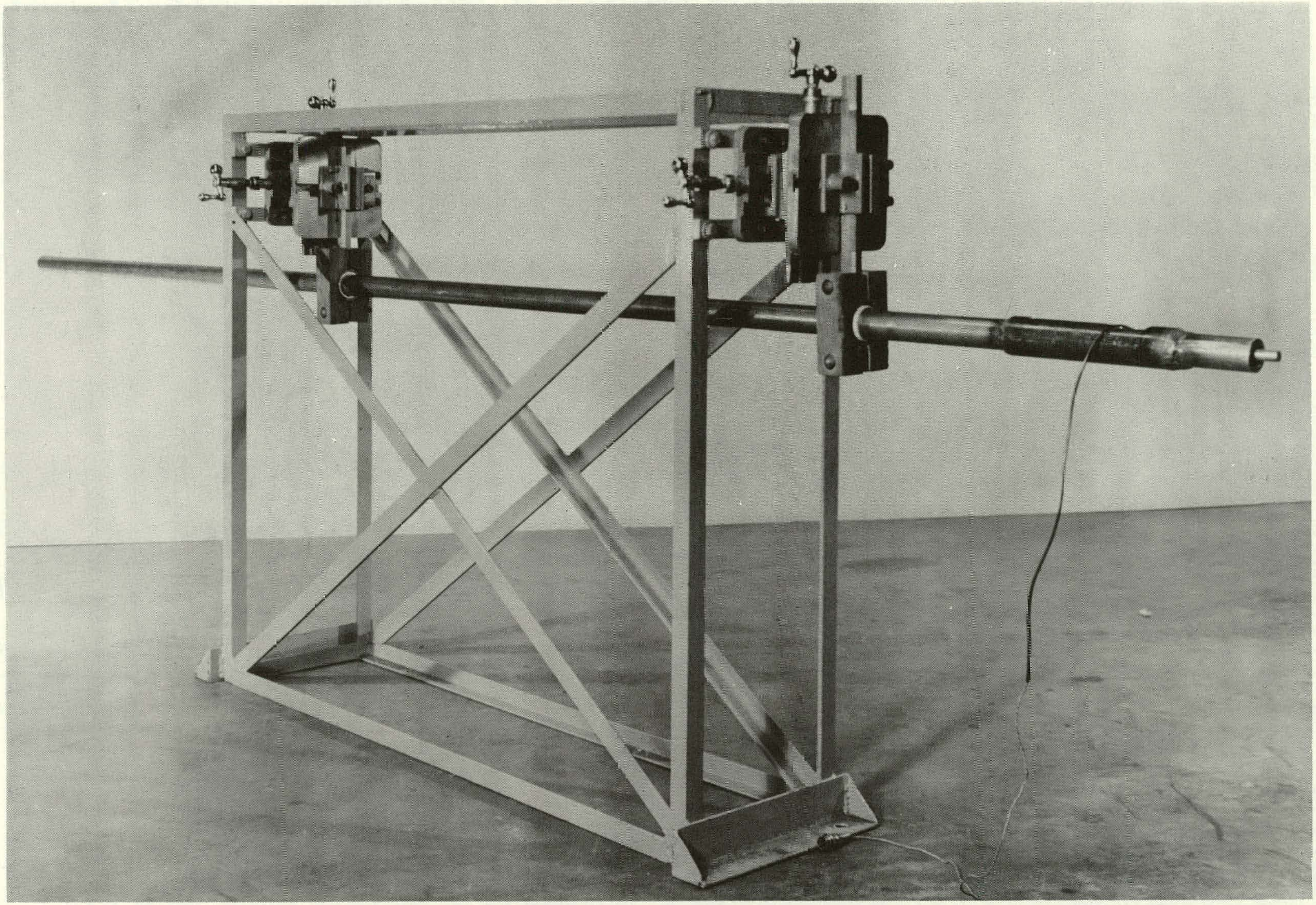

FIG. 29 ONE-HALF INCH PRESSURE BAR IN TUBE SUPPORT AND MOUNT

with power supply is shown in Fig. 30. A detailed description of the entire photoelectric system may be found in Ref. (8).

Instrumentation. The quantities to be recorded are four strain measurements, one on each side of the specimen at sections A and B in Fig. 27, a stress as indicated by the gages on the pressure bar, and the output of the photomultiplier which is an indication of the impact velocity. This requires a minimum of six oscilloscopes. However, in order to obtain strain records at various sensitivities and sweep rates, ten traces are needed. The available scopes included five Tektronix Model 545's, three Model 535's, and one Model 551. The Model 551 has a dual-trace beam which results in a total of ten traces available for recording. Each scope is equipped with a DuMont Oscilloscope Recording Camera with Polaroid back.

Preparation

The two materials used were commercially pure unannealed copper and tellurium lead. All of the specimens were 0.5-in. in diameter. The copper specimens were 0.5, 1.0, and 2.0-in. long. The lead specimens were all 1.0-in. long. All the specimens were machined from 0.5-in. diameter rods.

The specimens were cut to length and the end surfaces faced in a lathe. The end surfaces were then hand lapped by rubbing them on No. 400 Emory cloth spread over a hardened, ground, flat surface made for that purpose. The end surfaces were lapped until all tool

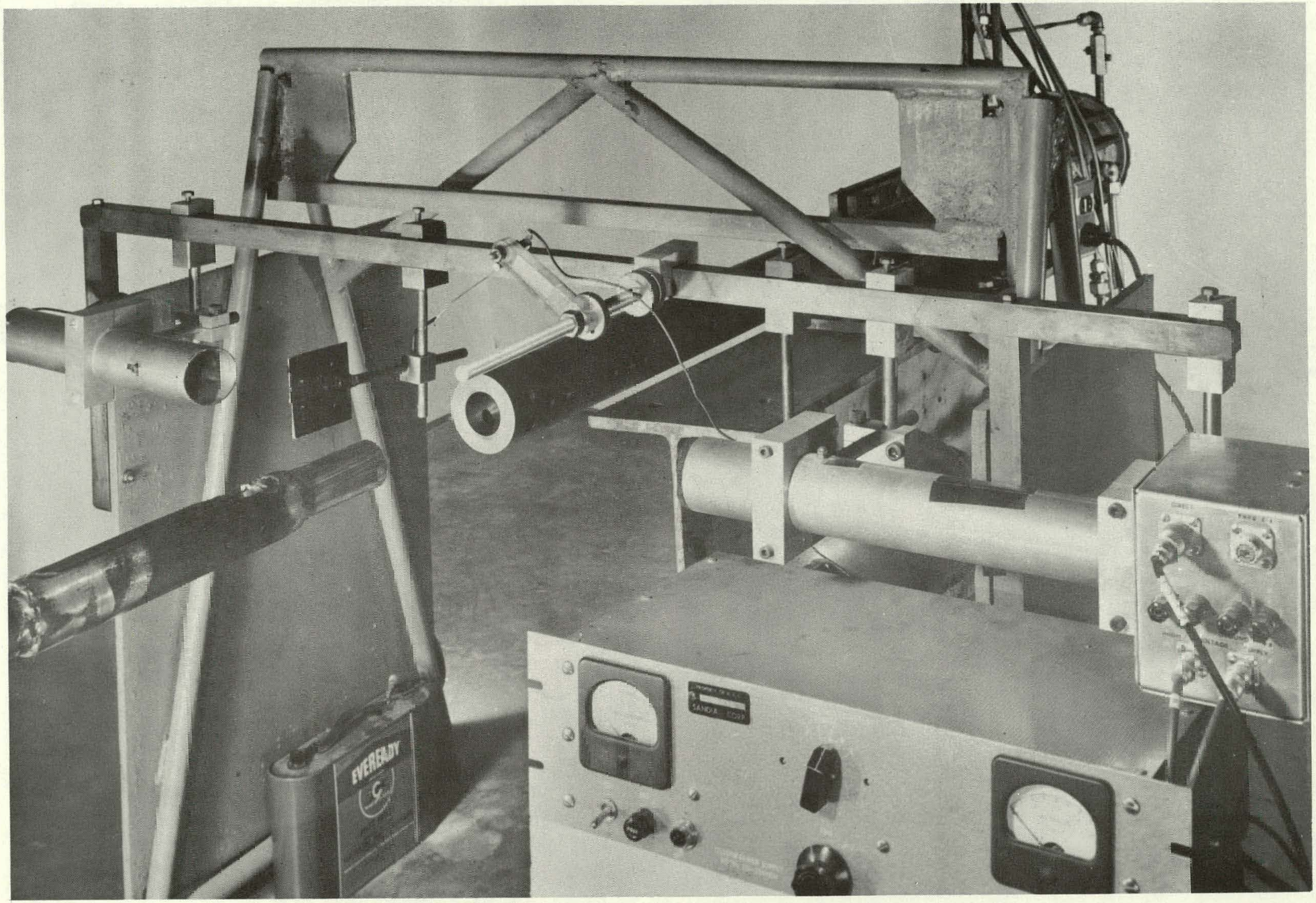

FIG. 30 PHOTOELECTRIC SYSTEM FOR MEASURING IMPACT VELOCITY

marks were gone and the ends were flat across. The lapping was continued until the two end surfaces were as near parallel as could be measured with a micrometer capable of measuring to 0.0001-inches. The end surfaces of the copper were within 0.0002 radian of being parallel. The lead specimens were more difficult to lap and the finishing touches were made by lapping them on a sheet of paper spread over the flat surface. The paper cut the lead quite satisfactorily for the purpose. The very tedious preparation procedure was necessary to insure as near a plane impact as possible.

Mounting the strain gages. The cylindrical surfaces were prepared for the gages by blasting them with a very fine sand. The specimens were then cleaned with acetone.

The gages used on the 1.0 and 2.0-in. specimens were Tatnall Type C9-111 which are 1/16-in. long. Type C9-1x1-32 gages which have a length of 1/32-in. were used on the 0.5-in. specimens. The gages are etched foil mounted on epoxy backing. They were bonded to the specimens with Armstrong Epoxy Resin Type C-2 with Activator E. The use of Type C-2 with the foil gages enabled strains as high as 3 per cent to be measured. The resin was heat cured at 230F for one and one-half hours. The curing also served to stress relieve the specimens. On every specimen, the gages were mounted as near the end surfaces as possible. A group of specimens before the gages were mounted is shown in Fig. 31.

Procedure. After the specimens were prepared and the gages and lead wires were connected, a shot was ready to be made. The

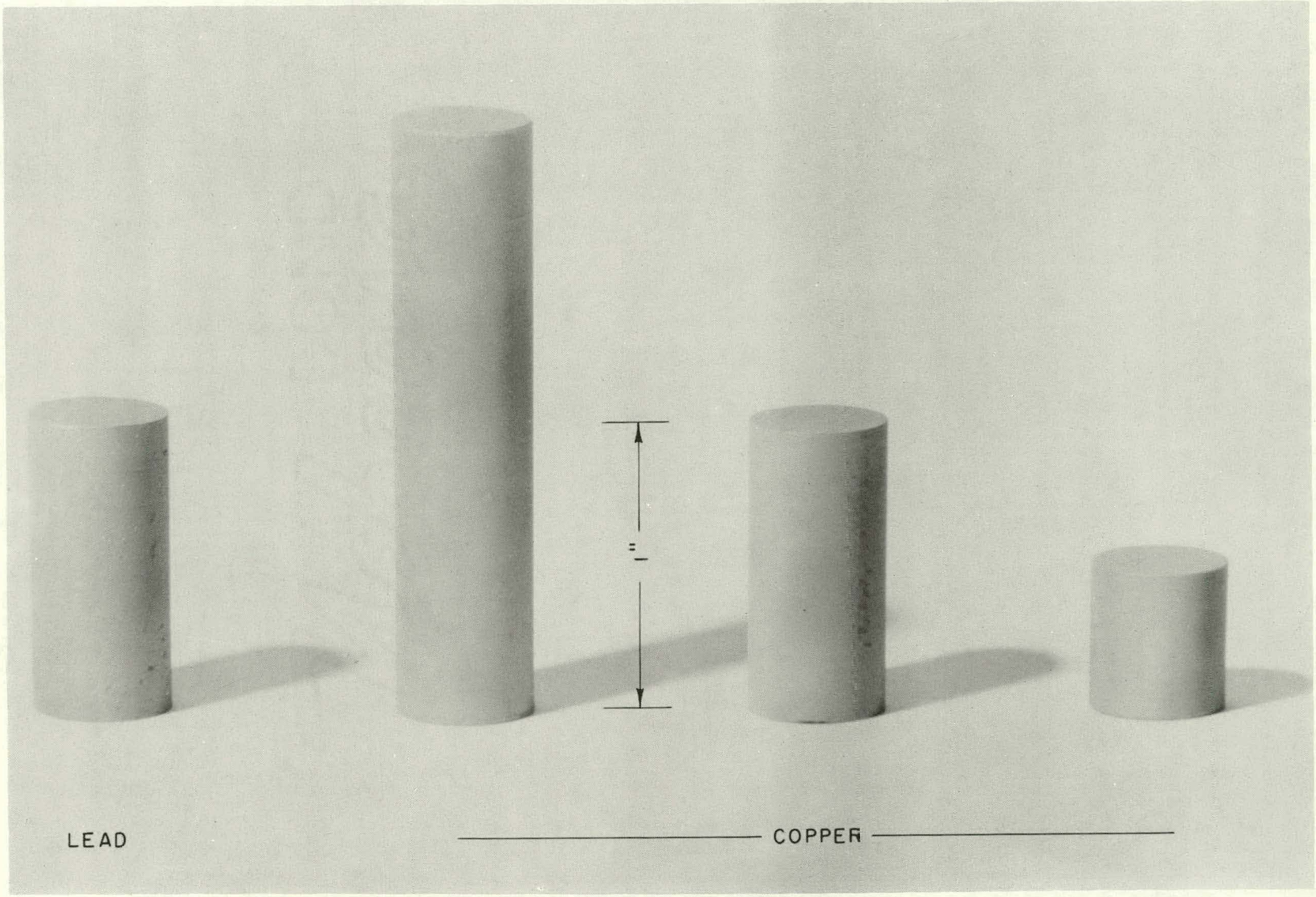

FIG. 31 LEAD AND COPPER SPECIMENS

particular specimen to be used was mounted on the end of the pressure bar using a very thin film of Duco cement. The specimen was held firmly in place until the glue dried to insure as intimate a contact as possible between the specimen and bar.

The four strain gages on the specimen were connected to four Wheatstone bridges so that the strains could be recorded individually. The bridge outputs were then connected to the various oscilloscopes.

The impact face of the specimen was made to fit flat against the surface of the projectile to insure a plane impact. Adjustments were made with the two-way Universal vises and the planeness was checked carefully by shining a light between the projectile and specimen. After proper alignment was assured, the projectile was pushed to the rear of the barrel in firing position.

The scopes were triggered by the projectile coming in contact with a piece of piano wire protruding in front of the impact face of the specimen as shown in Fig. 32. The triggering wire is attached through a 45-volt battery to the external triggering circuits in the scopes. Fig. 32 also shows the specimen in firing position.

Calibration must be made just before firing since the gages and specimens are destroyed by the impact. This also helps to minimize the effects of amplifier drift and other instability factors. The calibrations are made by shunting the active leg of the Wheatstone bridge with a precision resistor which results in an apparent change in resistance of the strain gage, thus indicating an apparent strain. The shunt resistor is connected and disconnected rapidly by a mechanical

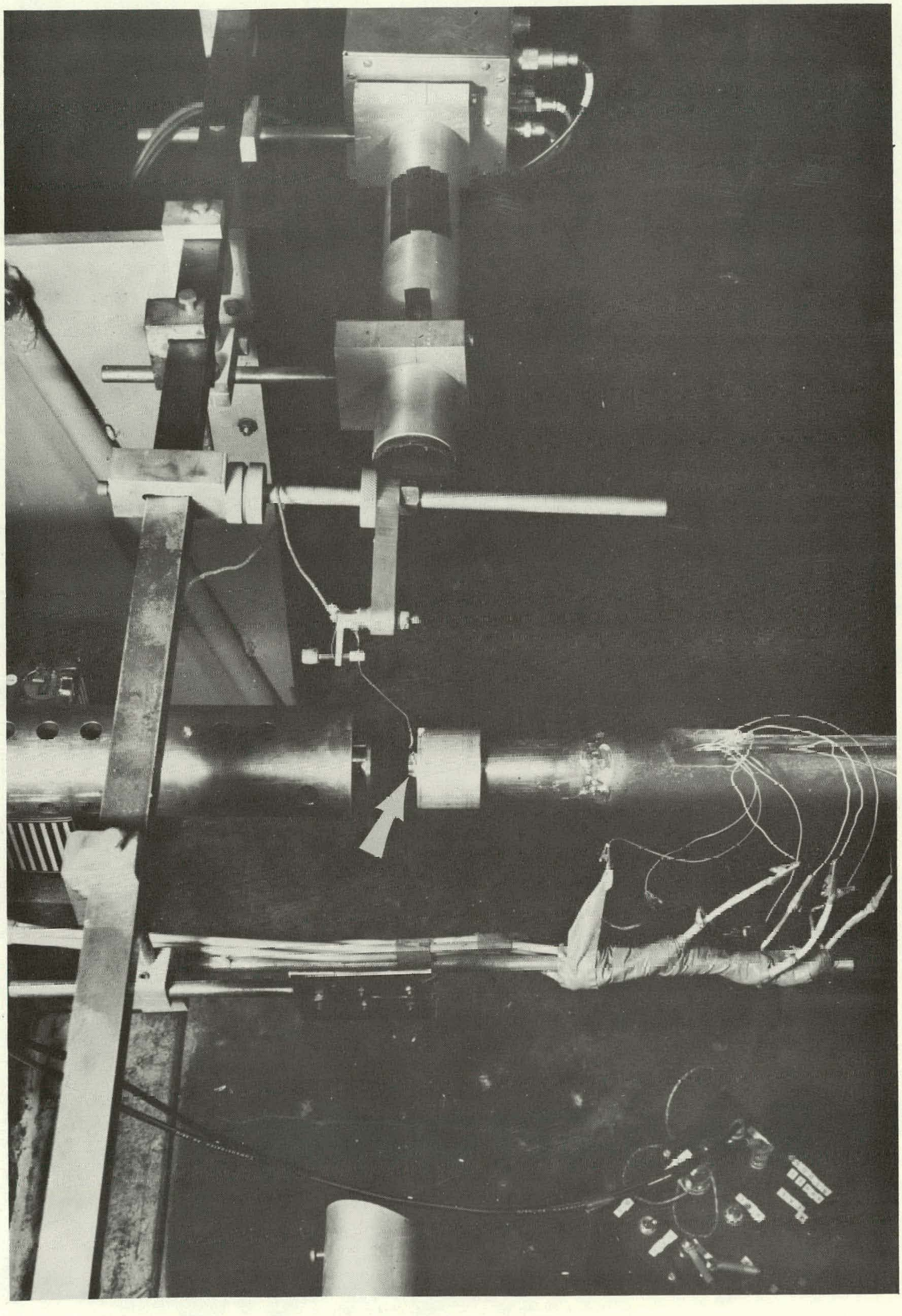

FIG. 32 SPECIMEN AND TRIGGER IN FIRING POSITION

chopper which results in the appearance of two dots or pips on the oscilloscope screen. The distance between the two pips represents a known strain determined by the value of the shunt resistor. The scopes recording the output of the four gages on the specimen and the strain gages on the pressure bar are all calibrated in the above manner. Of course, the Young's modulus of the steel pressure bar is used to convert strain to the stress in the pressure bar.

It is not necessary to calibrate the photoelectric system since the magnitude of its output is unimportant. The only measured quantities are the distance between the light slits passing in front of the specimen and the time between successive steps on the photomultiplier output signal. Oscilloscope grids, calibration pips, and records are all superimposed on the same photograph.

With the calibrations made, the gun is pressurized with dry nitrogen to the pressure necessary to give the required impact velocity.

When all preparations for firing have been completed the camera shutters are opened and the gun is fired.

An example of the photographs obtained are displayed in Fig. 33. The records shown are for one of the 10 fps shots on lead.

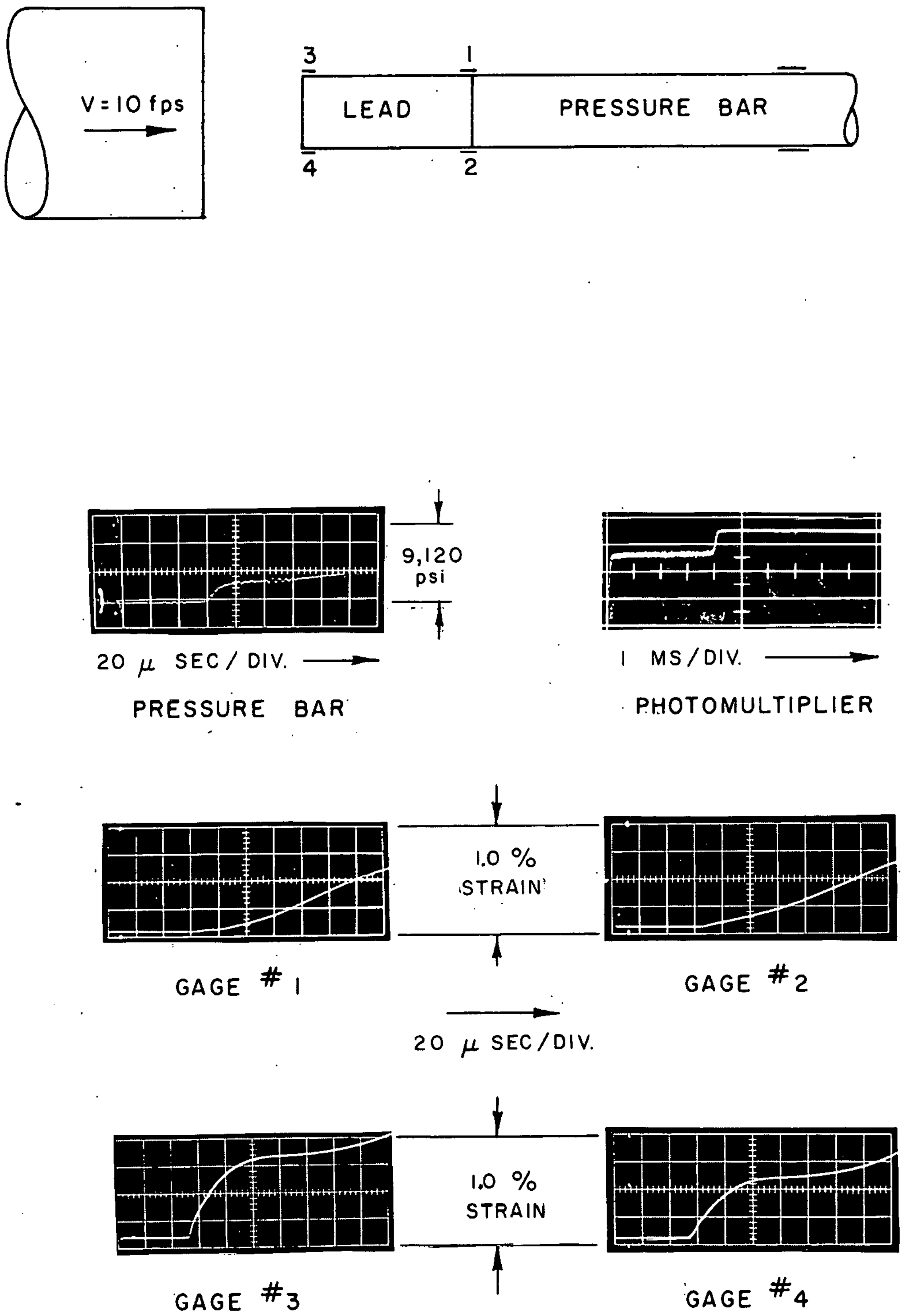

FIG.33 ORIGINAL RECORDS OF 10 fps SHOT ON LEAD

EXPERIMENTAL RESULTS

Copper

The experimental program for copper was conducted with specimen length and impact velocity as the variable parameters. Lengths of 1/2, 1, and 2-inches and impact velocities of 33, 65, and 110 fps were included in the program. The diameter, it will be recalled, of all specimens was 1/2-inch. All three lengths were impacted at 65 fps and all three velocities were used on 1-in. specimens. The measured results include stress at the bar end as measured by the pressure bar and strain measured on the specimen by gages at the impact end and the bar end as previously indicated.

Stresses and strains recorded for two 1/2-in. specimens impacted at 65 fps are shown in Fig. 34. The maximum stress indicated for these impacts is 55,000 psi whereas the maximum stress on the static stress-strain curve shown in Fig. 8 is only 45,000 psi. This increase is consistent with results obtained by other investigators.[1, 2, 10]

The strain curves which begin at $t = 0$ were recorded from the gages at the impact end. The strains at the bar end begin at the time required for the elastic wave to travel the length of the specimen. The strains measured at diametrically opposite positions do not always begin at the same instant. This is probably because the impacts cannot be exactly plane, which results in a stress-wave front

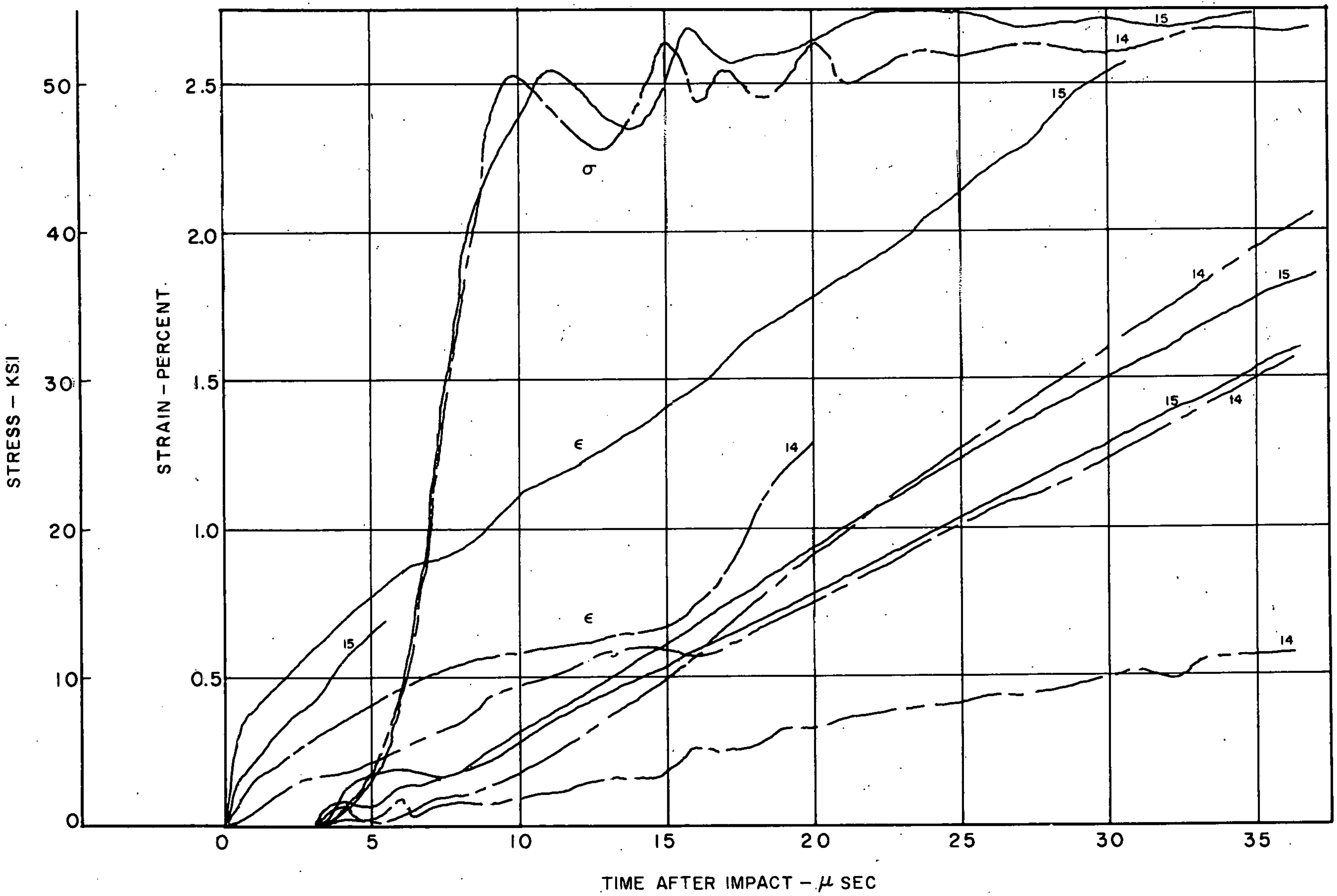

FIG. 34. RESULTS OF 65 fps SHOT ON 1/2 in. COPPER

that is not perpendicular to the specimen axis. The fact that there are at times wide discrepancies in strains measured at the same end of the specimen indicates also that the wave is not uniform even if it is plane. The strains at the bar end of Shot No. 15 agree reasonably well, while those of Shot No. 14 do not. Note that the strains at both the impact and bar ends have approximately the same slope and continue to increase in a straight line.

Fig. 35 shows the results for the 65-fps impacts on 1-in. specimens. The stress record for Shot No. 5 was not obtained. The maximum stress obtained for the 1-in. specimen was approximately 45,000 psi. Previous investigators[10*] have shown the maximum stress for these conditions to be approximately 51,000 psi. The strain at the impact end for both shots appears to have reached a maximum in about 15 μsec instead of continuing to increase as with the 1/2-in. specimen. The two strain records at the impact end for Shot No. 5 were identical until one of the signals was lost, probably because of a broken gage or lead wire. Because of this, it is surprising that the strains at the bar end are so different. For Shot No. 6, strains at the impact end show a large discrepancy, but those at the bar end are in very good agreement. This indicates that there is little correlation between the uniformity of the strain wave at the impact and the bar ends of the specimen.

---

[*] Unpublished results obtained in Structural Mechanics Research Laboratory also indicate the maximum stress for this condition to be about 50,000 psi.

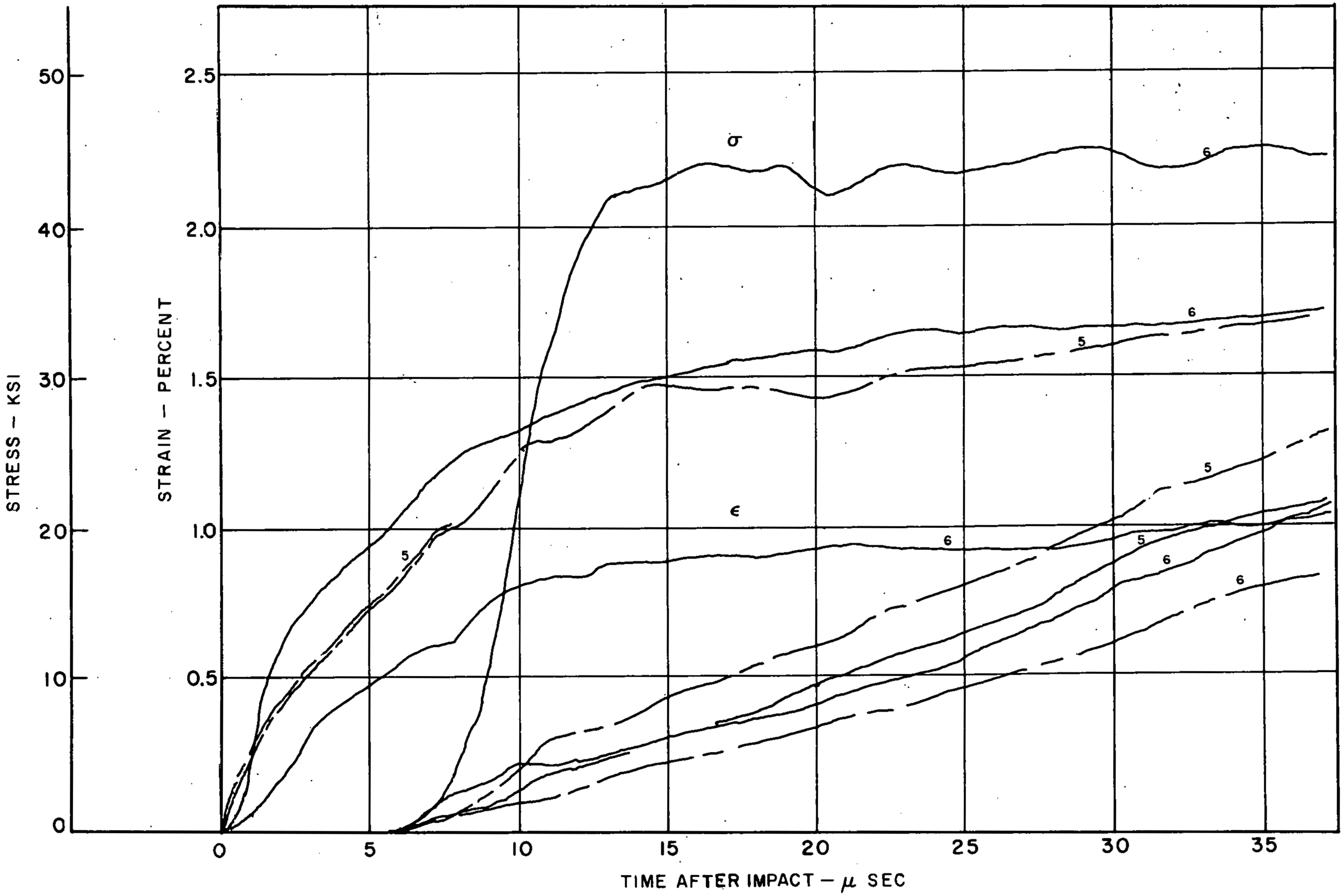

FIG. 35 RESULTS OF 65 fps SHOT ON 1 in. COPPER

Fig. 36 presents the results for the 65-fps shot on the 2-in. specimens. The maximum stresses are again approximately 45,000 psi. The strains at the impact end are very similar to those measured on the 1-in. specimens. This is to be expected, since the material at the impact end must react as if the specimen is infinitely long, at least until a reflection has had time to travel from the bar end back to the impact end.

The strains measured at the bar end of the 2-in. specimens are much lower than those measured on the 1-in. and 1/2-in. specimens. This is not surprising since the strain wave has had time and distance in which to become distorted and flattened.

The results of the 33-fps shot on the 1-in. specimens are shown in Fig. 37. The maximum stress obtained is approximately the same as that shown on the static stress-strain curve. The strains measured at the impact and bar ends of the specimens were approximately the same although they differ considerably for the two shots.

As shown in Fig. 38, the 110-fps impact on the 1-in. specimens produced a maximum stress of from 48,000 to 50,000 psi which is less than that measured on the 1/2-in. specimens impacted at 65 fps. The stress was lower even though the impact velocity was higher probably because the 1-in. specimens allowed the stress time and distance in which to spread out over the specimen length, thus reducing its amplitude.

The strains measured on the 1-in. specimens impacted at 110 fps are also shown in Fig. 38. The strains at the impact end increased

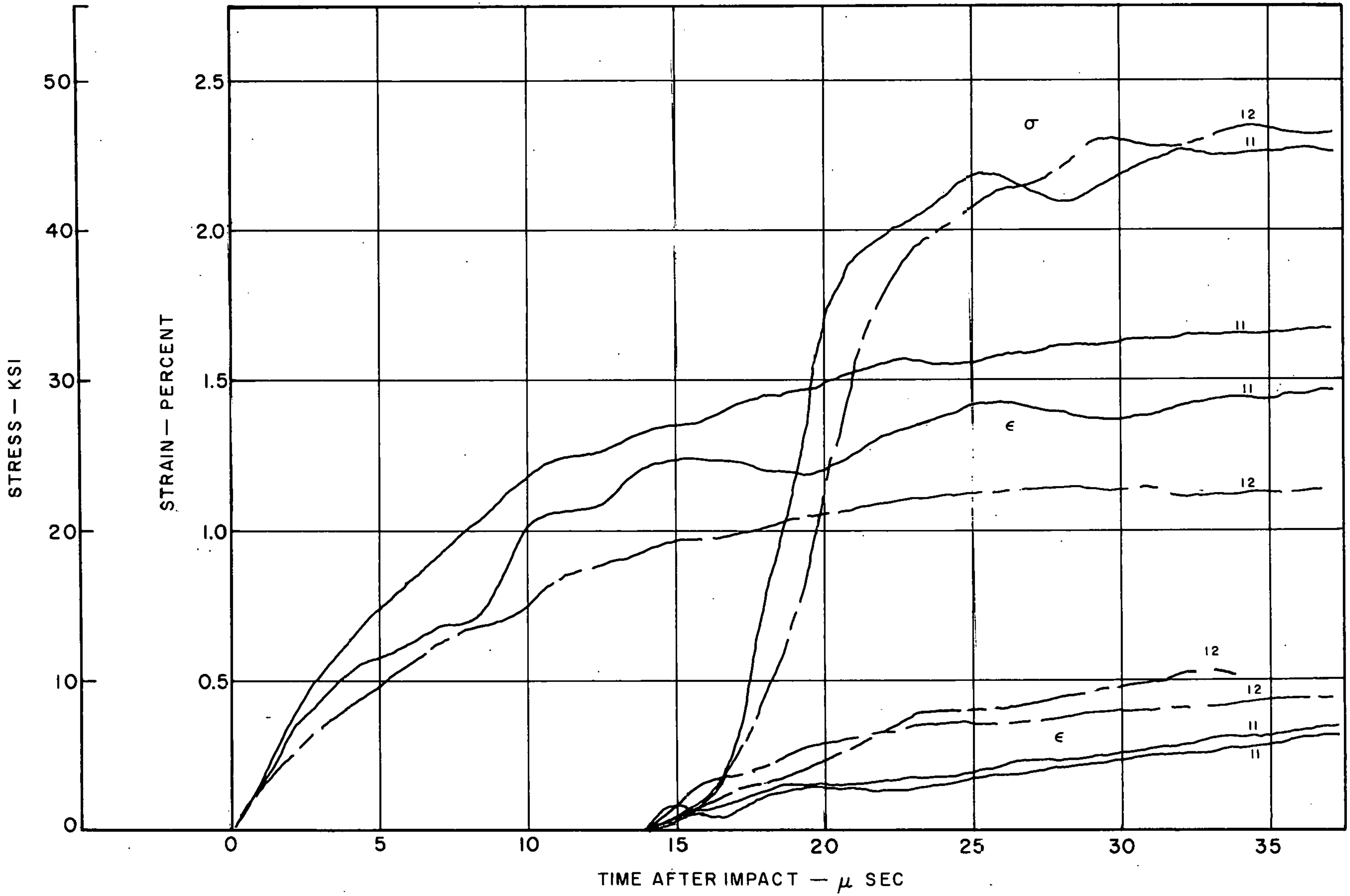

FIG. 36, RESULTS OF 65 fps SHOT ON 2 in. COPPER

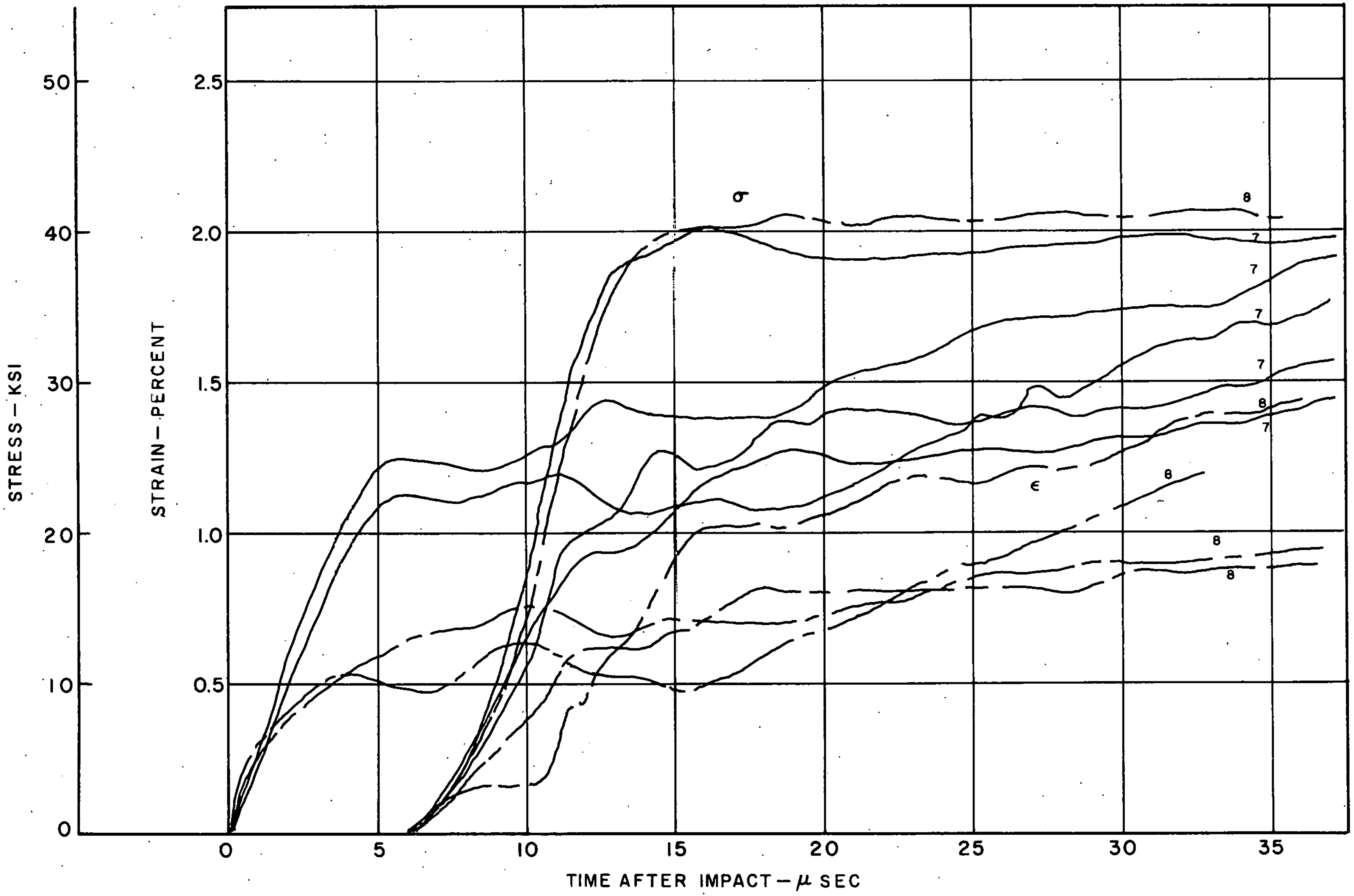

FIG. 37. RESULTS OF 33 fps SHOT ON 1 in. COPPER

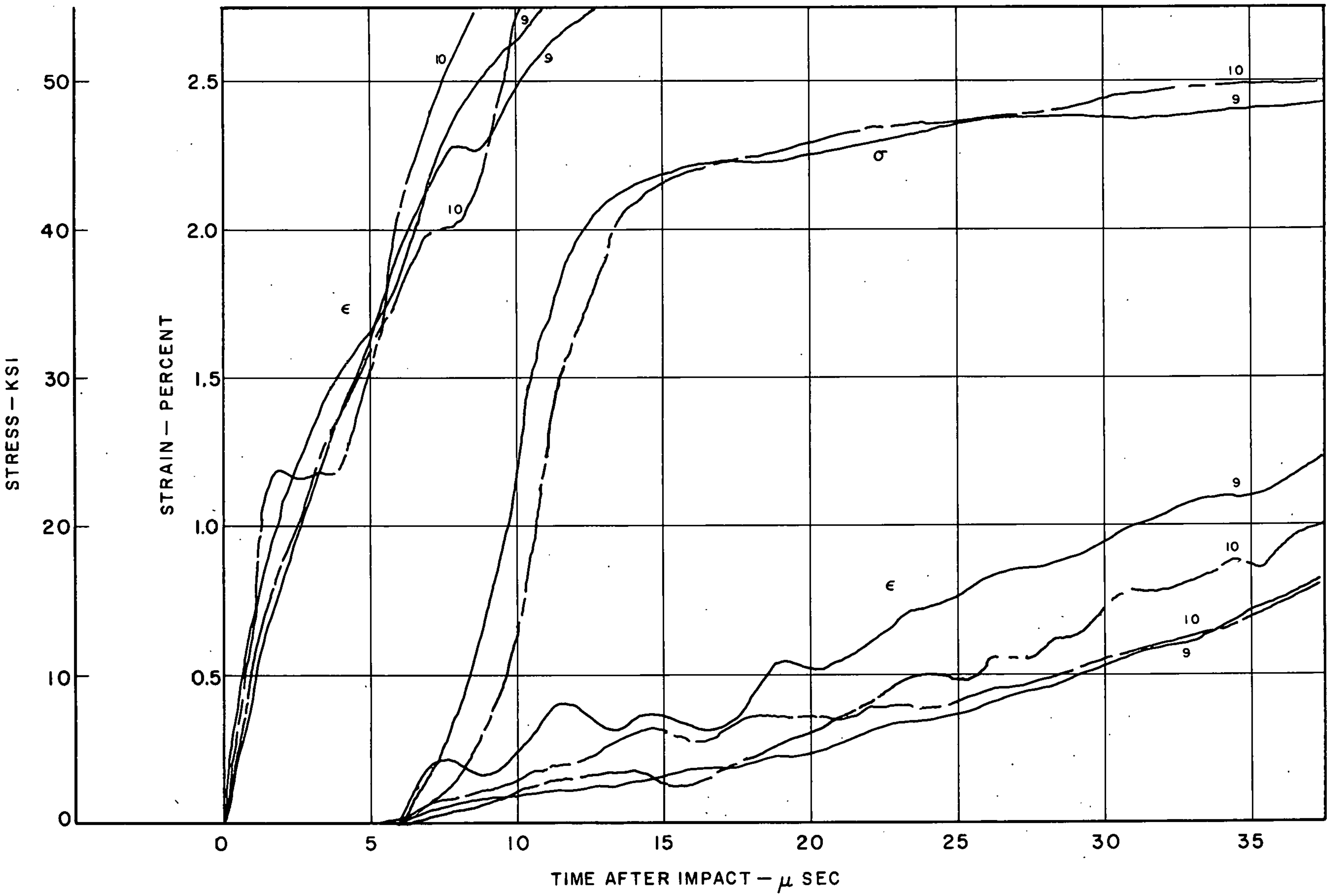

FIG. 38, RESULTS OF 110 fps SHOT ON 1 in. COPPER very rapidly to above 3 per cent strain in approximately 10 μsec. Although this is much larger than the strains measured on any of the other specimens, the strains at the bar end are practically the same as those measured on the 1-in. specimens at 65 fps. An explanation for this will be offered later when the experimental results are compared to the results predicted by the nonstrain-rate theory.

Lead

The shots on lead were made on 1-in. specimens at an impact velocity of 10 fps. The results are shown in Fig. 39. On one of the stress records, oscillations appear that have been recorded previously in numerous tests on lead. It is not believed that the oscillations are caused by the instrumentation, but that they are due to successive slipping of the slip planes in the lead and possibly grain boundary interference.[11] There is no indication of these oscillations on the strain records of Fig. 39. The strains recorded at the impact end for the two shots showed wide scatter while those at the bar end were very nearly equal.

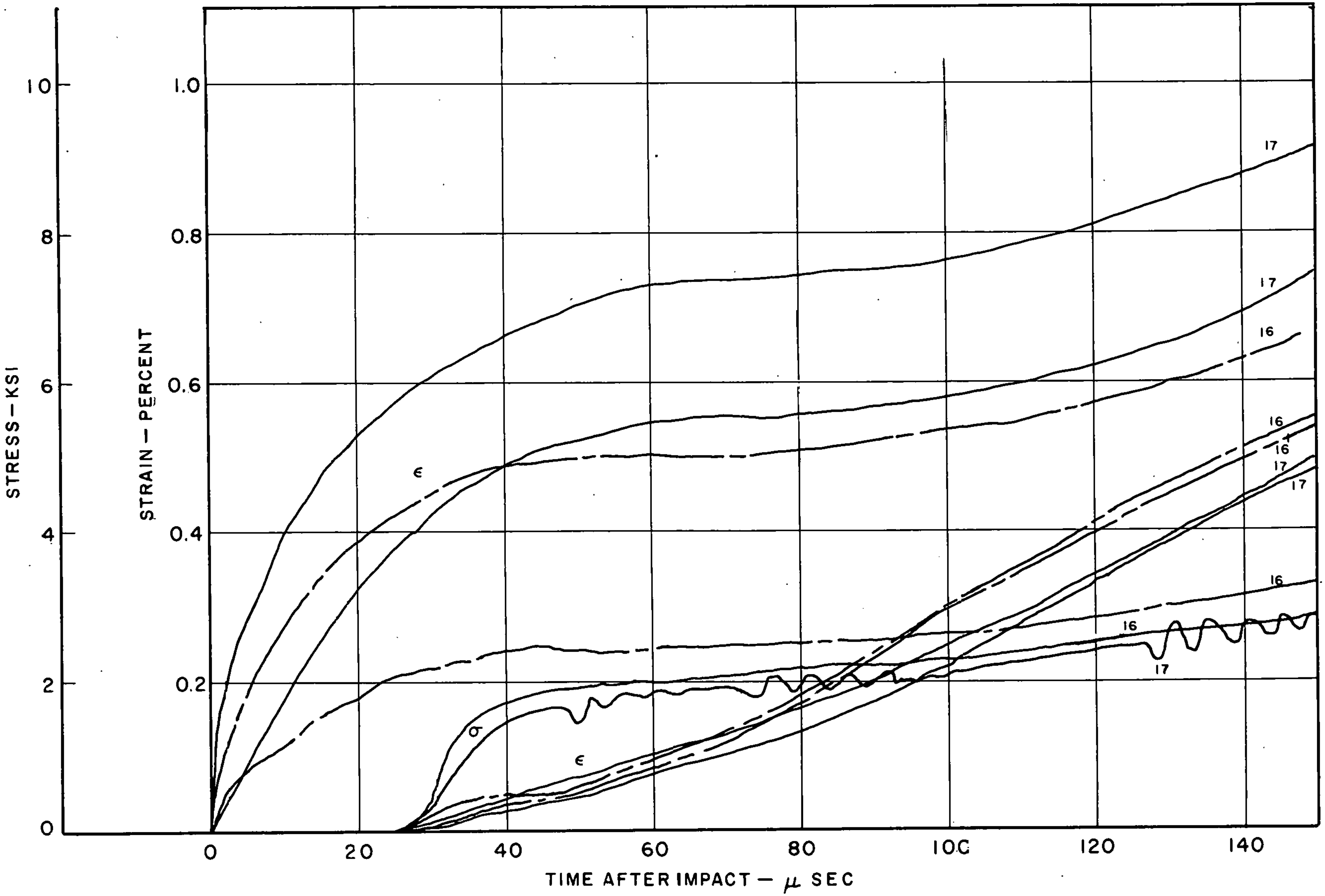

FIG. 39, RESULTS OF 10 fps SHOT ON 1 in. LEAD

COMPARISON OF EXPERIMENTAL WITH THEORETICAL RESULTS

In the comparisons presented in this section, each of the curves representing experimental results is an average of all the original curves obtained for a particular test condition. The curves representing the nonstrain-rate theory were obtained from the diagrams of state discussed previously. The curves representing the strain-rate theory where plotted directly from the digital computer data.

Comparison of Experiment with Nonstrain-Rate Theory

Copper. The stress-time records as measured by the pressure bar are compared with those predicted by the elementary theory in Figs. 40 through 45. In each of these figures, there seems to be a lag between the theoretical and the experimental curves. The initial portions of the theoretical curves rise much faster than the experimental curves. Undoubtedly, this is due partly to the assumption in the theory that the stress wave begins at the impact end as a step which has zero rise time. If the initial wave were assumed to have a rise time of three or four μsec, then the first portions of the theoretical stress-time curves would probably come nearer agreeing with the measured values. The disagreement is also partly due to the assumption that the projectile is rigid instead of elastic.

In every case, the maximum stress measured is from 10 to 20 per cent above the theoretical curve with the exception of the

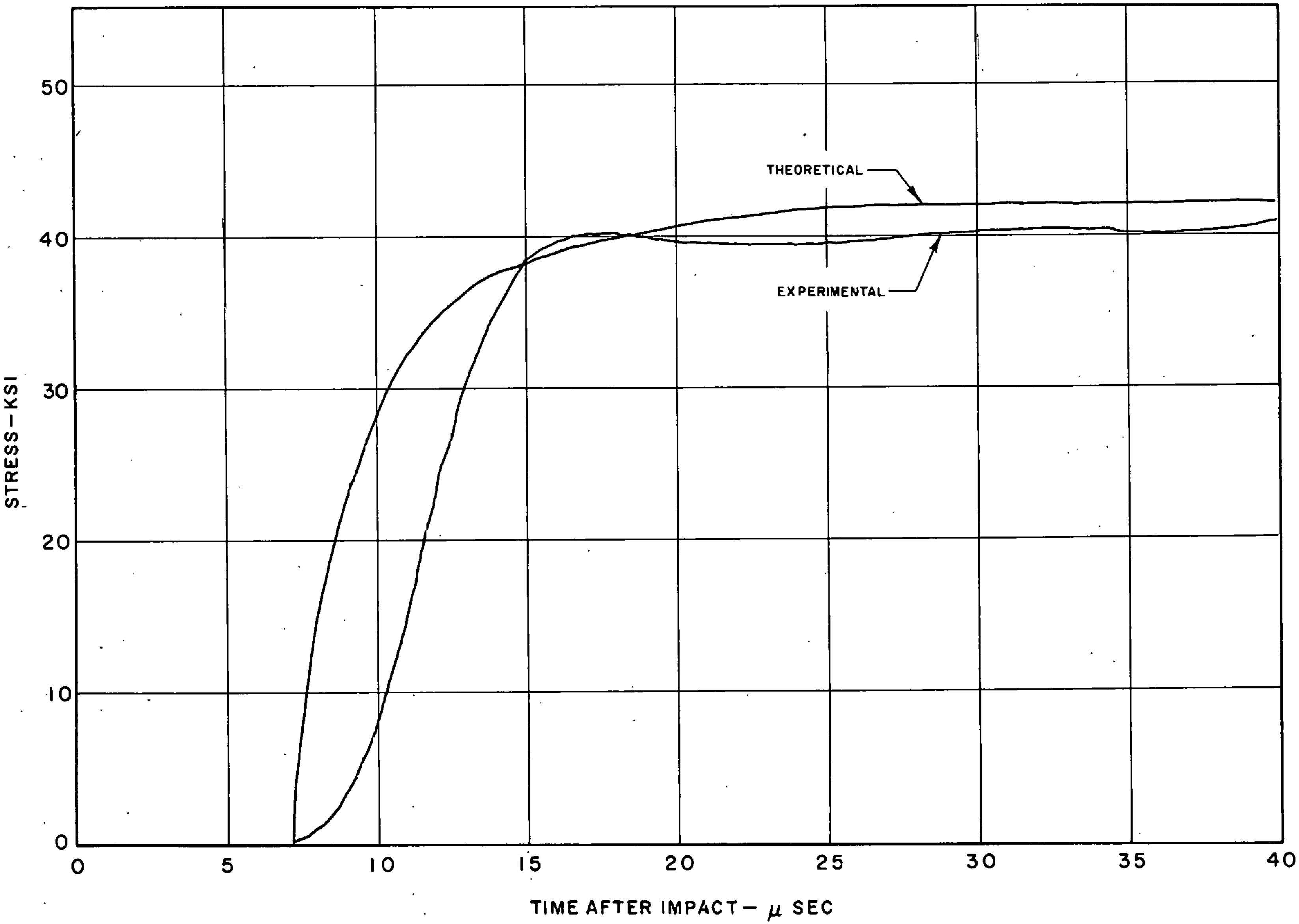

FIG. 40, COMPARISON OF THEORETICAL WITH MEASURED STRESS FOR 33 fps SHOT ON 1 in. COPPER; NONSTRAIN-RATE THEORY

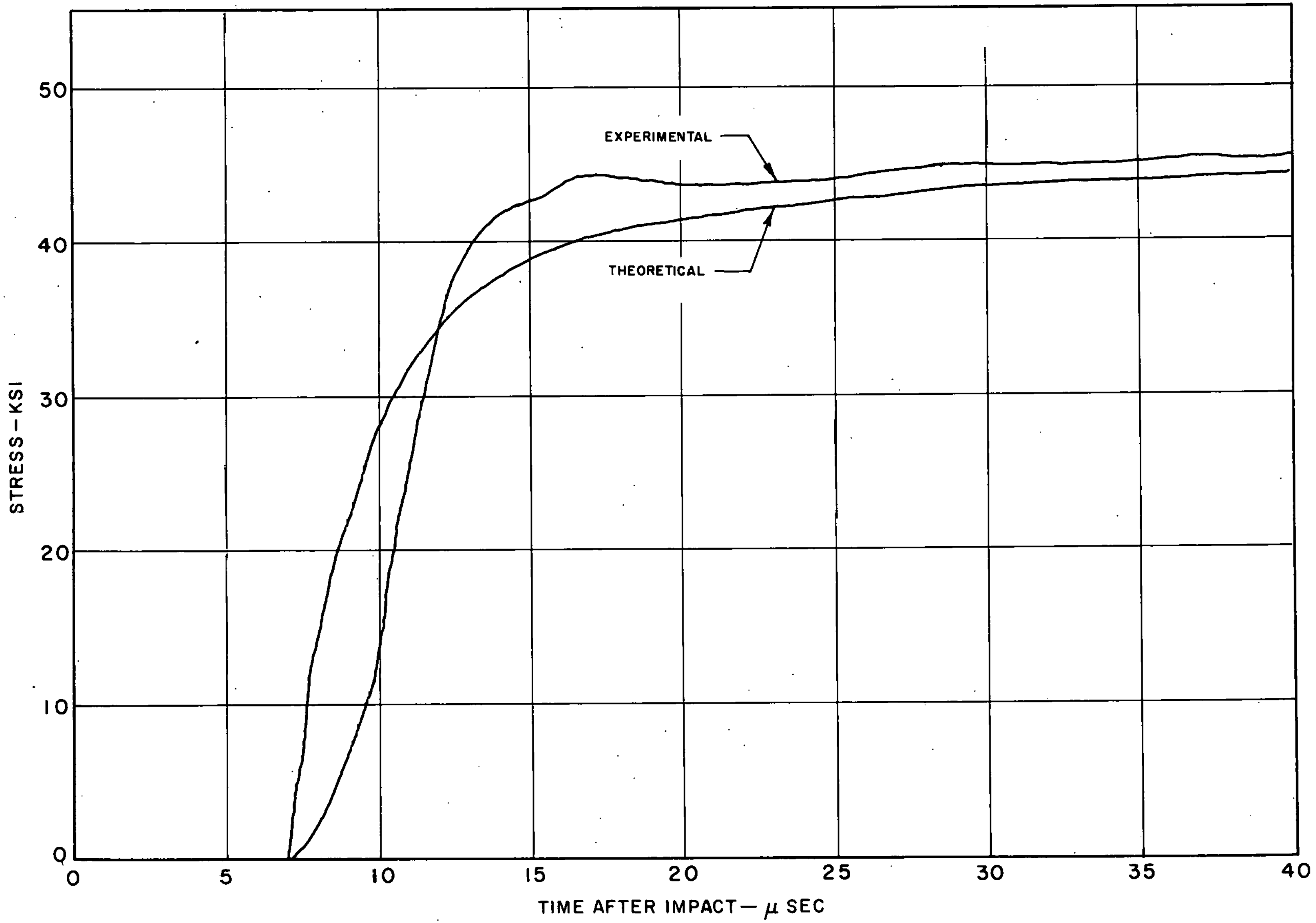

FIG. 41, COMPARISON OF THEORETICAL WITH MEASURED STRESS FOR 65 fps SHOT ON 1 in. COPPER; NONSTRAIN-RATE THEORY

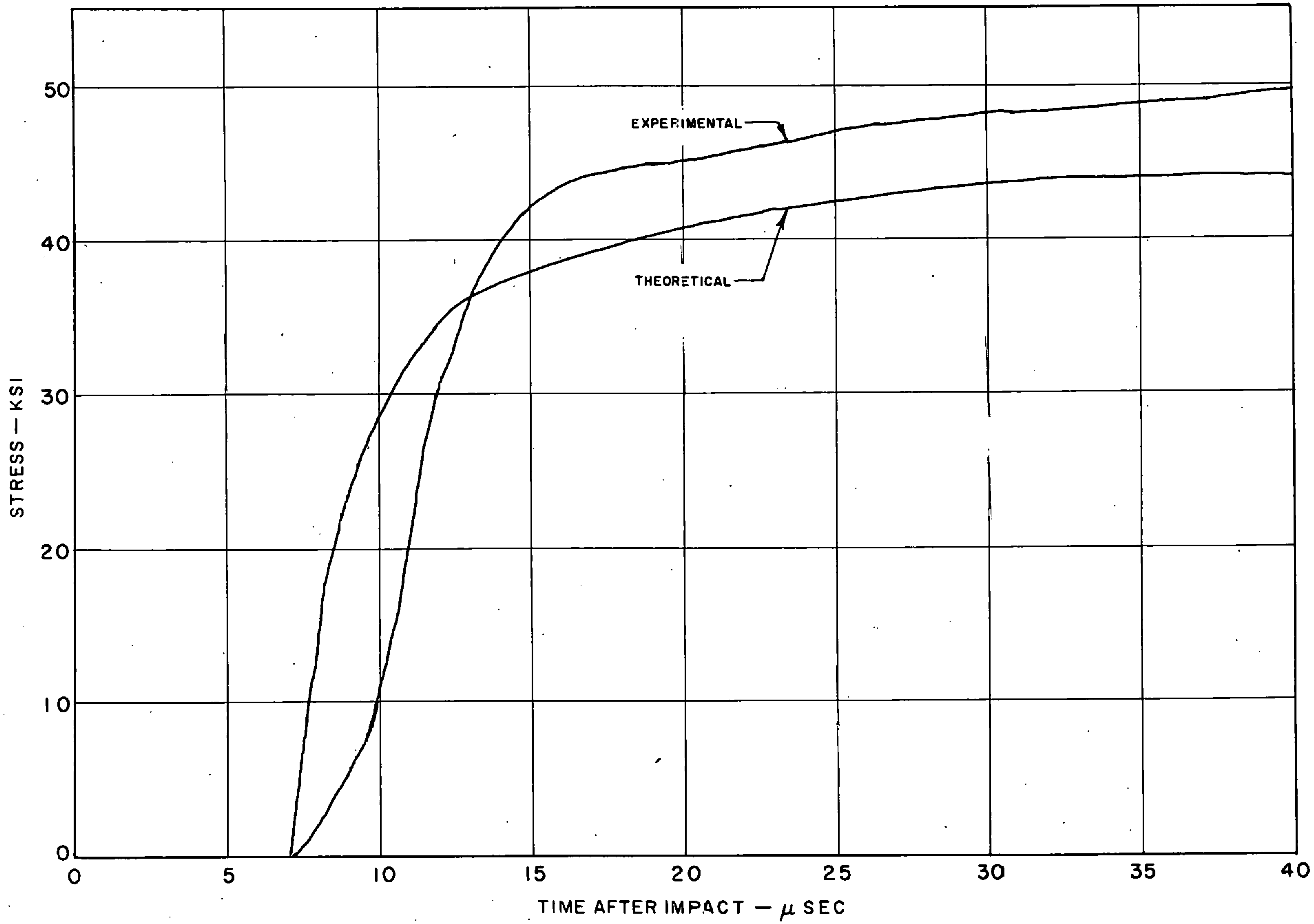

FIG. 42, COMPARISON OF THEORETICAL WITH MEASURED STRESS FOR 110 fps SHOT ON 1 in. COPPER; NONSTRAIN-RATE THEORY

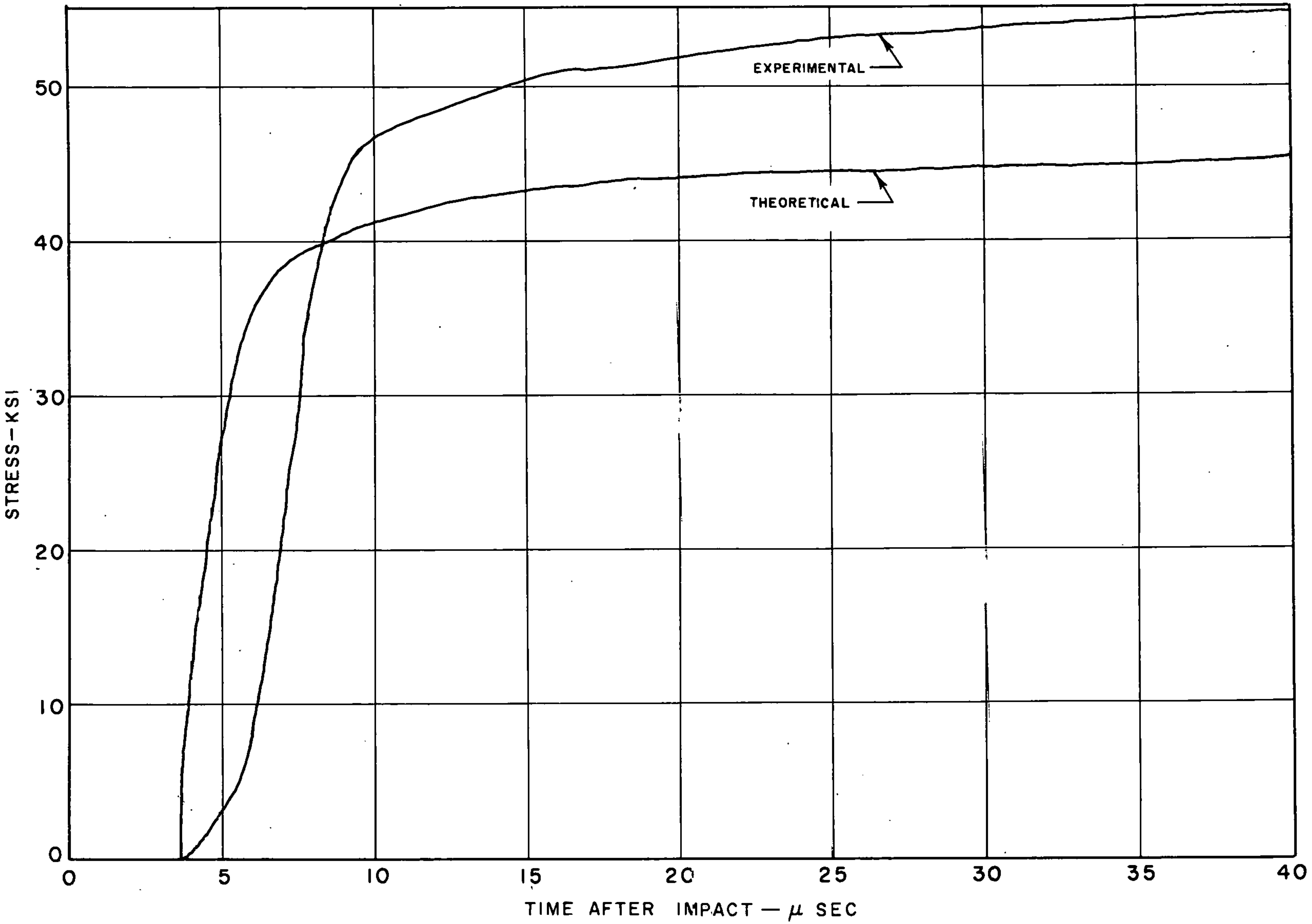

FIG. 43, COMPARISON OF THEORETICAL WITH MEASURED STRESS FOR 65 fps SHOT ON 1/2 in. COPPER; NONSTRAIN-RATE THEORY

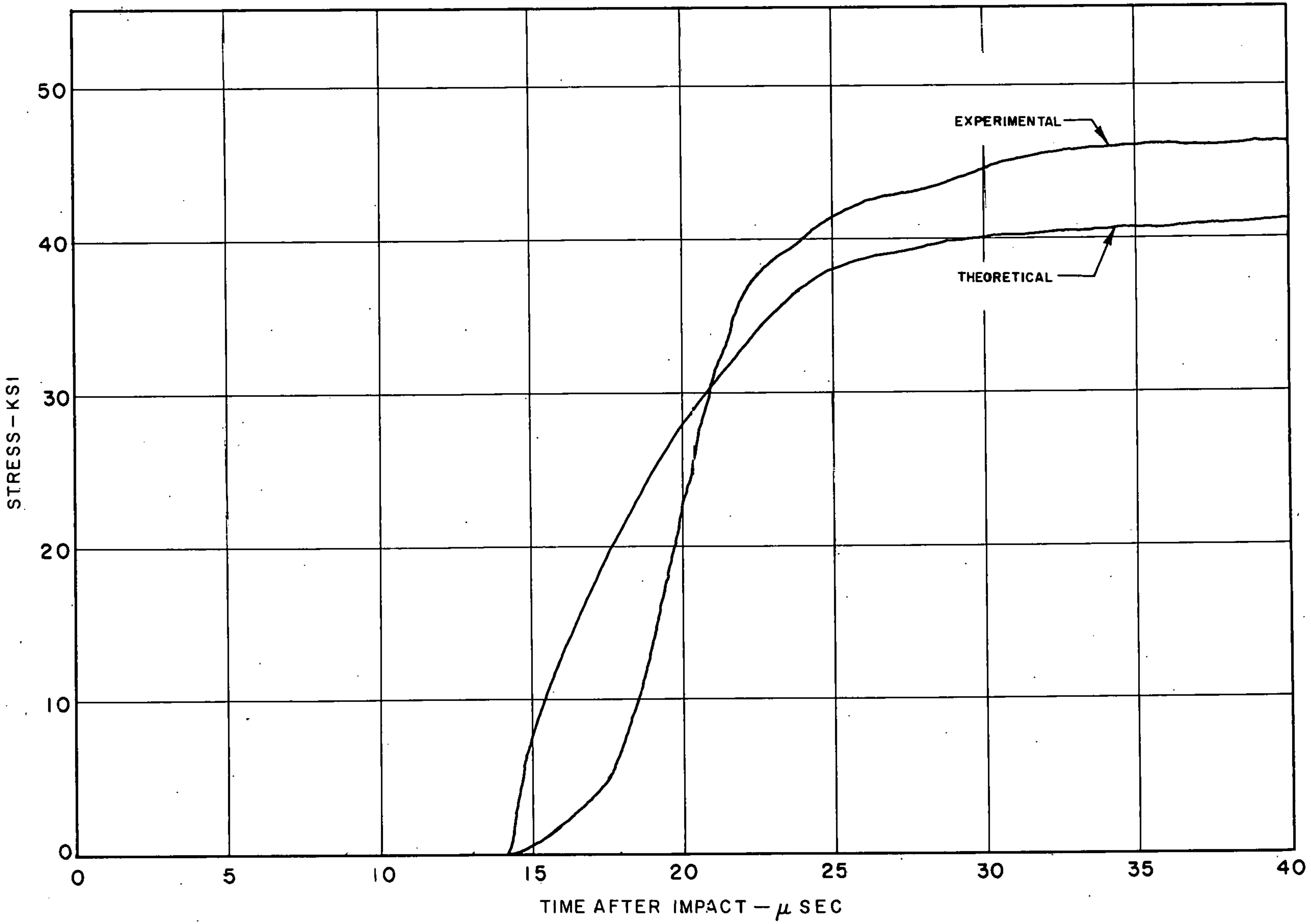

FIG. 44, COMPARISON OF THEORETICAL WITH MEASURED STRESS FOR 65 fps SHOT ON 2 in. COPPER; NONSTRAIN-RATE THEORY

33-fps shot on the 1-in. specimens as shown in Fig. 36. In Fig. 41, the stress measured on the 1-in. specimens impacted at 65 fps is approximately 10 per cent greater at the peak, but then drops to a value only slightly larger than the theoretical curve as time increases. The stress measured on the 1-in. specimens impacted at 110 fps as shown in Fig. 42 is 50, 000 psi as compared to the 45, 000 psi predicted by theory. The greatest difference in the magnitude of measured and theoretical stresses occurs in Fig. 43 for the 65-fps impact on the 1/2-in. specimens. The maximum measured stress is approximately 55, 000 psi while the maximum theoretical stress is only 45, 000 psi.

This is a difference of 10, 000 psi as compared to 5, 000 psi for the 65-fps shot on the 1-in. specimens. This indicates that there is definitely a strain-rate effect and that a shorter specimen has more effect than a higher impact velocity in producing higher measured stresses.

In Fig. 44, the maximum stress produced by the 65-fps shot on the 2-in. specimens is 46, 000 psi which is practically the same as that produced by the same velocity on the 1-in. specimens. This pattern has been obtained before in Ref. (10) when it was found that the maximum stress produced by an impact was affected only slightly by the length if the length-to-diameter ratio were greater than two and the diameter were held constant.

33-fps shot on the 1-in. specimens as shown in Fig. 36. In Fig. 41, the stress measured on the 1-in. specimens impacted at 65 fps is approximately 10 per cent greater at the peak, but then drops to a value only slightly larger than the theoretical curve as time increases. The stress measured on the 1-in. specimens impacted at 110 fps as shown in Fig. 42 is 50,000 psi as compared to the 45,000 psi predicted by theory. The greatest difference in the magnitude of measured and theoretical stresses occurs in Fig. 43 for the 65-fps impact on the 1/2-in. specimens. The maximum measured stress is approximately 55,000 psi while the maximum theoretical stress is only 45,000 psi.

This is a difference of 10,000 psi as compared to 5,000 psi for the 65-fps shot on the 1-in. specimens. This indicates that there is definitely a strain-rate effect and that a shorter specimen has more effect than a higher impact velocity in producing higher measured stresses.

In Fig. 44, the maximum stress produced by the 65-fps shot on the 2-in. specimens is 46,000 psi which is practically the same as that produced by the same velocity on the 1-in. specimens. This pattern has been obtained before in Ref. (9) when it was found that the maximum stress produced by an impact was affected only slightly by the length if the length-to-diameter ratio were greater than two and the diameter were held constant.

The comparisons of the measured strains with those predicted by the theory are shown in Figs. 45 through 49. For every test condition, the strains measured at the impact end of the specimens are from 30 to 50 per cent less than those predicted by theory. The initial slopes of the measured curves are also considerably lower. This may be due to the assumption that the projectile is rigid.

The strains measured at the bar end of the 1-in., 33 fps and the 1/2-in., 65-fps tests in Figs. 45 and 48 are considerably lower than the theory predicts. However, the bar end strains for the 1-in. 65 and 110 fps and 2-in., 65-fps tests agree reasonably well with the respective theoretical curves as shown in Figs. 46, 47, and 48.

It was mentioned before that the measured strains at the bar end for the 65 and 110 fps shots were very nearly equal. The reason for this can be seen in Fig. 17 which is the diagram of state for copper mounted on the elastic bar and impacted with a velocity of 65 fps. The step which represents the maximum stress wave is the plateau numbered 10 in the figure. If the stress waves resulting from step 10 are followed down the bar, *i. e.*, steps μ, ν, ξ , etc., it can be seen that the effects of step 10 could not be observed at the pressure bar until $C_o t/L$ is greater than eight, which corresponds to a time of 56 μsec for a 1-in. specimen. Therefore, for the time shown in Fig. 47, according to the nonstrain-rate theory, the strains at the bar end of the specimens impacted at 65 and 110 fps are exactly the same.

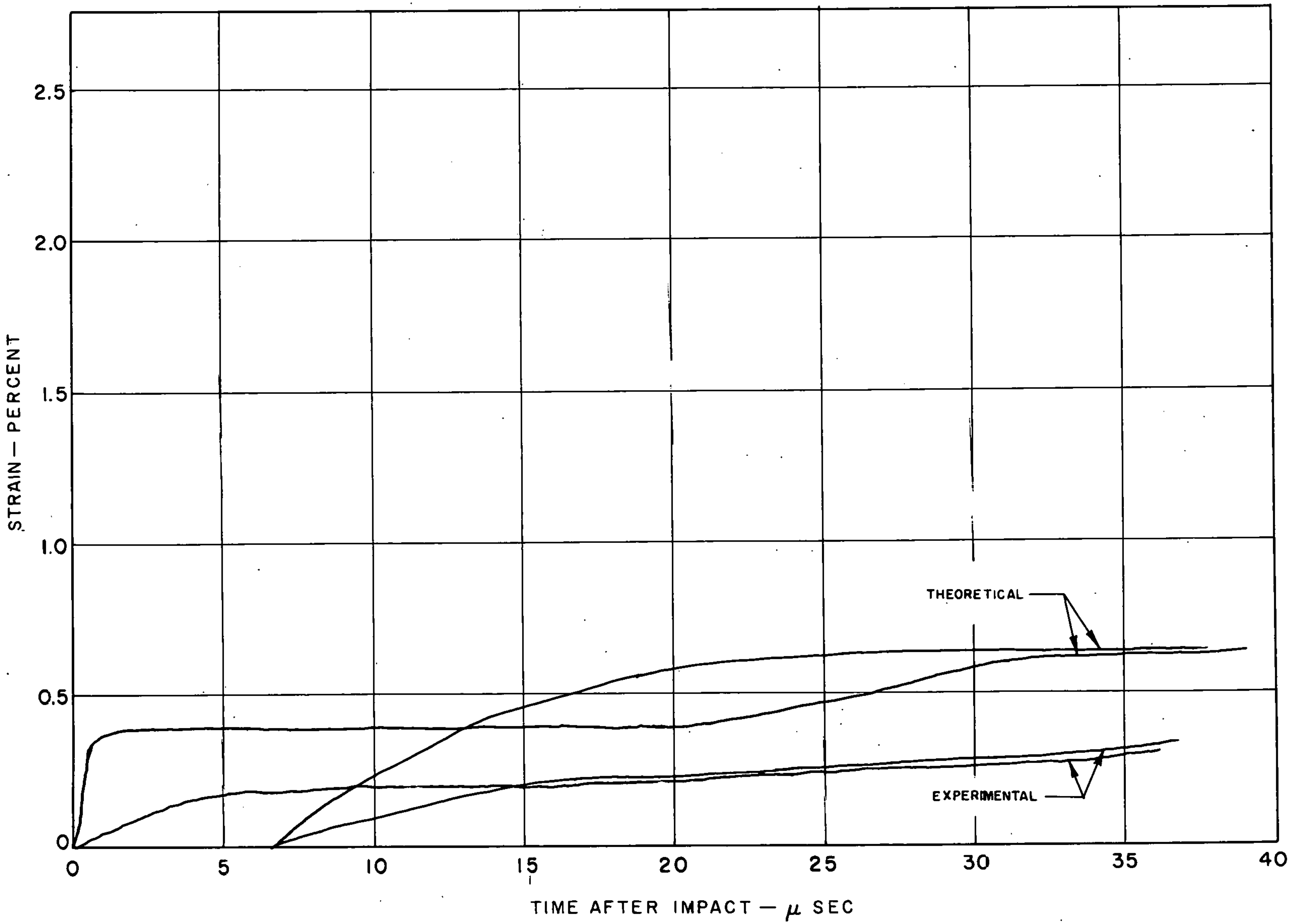

FIG. 45, COMPARISON OF THEORETICAL WITH MEASURED STRAINS FOR 33 fps SHOT ON 1 in. COPPER; NONSTRAIN-RATE THEORY

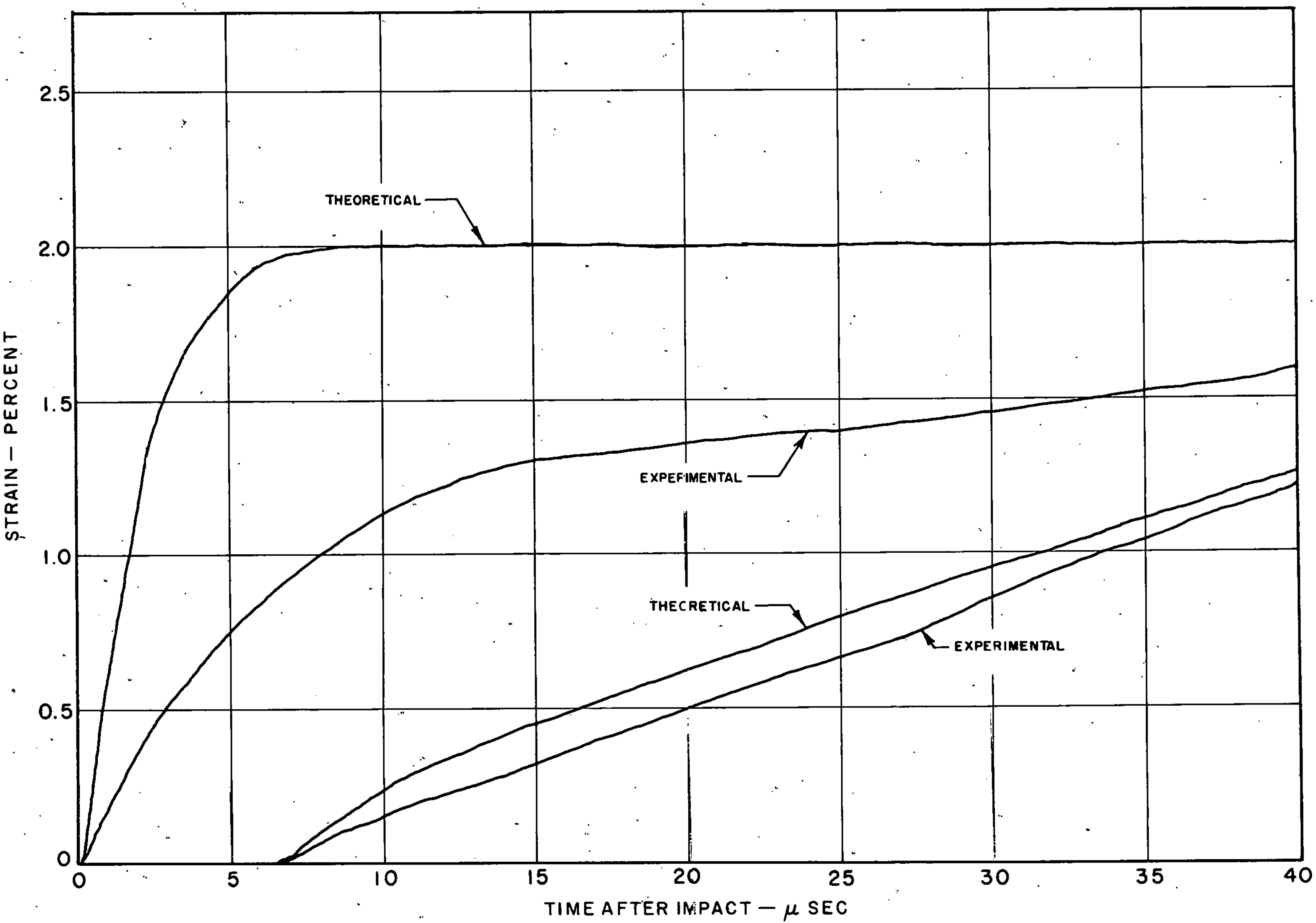

FIG. 46, COMPARISON OF THEORETICAL WITH MEASURED STRAINS FOR 65 fps SHOT ON 1 in. COPPER; NONSTRAIN-RATE THEORY

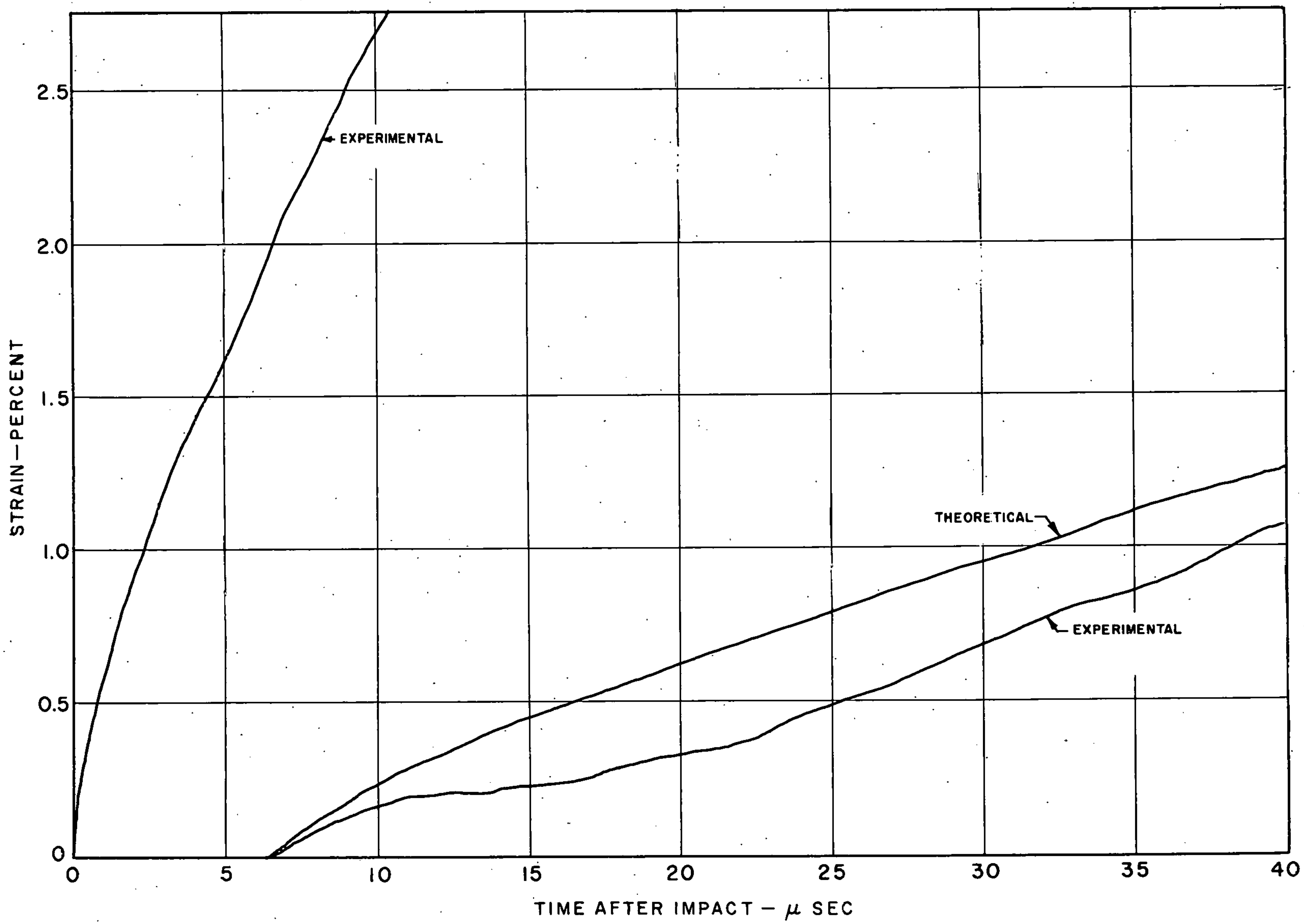

FIG. 47, COMPARISON OF THEORETICAL WITH MEASURED STRAINS FOR 110 fps SHOT ON 1 in. COPPER; NONSTRAIN-RATE THEORY

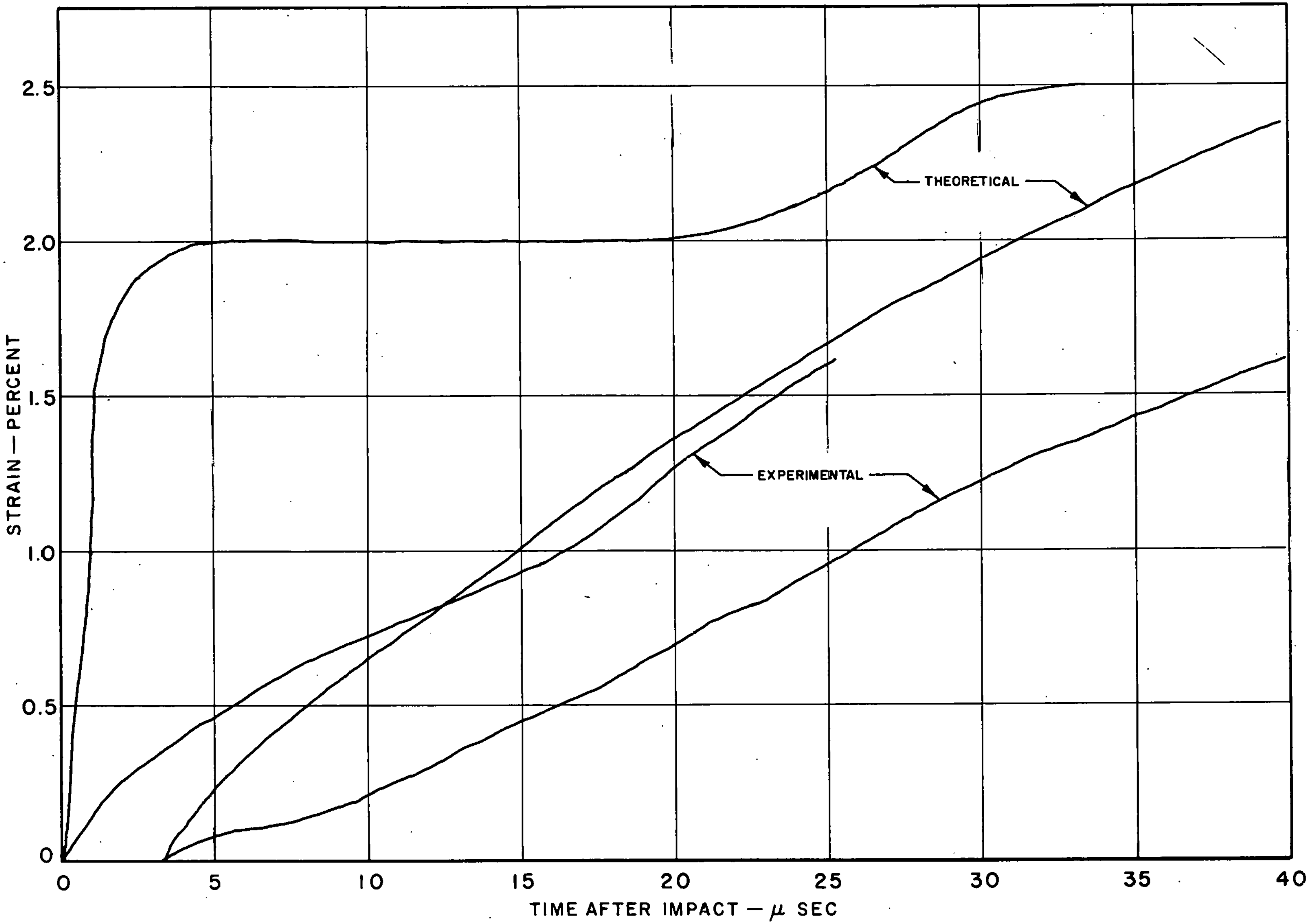

FIG. 48, COMPARISON OF THEORETICAL WITH MEASURED STRAIN FOR 65 fps SHOT ON 1/2 in. COPPER; NONSTRAIN-RATE THEORY

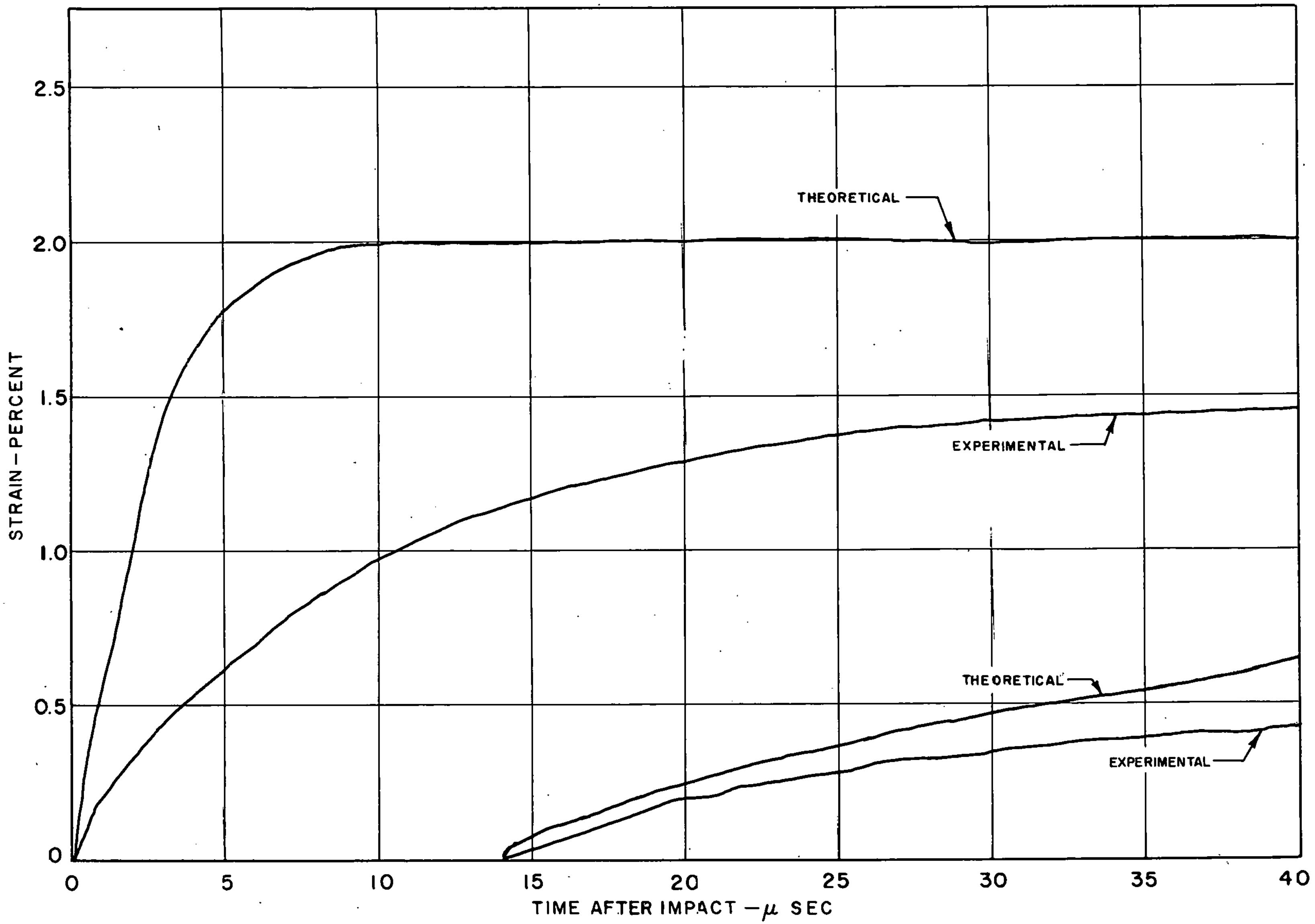

FIG. 49, COMPARISON OF THEORETICAL WITH MEASURED STRAINS FOR 65 fps SHOT ON 2 in. COPPER; NONSTRAIN-RATE THEORY

In Fig. 48 for the 1/2-in. specimens impacted at 65 fps, the theoretical strain at the impact end reaches a plateau of 2 per cent and then begins to rise again after 20 μsec has lapsed. This second rise is produced by the arrival at the impact end of the first reflected wave. This increase is somewhat substantiated by a corresponding rise in the strain which was measured at the impact end, although the magnitude of the measured strain differs. The time at which the corresponding rise of measured strain occurs is about 17 μsec after impact, but since the strain is lower than that predicted the reflected strain wave should arrive sooner because it is being propagated faster.

In Ref. (2), dynamic stress-strain curves were constructed by measuring stress versus time and assuming the strain to be equal to $\frac{Vt}{L}$. This assumption is repudiated by the strain-time records obtained in this study.

In order to calculate the strain rate, the slopes of the experimental strain-time curves must be obtained. Differentiating an experimentally obtained curve is a very crude process, especially if there are any unexplained variations in the curves or if there is much scatter among curves taken under the same conditions. At best, only an estimate of the strain rate can be obtained from the curves resulting from these experiments. The slopes of the strain-time curves for both the impact and bar ends for copper for each test condition are shown in Table IV. The theoretical average strain rate over the length of the specimen is listed in the column labeled V/L. The impact velocity and specimen length are listed also.

TABLE IV. Measured and Average Strain Rates

V	L	V/L	Strain Rate 1/sec	
in./sec	in.	1/sec	Impact end	Bar end
780	1/2	1560	3000	480
1300	1	1300	3000	300
780	1	780	2000	370
396	1	396	500	250
780	2	390	1300	250

There is a wide range of values for the measured strain rate, especially for the impact end. Logically, one would assume that the strain rate at the impact end would depend on the impact velocity alone instead of V/L, since the material at the impact end cannot detect an effect of the length until some time after impact. Conversely, the strain rate at the bar end should depend on the length alone as long as the velocity is such that a plastic wave reaches the bar end. The figures in the table follow this pattern somewhat, although they are inaccurate. The relationship between the strain rate at the impact end and V/L seems to be meaningless, although there appears to be some pattern in the relationship between V/L and the strain rate at the bar end. This pattern for copper is demonstrated by plotting the ratio of measured strain rate, $\dot{\varepsilon}_m$, to V/L as a function of impact velocity as shown in Fig. 50. The strain rate $\dot{\varepsilon}_m$ used for this plot was measured at the bar end of the specimen. It is seen that as the impact velocity increases, the ratio $\dot{\varepsilon}_m/V/L$ decreases for the 1-in. specimens. This is contrary to the results reported by Turnbow[2] as shown by the dashed lines in the figure. Although the results reported here cover a different range of impact velocities, the point for the lowest impact velocity falls in the center of Turnbow's data.

Turnbow made his measurements on hollow aluminum and copper tubes, instead of solid cylinders, with gages placed in the center of the specimens. This difference in technique could very well account for the disagreement in results. In any case, there is not enough information to draw a definite conclusion.

The variation of $\dot{\varepsilon}_m/V/L$ with specimen length for a constant impact velocity of 780 ips, is shown in Fig. 51. For shorter lengths, the quantity $\dot{\varepsilon}_m/V/L$ decreases for lengths as short as 1/2-in. which agrees with Turnbow (see Fig. 50). However, one must logically conclude that as the length gets very short, the measured strain rate must approach V/L, that is, if the projectile and pressure bar are rigid compared to the specimen. For a copper specimen and a steel

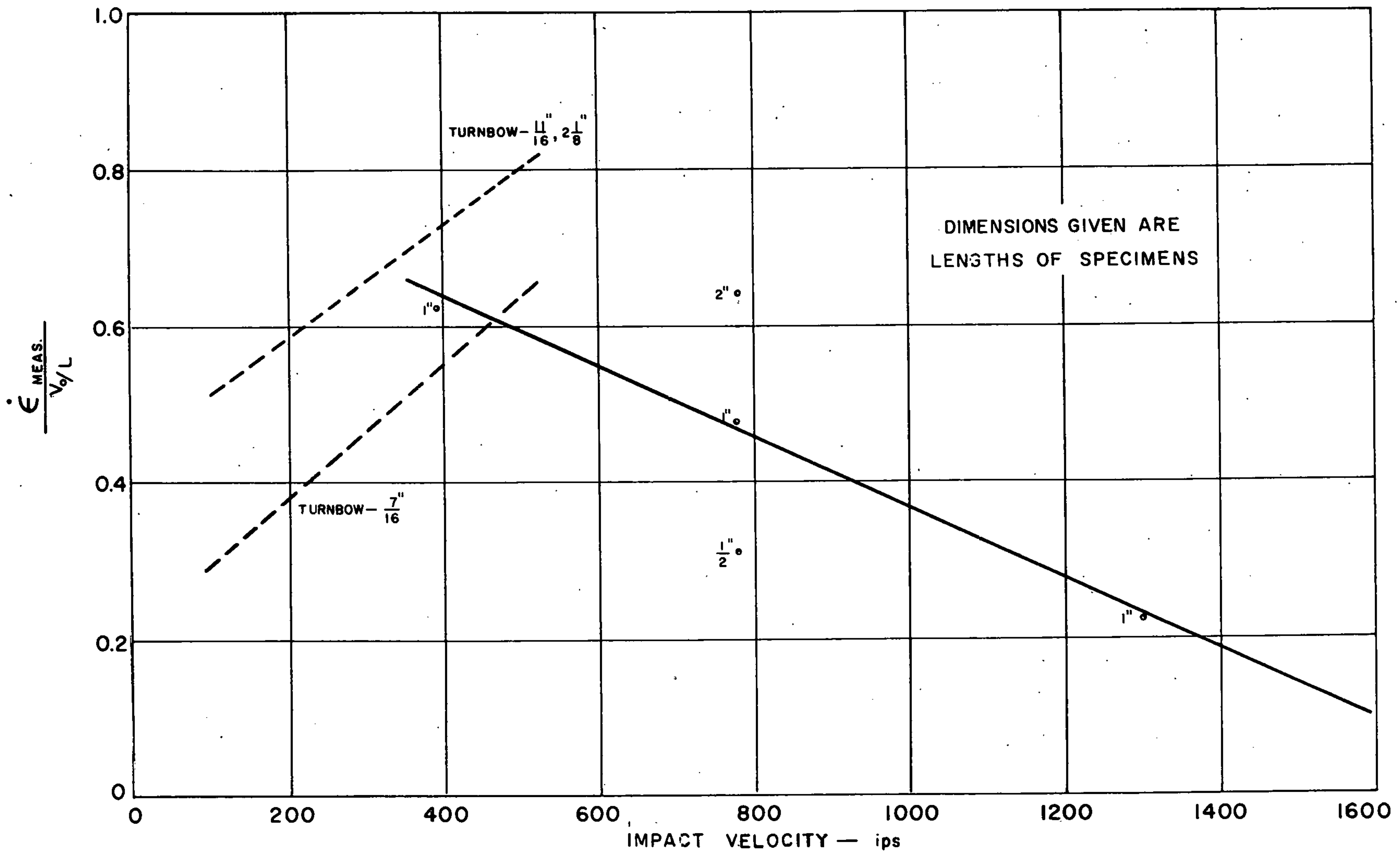

FIG. 50, RATIO OF $\dot{\epsilon}_m/V/L$ VERSUS IMPACT VELOCITY FOR COPPER

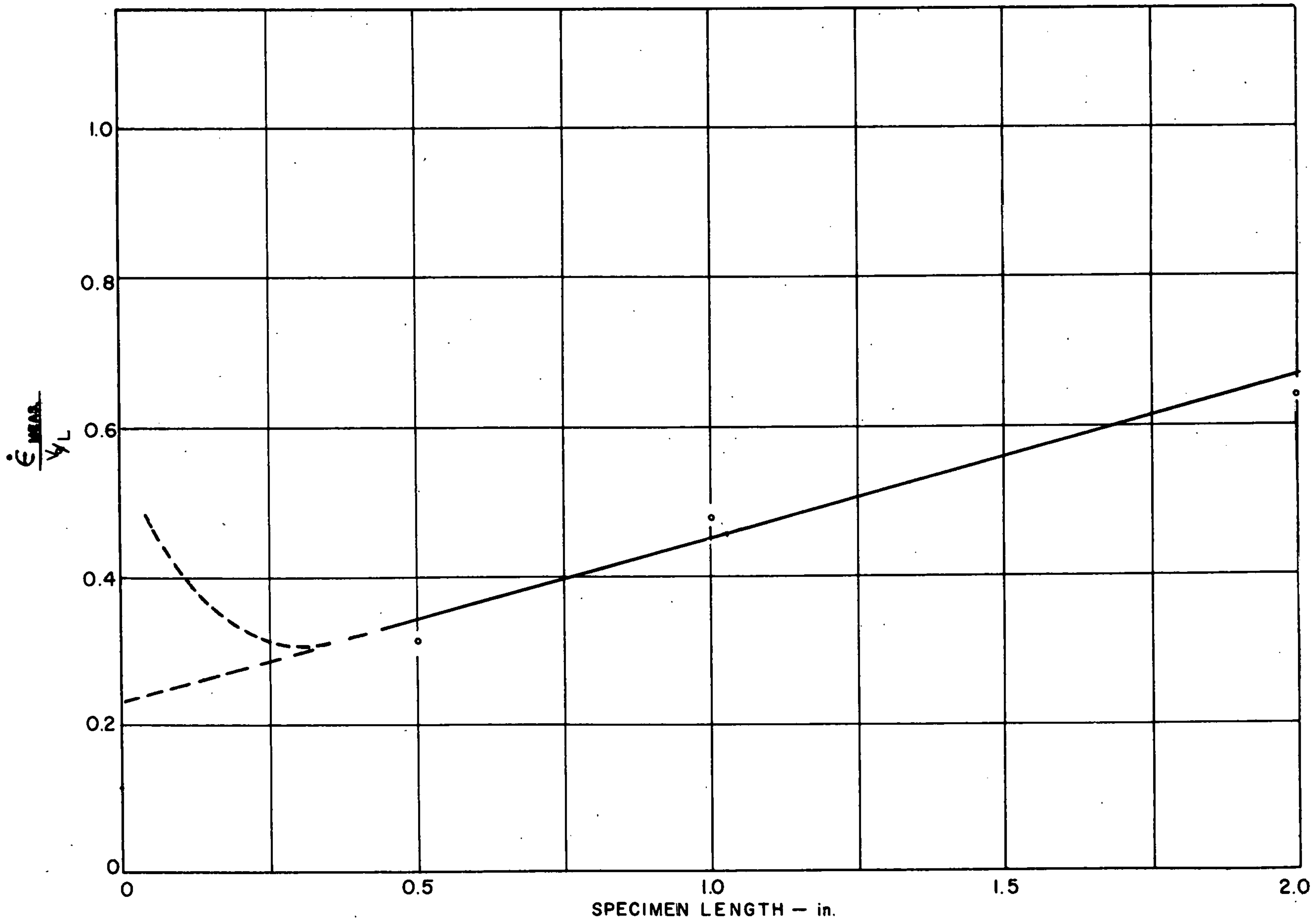

FIG. 51, RATIO OF $\dot{\epsilon}_m / V/L$ VERSUS LENGTH FOR IMPACTS OF 780 ips ON COPPER projectile and pressure bar, one would expect $\dot{\varepsilon}_m/V/L$ to approach some number less than 1.0, but certainly greater than 0.2 as is indicated by a continuation of the straight line in Fig. 51. Therefore, the curve in Fig. 51 should turn up as the specimen length approaches zero as indicated by the curved dashed line, though there are no tests to support this postulation.

Lead. The comparisons of the experimental to the theoretical results for lead are shown in Figs. 52 and 53. Fig. 52 shows that the measured and experimental strains at the bar end of the specimen agree very well for the first 100 μsec after impact. The sudden rise in the theoretical curve at that time is caused by the arrival of several strain steps traveling at very nearly the same velocity. The magnitude of the strain measured at the impact end is in fair agreement with the theory although the shapes of the initial parts of the curves differ considerably. The tail end of the theoretical curves are dashed because of the lack of accuracy for the higher strains. The rise of the theoretical strain at the impact end after about 120 μsec is caused by the arrival of a reflected wave from the fixed end. A corresponding rise is observed experimentally, also.

The theoretical and measured stresses are compared in Fig. 53. The wave shapes are very similar, but the theoretical stress is about 30 per cent less than that which was measured. This indicates that lead is definitely strain-rate dependent and does not follow the static stress-strain curve during an impact.

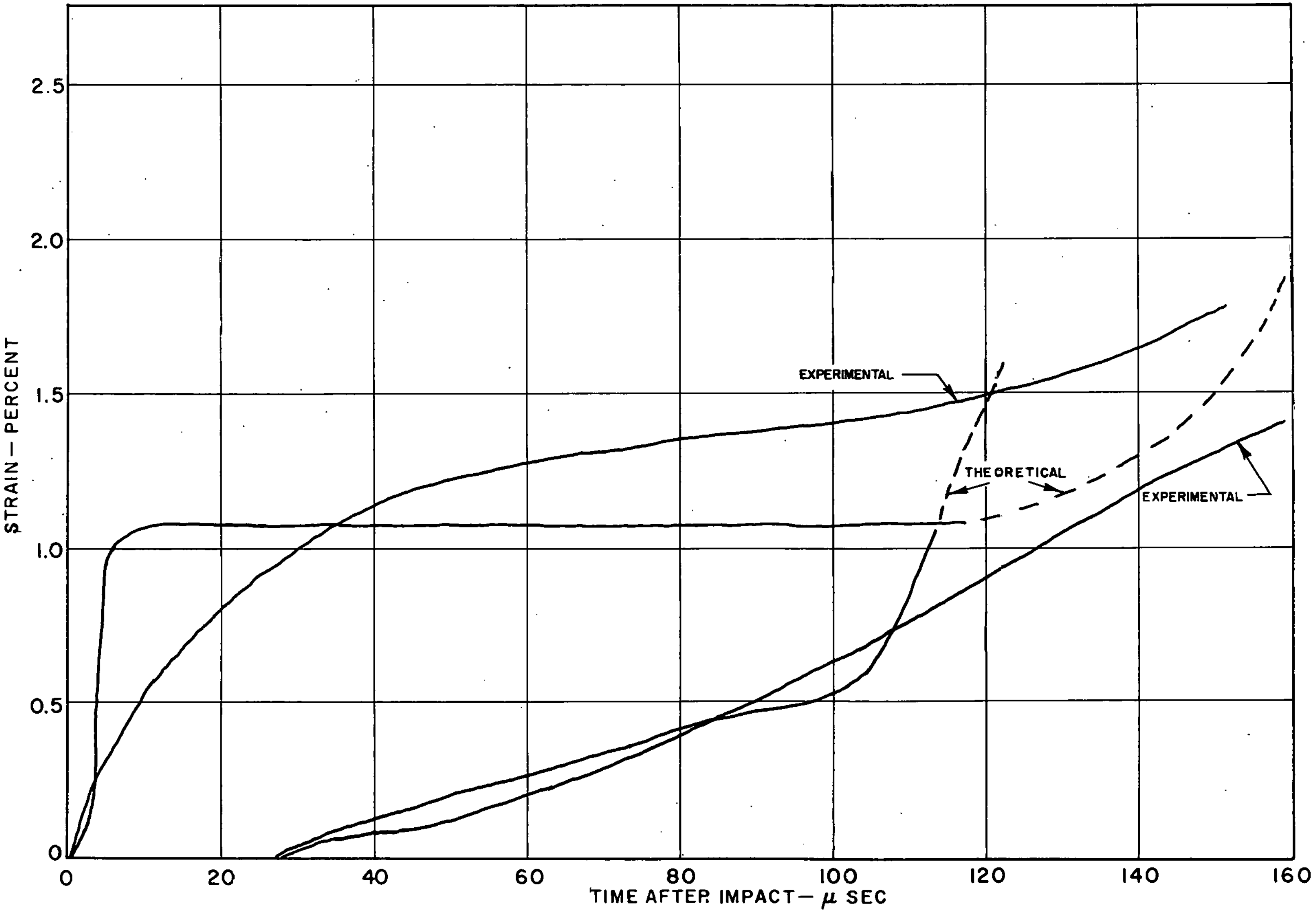

FIG. 52, COMPARISON OF THEORETICAL AND MEASURED STRAINS FOR 10 fps SHOT ON LEAD; NONSTRAIN-RATE THEORY

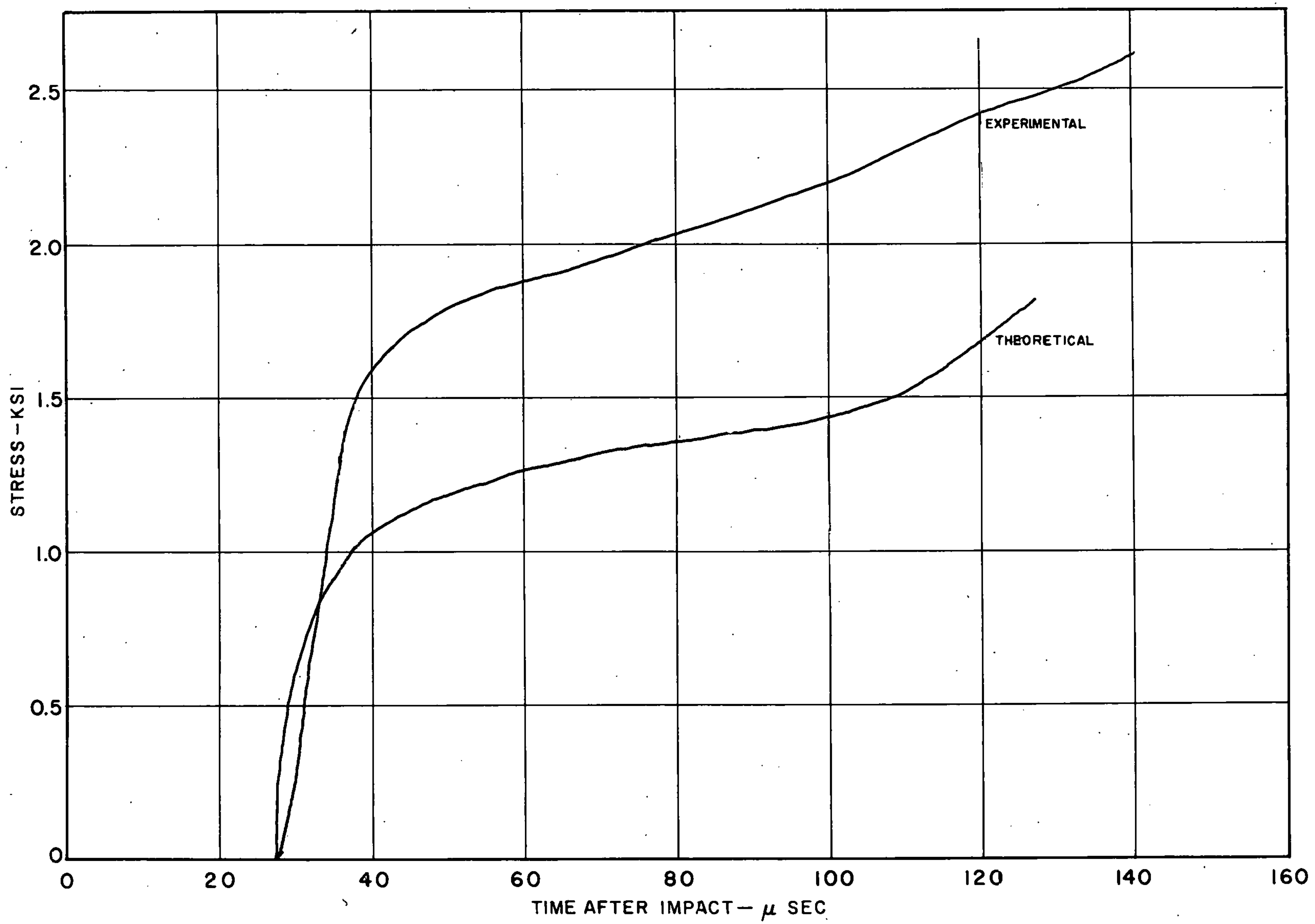

FIG. 53, COMPARISON OF THEORETICAL AND MEASURED STRESSES FOR 10 fps SHOT ON LEAD; NONSTRAIN-RATE THEORY

As was stated previously, if a material is suspected of being strain-rate dependent, an improvised stress-strain curve may be drawn to simulate the effects of strain rate. Such a stress-strain curve was presented in Fig. 21. The stress and strain at the bar end of a specimen following the "dynamic" curve were shown in Fig. 22.[*] These quantities are replotted in Fig. 54 where they are compared with the measured stress and strain at the bar end. The use of the "dynamic" stress-strain curve increased the strain slightly so that it does not agree with the measured strain as well as that from the static stress-strain curve. However, the stress was increased considerably so that it compares very favorably with the measured stress. Even better agreement would have been obtained had a "dynamic" stress-strain curve of higher stresses been used.

---

[*] The "dynamic" stress-strain curve shown in Fig. 21 is one obtained when a strain-rate-sensitive material obeying a linear strain-rate law is subjected to a <u>constant</u> strain rate only, but since the strains measured at the bar end were linear with time, the technique described is valid.

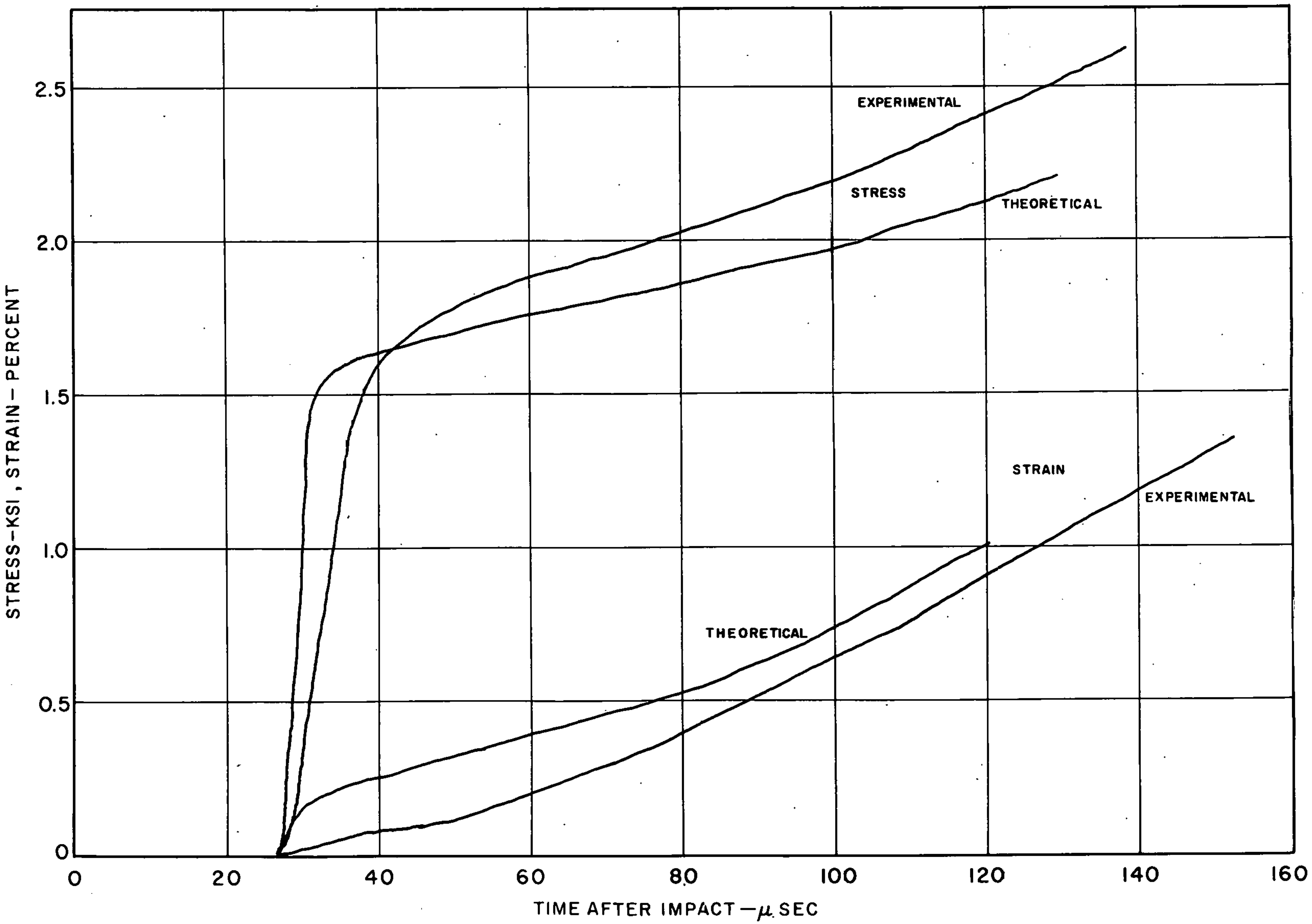

FIG. 54, COMPARISON OF MEASURED WITH THEORETICAL RESULTS BASED ON A "DYNAMIC" STRESS-STRAIN CURVE FOR LEAD; NONSTRAIN-RATE THEORY

Comparison of Experimental with Nonstrain-Rate and Strain-Rate Theories

The results of the experiments are compared with the elementary and strain-rate theories in Figs. 55 through 60. Fig. 55 is the stress-time variation at the bar end of a 1/2-in. copper specimen impacted with a velocity of 65 fps. It can be seen that for values of K equal to 60×10^4/sec and 90×10^4/sec, the strain-rate theory predicts a stress that is approximately 10 per cent above the experimental curve; however, a still higher value of K would reduce the stress predicted by the strain-rate theory so that better agreement could be obtained.

The initial parts of the strain-rate curves rise instantaneously because of the assumed step-velocity impact conditions. Had the particle velocity at the impact end been assumed to rise in a finite interval of time, then the initial parts of the experimental and strain-rate curves would have been in much better agreement.

It is apparent that the strain-rate curve could be made to fit the experimental curve by varying the flow constant K along with the particle velocity rise characteristics at the impact end. This does not necessarily indicate that the strain rate mechanism gives a correct phenomenological description of plastic wave propagation, however. Radial inertia may affect the observed strains and stresses in the same way they are affected by strain rate.

A better test of the strain-rate theory would be the comparison of it with the experimental results of tests on a longer specimen where

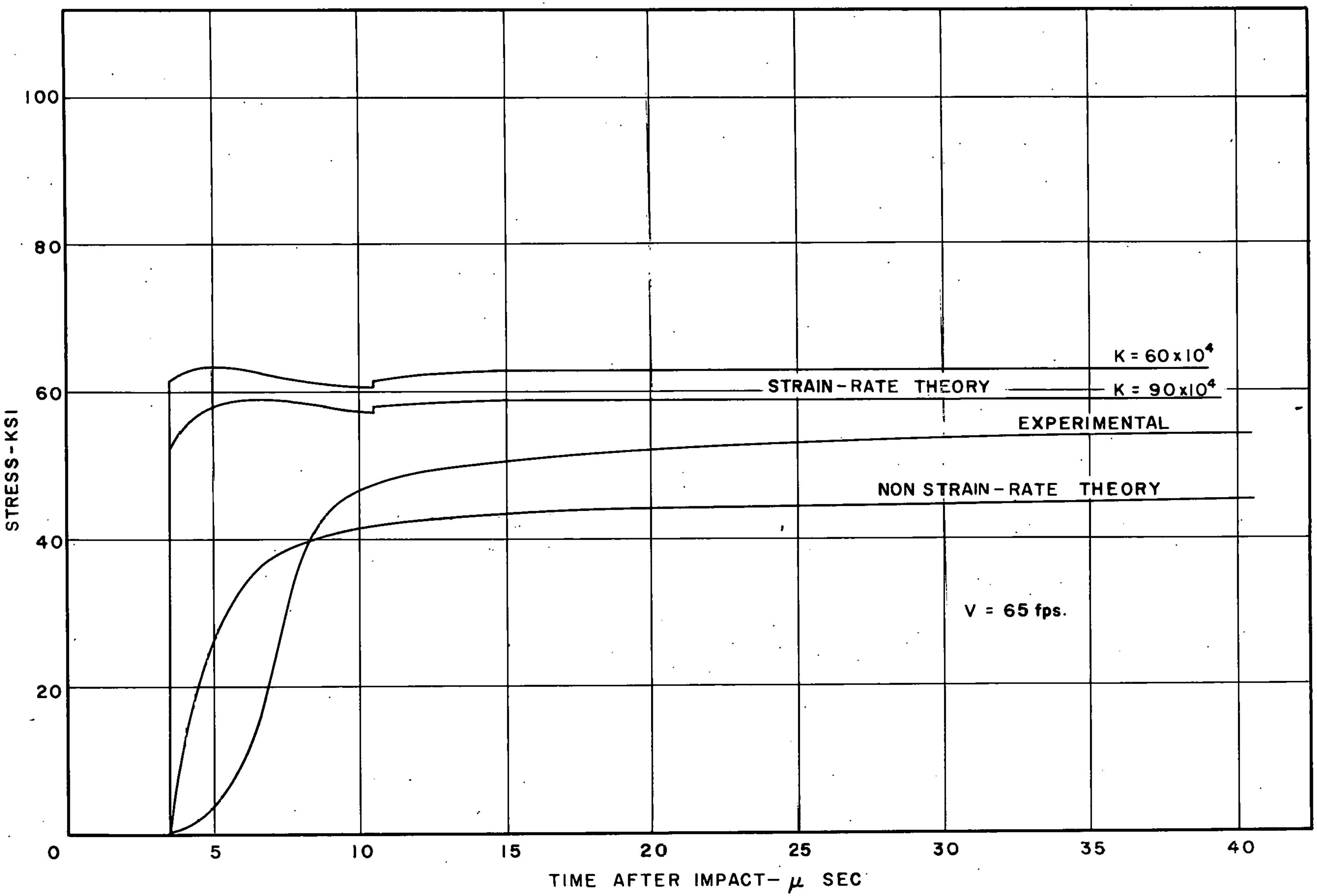

FIG. 55 COMPARISON OF STRESSES AT THE SEMIFIXED END OF ½ in. SPECIMEN

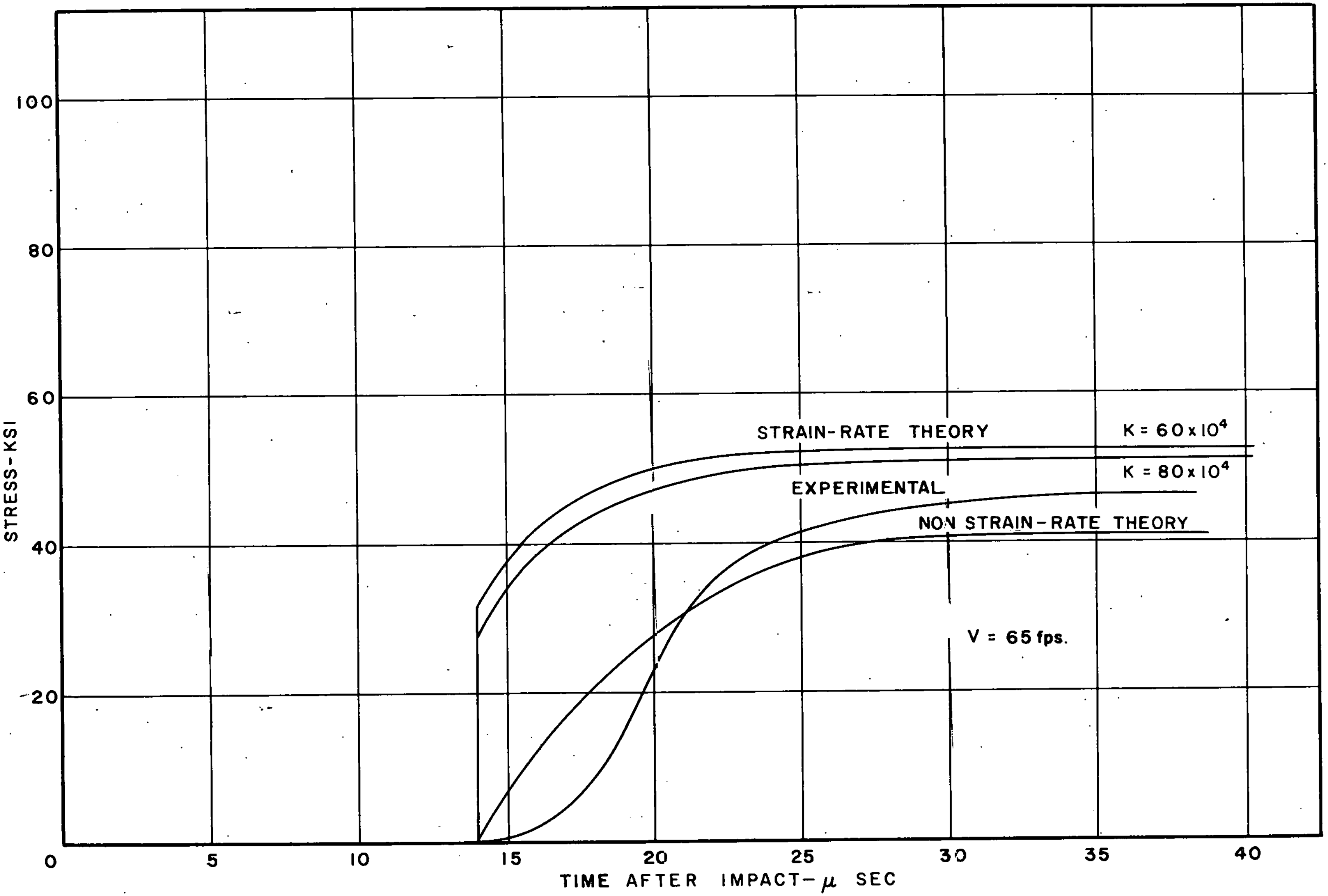

FIG. 56 COMPARISON OF STRESSES AT THE SEMIFIXED END OF 2in. COPPER SPECIMEN

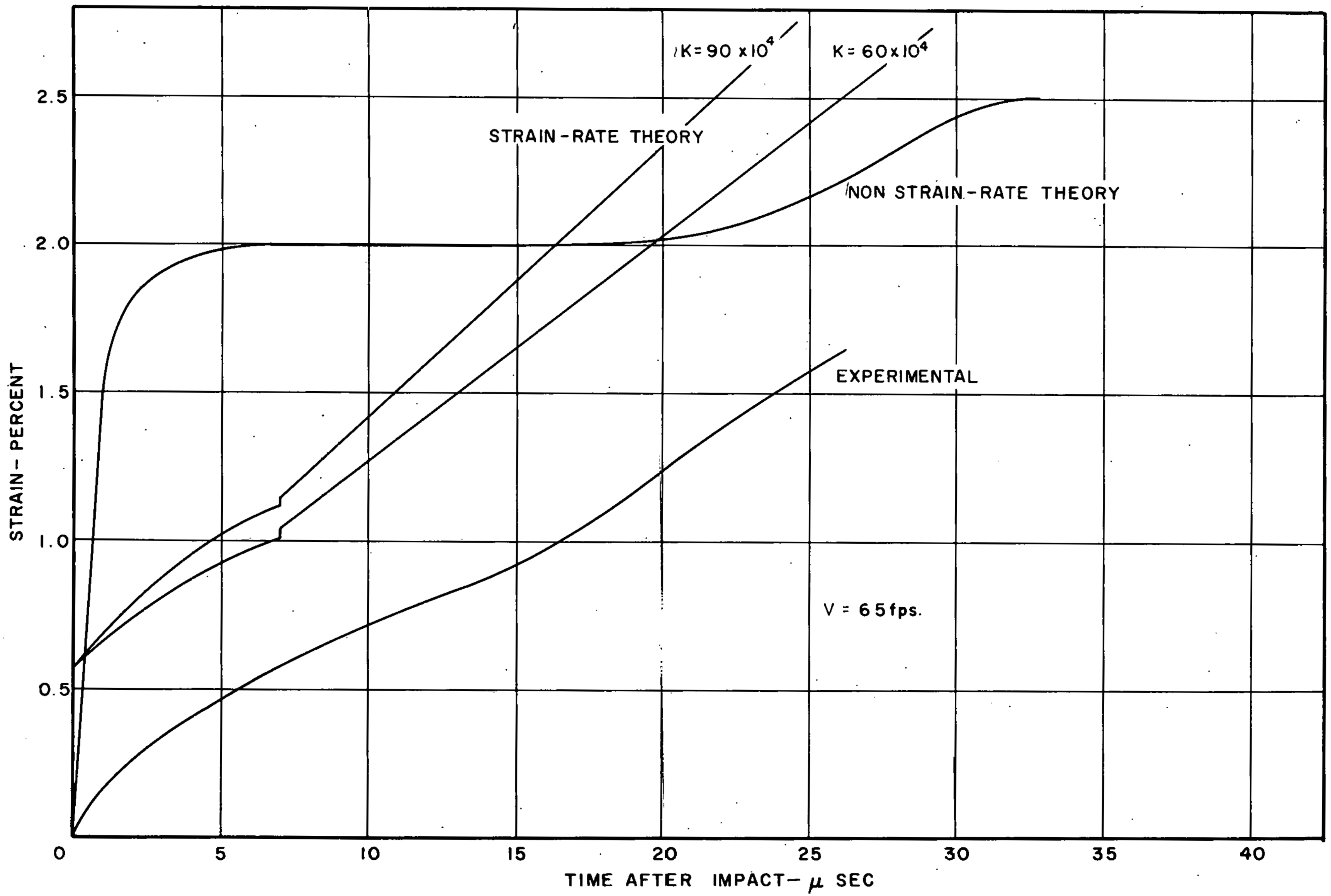

FIG. 57 COMPARISON OF STRAINS AT THE IMPACT END OF ½ in. COPPER SPECIMEN

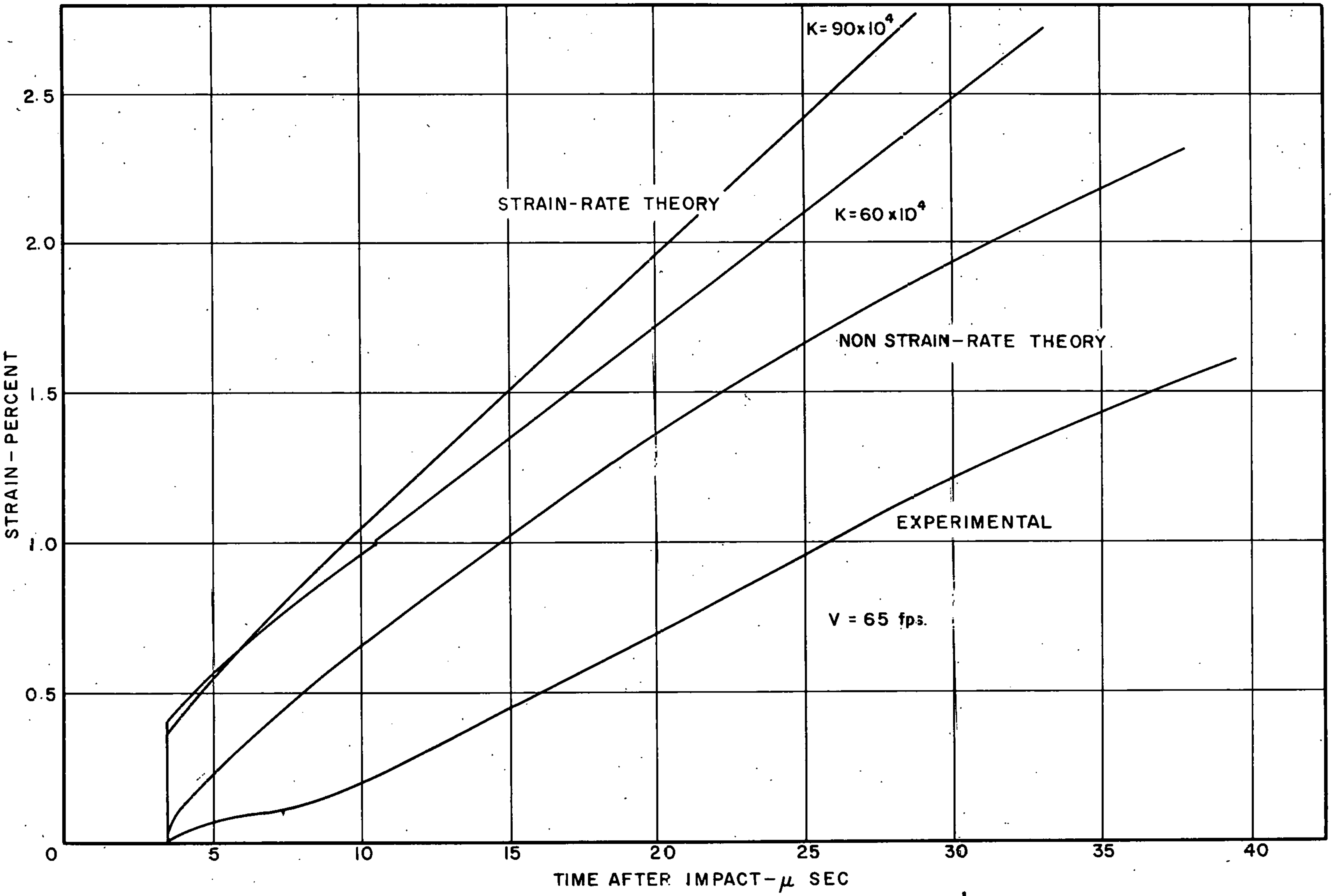

FIG.58 COMPARISON OF STRAINS AT SEMIFIXED END OF $\frac{1}{2}$ in. COPPER SPECIMEN

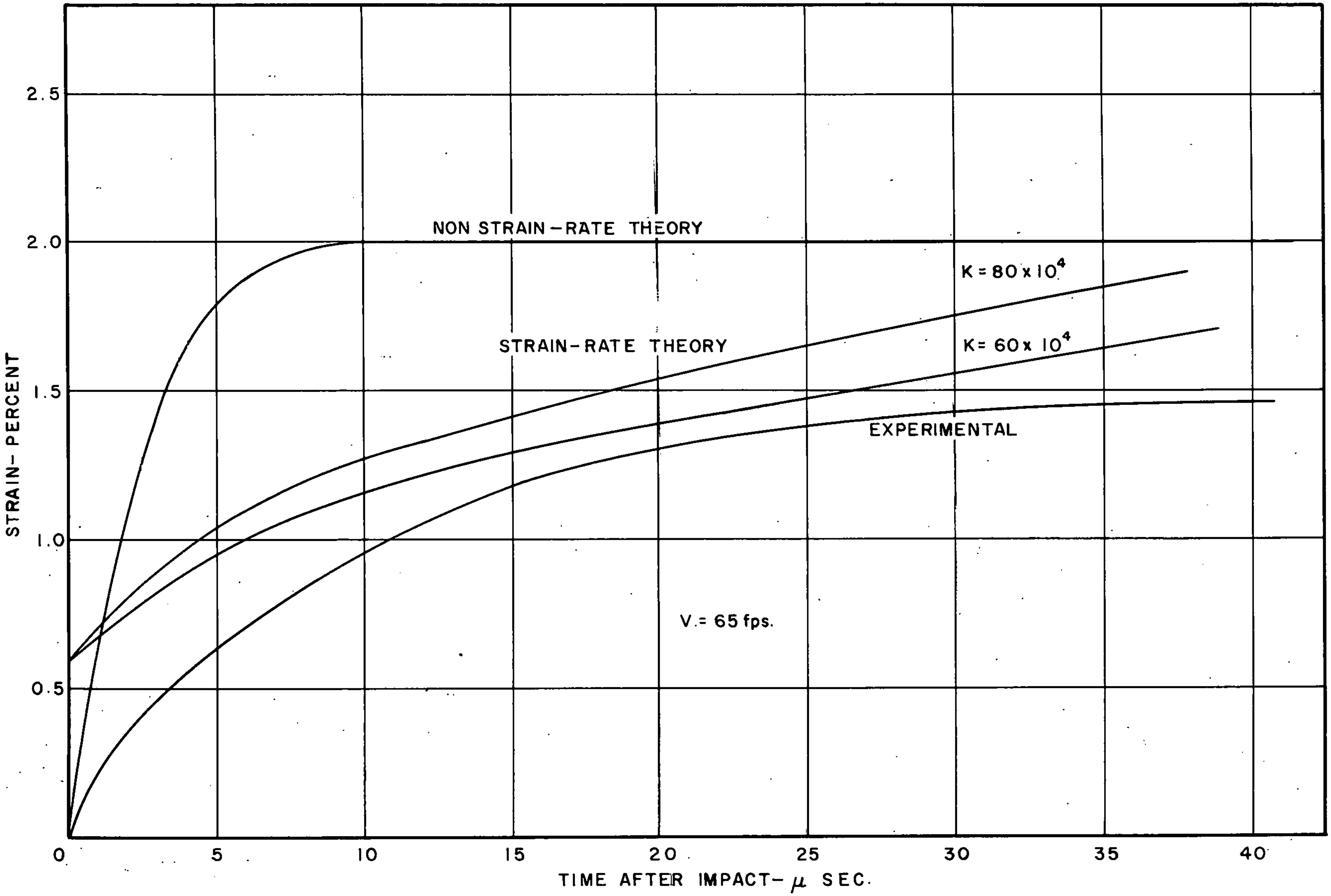

FIG. 59 COMPARISON OF STRAINS AT THE IMPACT END OF 2 in. COPPER SPECIMEN

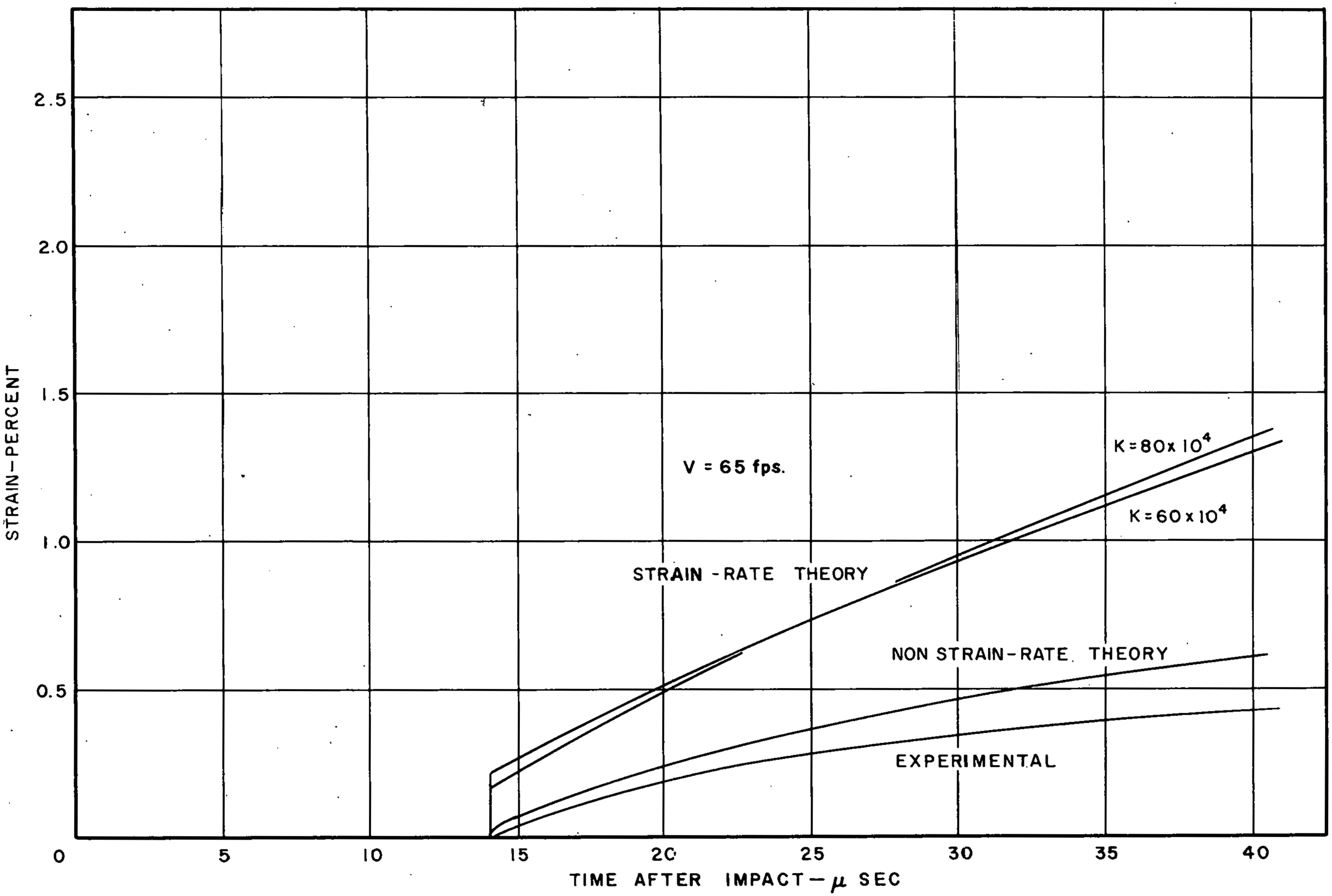

FIG. 60 COMPARISON OF STRAINS AT THE SEMIFIXED END OF 2 in. COPPER SPECIMEN

the radial inertia is no longer significant. Fig. 56 shows a set of results for a 2-in. specimen. The values of K for which the strain-rate curves are shown, are 60×10^4/sec and 80×10^4/sec. In order to match the experimental curve, it is obvious that a much higher value of K must be chosen and also more realistic impact conditions must be assumed.

Fig. 57 shows the computed and experimental results of the strain history at the impact end of a 1/2-in. copper specimen. The nonstrain-rate curve is considerably different from that which was measured as are the curves representing the strain-rate theory. However, if a finite rise time were assumed in the particle velocity-time variation, the curve for $K = 60 \times 10^4$/sec or less would be in reasonable agreement with the experiment.

Fig. 58 shows the same quantities for the bar end of the 1/2-in. specimen. Here the nonstrain-rate theory is approximately 60 per cent greater than the experiment while the strain-rate curve for $K = 60 \times 10^4$/sec is approximately 120 per cent greater. Even if the step at the beginning of the strain-rate curves were eliminated, the curve for $K = 60 \times 10^4$/sec still would not agree with the experiment because of the difference in slope. A relatively large radial inertia effect in the short specimen could have caused the measured strains to be so much lower than the two theories.

Figs. 59 and 60 show the strain records for the impact end and bar end of the 2-in. copper specimen. In Fig. 59, the strain as predicted by the nonstrain-rate theory is considerably higher than the experimental curve while the strain-rate-theory curves are only slightly higher. If the initial step of the strain-rate curves were removed, the curve for $K = 60 \times 10^4$/sec would be in fair agreement with the experimental curve. It appears that a curve computed for $K = 50 \times 10^4$/sec would be in even better agreement if the step velocity were removed.

The strain-time variations at the bar end of the specimen are shown in Fig. 60. For this condition, the nonstrain-rate theory is about 25 to 30 per cent higher than the experimental curve while the curves from the strain-rate theory are approximately 120 per cent higher. Again, if the particle velocity were assumed to have a finite rise time, the strain-rate-theory curve could be made to fit the experimental curve by proper choice of the flow constant. The proper choice would require that K be decreased to some value less than 60×10^4/sec.

There are two contradictory requirements being placed on the value of K when the stresses and then the strains from the strain-rate theory are compared with the experimental results. The stress records would indicate that K should be approximately 250×10^4/sec while the strain records indicate that it should be less than 60×10^4/sec. Obviously, both of these values cannot be used simultaneously; therefore, the linear approximation of the general strain-rate theory <u>cannot</u> be expected to agree with the experimental results. There still remains, however, the possibility that the more general strain-rate theory can be made to satisfy the experimental results since it contains <u>two</u> flow constants which can be varied independently.

Comparison of Modified Nonstrain-Rate and Strain-Rate Theories

A set of curves was constructed using the nonstrain-rate theory in which a stress-strain curve was assumed such as one would expect from a strain-rate sensitive material subjected to a constant strain rate. The curves were constructed in the same manner as those for lead which were described in the section on the effects of changes in the stress-strain curve, page 42. A modified stress strain curve was chosen so that the maximum stress was approximately 15 per cent higher than the original stress-strain curve as shown in Fig. 61.

The results of the modified nonstrain-rate theory are presented in Figs. 62 and 63 where they are compared with the experiments and the strain-rate theory. Fig. 62 shows the stresses at the bar end of the 1/2-in. specimen. It is apparent that if the input particle velocity had a finite rise time, the strain-rate theory, by adjusting K , could be made to match exactly the modified nonstrain-rate-theory curve. The maximum value of the stress-strain curve (Fig. 61) used in the modified nonstrain-rate theory was selected to correspond to the maximum stress on the experimental curve.

Fig. 63 shows the three stress curves for the 2-in. specimens. Again, it appears feasible that the strain-rate curve could be made to fit almost exactly the modified nonstrain-rate-theory curve and both would agree very favorably with the experimental curve. However, there still

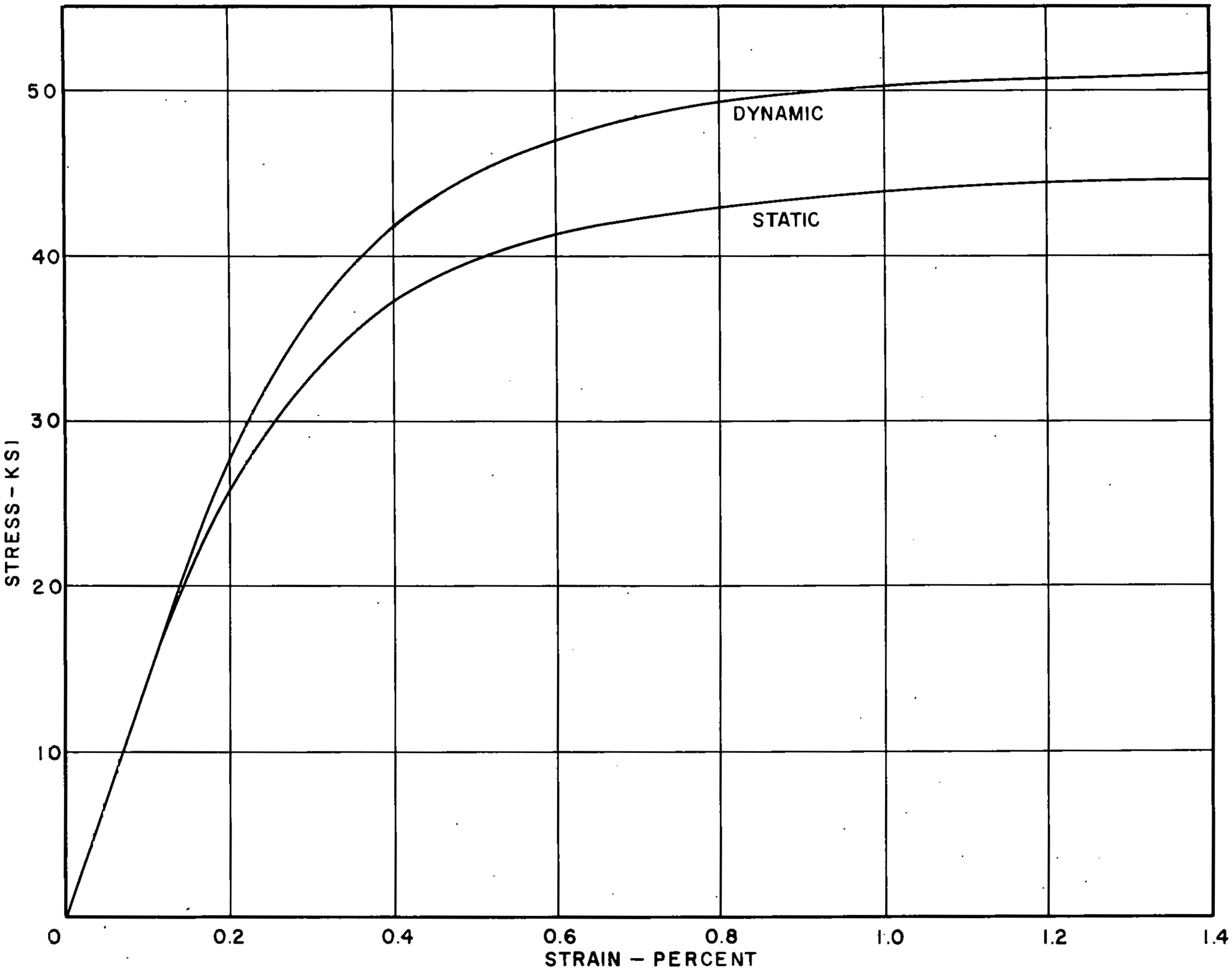

FIG. 61, STATIC AND DYNAMIC STRESS-STRAIN CURVE FOR COPPER

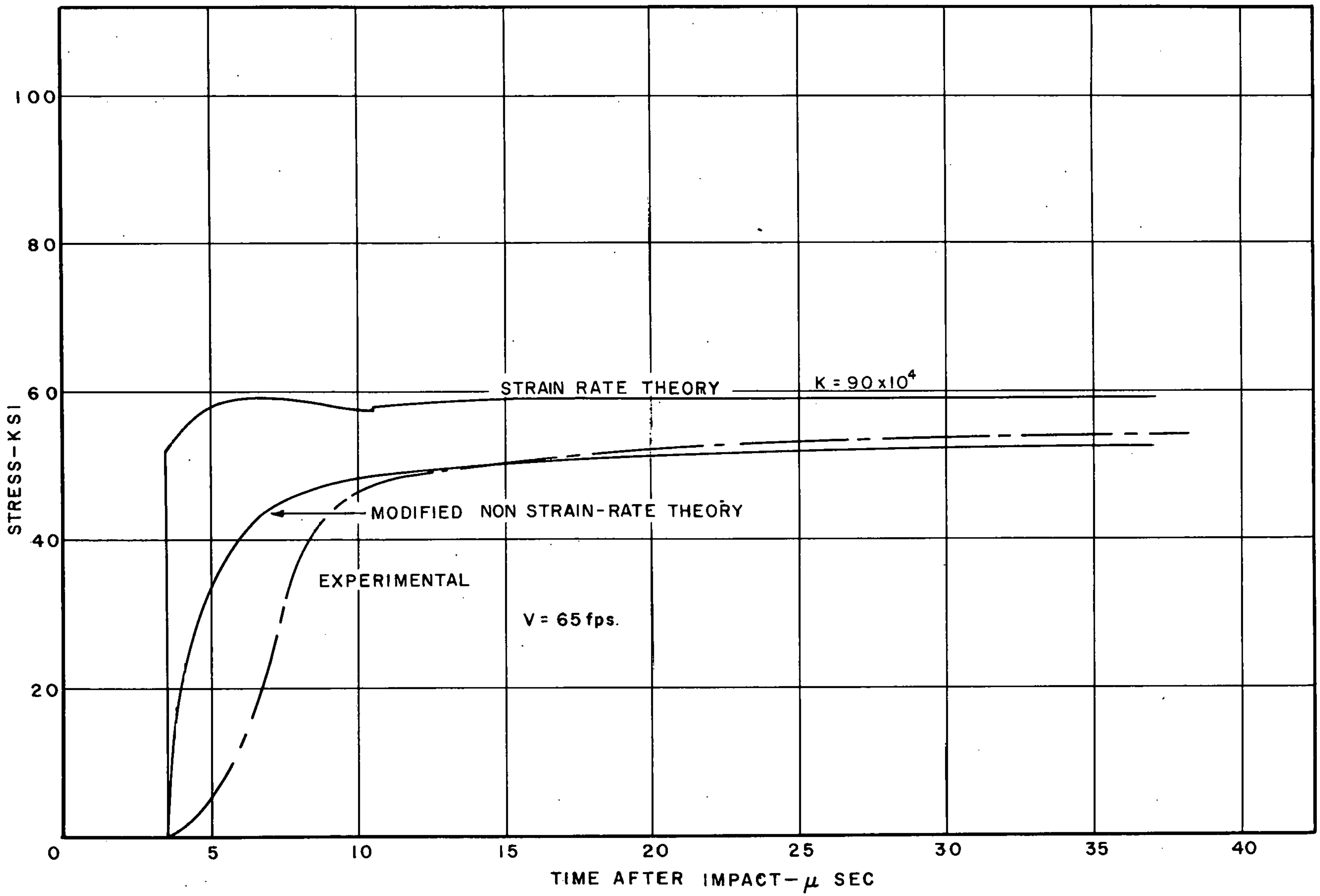

FIG. 62 COMPARISON OF STRESS FROM MODIFIED NONSTRAIN-RATE THEORY WITH STRAIN-RATE THEORY AND EXPERIMENT FOR ½ in. COPPER SPECIMEN

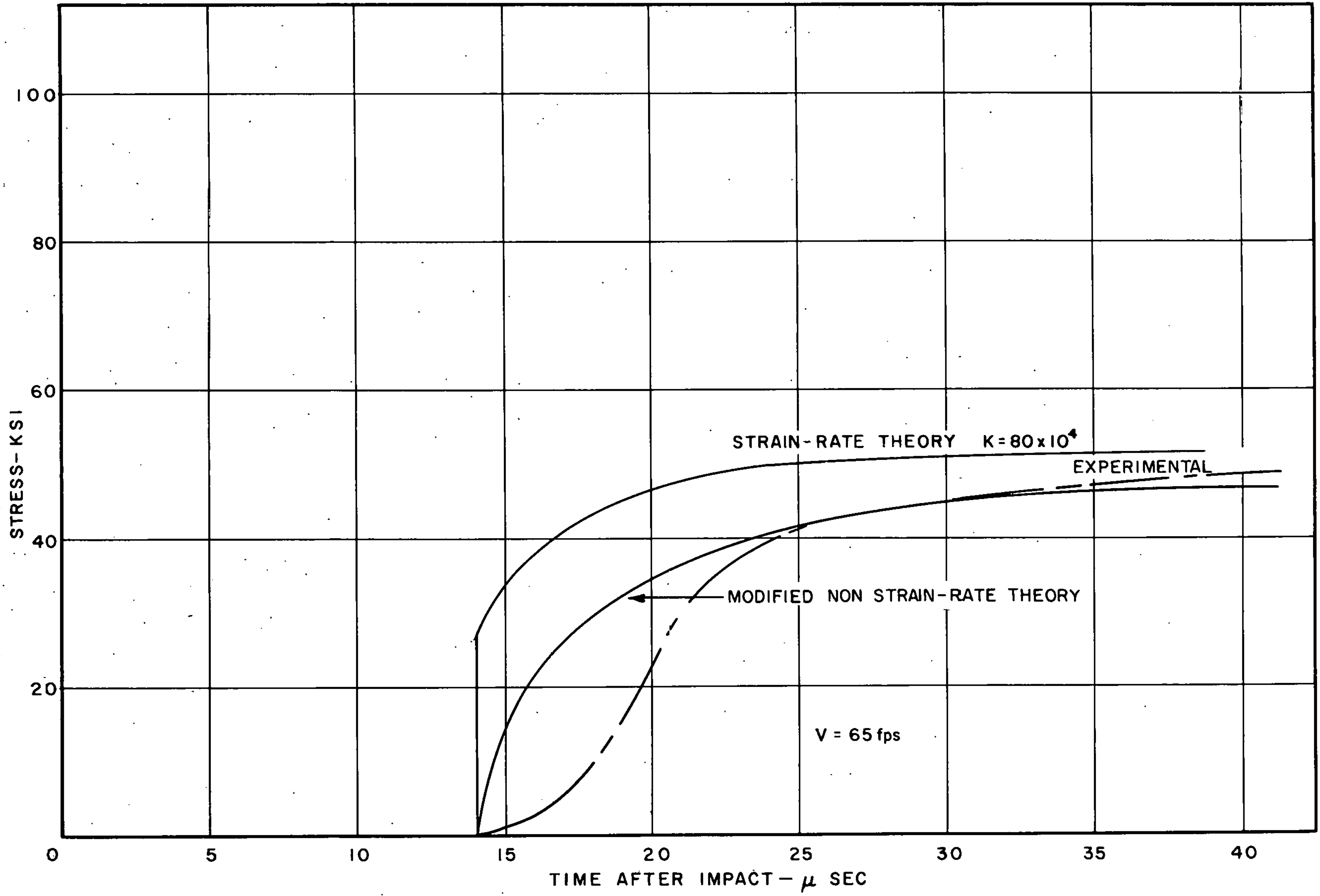

FIG. 63 COMPARISON OF STRESS FROM MODIFIED ELEMENTARY WITH STRAIN-RATE THEORY AND EXPERIMENT FOR 2in. COPPER SPECIMEN

remains the inconsistency of the required value of K obtained from the stress records as compared with that required by the strains. Even the strains predicted by the modified nonstrain-rate theory differ greatly from both the experimental curves and the elementary theory.

Evidently, when analyzing the stresses and strains at distances less than two diameters from the impact end, the problem is overly simplified when considered to be one-dimensional because of the effect of radial inertia on the measured quantities.

CONCLUSIONS

The following conclusions can be drawn concerning the results presented.

1. The nonstrain-rate or von Karman-Taylor theory predicts the variation of strain with time with reasonable accuracy except in the vicinity of the impact.
2. The average strain rate over the length of the specimen, V/L, has no relation to the strain rate measured at the impact end.
3. The ratio of the measured strain rate at the bar end to V/L decreases as the impact velocity increases, but increases as the specimen length increases.
4. The magnitude of the strain rate measured at the bar end for copper decreases with increasing specimen length, but has little relationship to the impact velocity for velocities above 33 fps.
5. An impact which is slightly out of plane affects the strains measured at the impact end considerably, but has little effect on those measured at the bar end.
6. Measurement of strain alone is not a very sensitive test as to the validity of the nonstrain-rate theory.
7. A step in particle velocity at the impact end of a specimen does not produce results which compare

favorably with experiment when the problem is considered to be one-dimensional.

8. The stresses predicted by the strain-rate theory indicate that the flow constant K for commercially pure copper should be approximately 250 x 10^4/sec.
9. The strains predicted by the strain-rate theory indicate that K should be about 40 to 50 x 10^4/sec.
10. The linear approximation to the strain-rate theory cannot be made to predict both the stresses and the strains experienced by copper specimens subjected to impact.
11. The nonstrain-rate theory using a "dynamic" stress-strain curve will predict the same stress-time variation as the strain-rate theory for a large value of K if a finite rise time is used instead of a step in particle velocity.
12. The effect of radial inertia in the first two diameters produces measured strains which are much smaller than those predicted by either of the two theories.
13. Observing the phenomenon of plastic wave propagation is a fruitful way of studying the dynamic stress-strain characteristics of materials.

14. Since the radial inertia is most pronounced when the strain rate is large and since it is small when the strain rate is small, and since it has been shown that both can have the same effect on the experimentally determined quantities, then it can be concluded that the two cannot be separated and must be analyzed concurrently unless the material being studied is either very sensitive or completely insensitive to strain rate.

RECOMMENDATIONS

It is apparent that neither the nonstrain-rate nor the linear strain-rate theory correctly predicts or explains all of the observed phenomena in a material subjected to impacts. It is, therefore, recommended that a detailed analysis be made employing the exponential strain-rate theory and that this analysis be made for the three-dimensional problem so that radial inertia and shear effects can be considered.

Since the linear strain-rate theory approaches the nonstrain-rate theory as the flow constant K increases without limit, it would be well to consider the three-dimensional problem when K is allowed to increase; that is, apply the nonstrain-rate theory in three dimensions.

More experimental information is needed concerning the strain distribution along the specimens. Tests should be made in which gages are placed in the middle as well as at both ends of the specimens.

Since there is a possibility that radial restraint affects both the stress and the strain records, then work should be performed to determine the effect of the amount and type of lubrication between the specimen and the two bounding surfaces, the pressure bar and the projectile.

Because of the inherent inaccuracy of resistance strain gages when used to measure large, rapidly changing strains, it is recommended that some of the experimental tests be repeated using a diffraction-grating-type strain gage and compare the results with those obtained with the resistance gages.

REFERENCES

1. Ripperger, E. A., *Stress-Strain Characteristics of Materials at High Strain Rates, Part II, Experimental Results,* Structural Mechanics Research Laboratory, The University of Texas, Austin, 1958.

2. Turnbow, James W., *Stress-Strain Characteristics of Materials at High Strain Rates, Part III, Strain Rate Effects and Plastic Wave Propagation,* Structural Mechanics Research Laboratory, The University of Texas, Austin, 1959.

3. Donnell, L. H., "Longitudinal Wave Transmission and Impact," *Transactions,* American Society of Mechanical Engineers, Vol. 52, pp 153-167, 1930.

4. von Karman, T. and P. Duwez, "The Propagation of Plastic Deformation in Solids," *Journal of Applied Physics,* Vol. 21, No. 10, p 987, 1950.

5. Taylor, G. I., "The Testing of Materials at High Rates of Loading (James Forrest Lecture)," *Journal of the Institute of Civil Engineers,* Vol. 26, 1946, pp 486-518.

6. Malvern, L. E., "The Propagation of Longitudinal Waves of Plastic Deformation in a Bar Exhibiting a Strain-Rate Effect," *Journal of Applied Mechanics,* Vol. 18, No. 2, p 203, 1951.

7. Griffis, L., "The Behavior of Longitudinal Stress Waves Near Discontinuities in Bars of Plastic Material," NDRC Armor and Ordnance Report No. A-212 (OSRD No. 1799) Division 2, 1943.

8. Benedick, Wm. B., "Air Guns and the Use of Air Propelled Projectiles," Technical Memorandum No. 79-56-51, Sandia Corporation, Albuquerque, New Mexico, June 5, 1956.

9. Fitzgibbon, D. P., *Stress-Strain Characteristics of Materials at High Strain Rates, Part I, Displacement Measurements During High Velocity Impacts,* Structural Mechanics Research Laboratory, The University of Texas, 1958.

10. Tubb, J., An Investigation of the Effect of Configuration on Elastic Failure of Cylinders Under Longitudinal Impact, Thesis, The University of Texas, 1959.

11. Schofield, B. H., R. A. Bareiss, and A. A. Kyrala, "Acoustic Emission Under Applied Stress," WADC Technical Report 58-194, 1958.